PhD thesis
October 2008

Numerical study of free surfaces and particle sorting in microfluidic systems

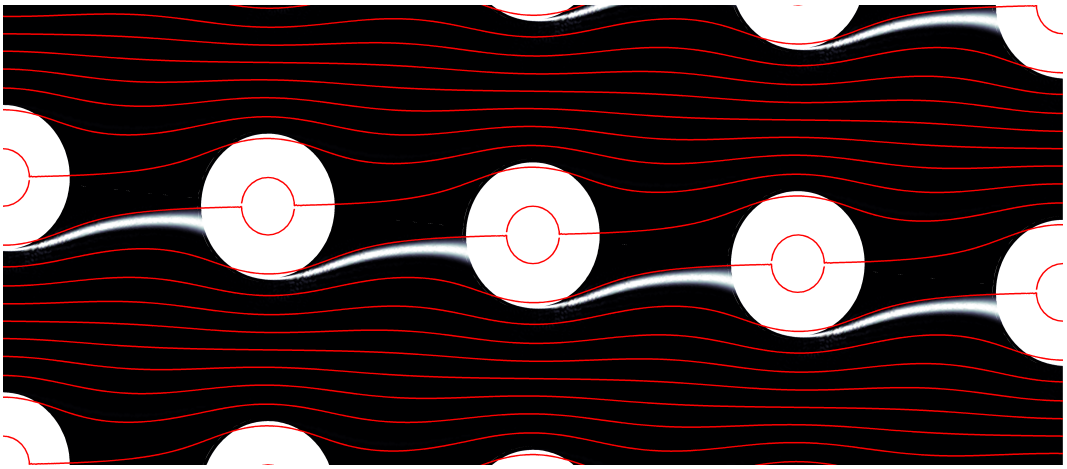

Martin Heller

Advisor prof. Henrik Bruus

Department of Micro- and Nanotechnology
Technical University of Denmark

Contents

List of Figures

List of Tables

List of Acronyms

DLD deterministic lateral displacement

FEM finite element

PDE partial differential equation

ALE arbitrary Lagrangian–Eulerian

FTP Forskningsrådet for Teknologi og Produktion

SEAS School of Engineering and Applied Sciences

MEMS micro electro mechanical systems

List of Symbols

Symbol	Description	Unit
η	Viscosity	$\mathrm{Pa\,s}$
ρ	Density	$\mathrm{kg/m^3}$
γ	Surface tension	$\mathrm{J/m^2}$
l, w, a, λ	Lengths	m
x, y, X, Y	Cartesian coordinates	m
s, S	Arc-length parameter	m
i, j	Coordinate indices	
m	Number of mesh nodes	
p	Pressure	Pa
Q	Flow	$\mathrm{m^3/s}$
t	Time	s
θ	angle	$^\circ$
κ	Curvature	$\mathrm{m^{-1}}$
$\ell_\mathrm{c} = \sqrt{\gamma/(\rho g)}$	Capillary length	m
$\boldsymbol{u} = [u, v]$	Velocity field	$\mathrm{m/s}$
$\boldsymbol{n}$	Normal vector	
$\boldsymbol{t}, \boldsymbol{T}$	Tangent vector	
$\boldsymbol{x} = [x, y]$	Position	m
$\boldsymbol{\sigma}$	Stress tensor	$\mathrm{Pa} = \mathrm{kg/(m\,s^2)}$

Continued from previous page...

Symbol	Description	Unit
$\boldsymbol{\nabla}$	Nabla operator	m^{-1}
Γ_i	Comsol flux vector	
F_i	Comsol source term	
d_a	Comsol coefficient	
G_i	Comsol coefficient in general Neumann BC	
R_i	Comsol coefficient in general Dirichlet BC	
Ω	Computational domain	
$\partial\Omega$	Boundary of computational domain	
$Re = \rho u l / \eta$	Reynolds number	
$Ca = \eta u / \gamma$	Capillary number	
$Pe = l u / D$	Péclet number	
ϵ	Wire width to capillary length ratio	
$\bar{\square}$	Denotes dimensionless quantities	
$\tilde{\square}$	Denotes test functions	
$\dot{\square}$	Differentiation with respect to arc-length	m^{-1}
$\square_0$	Denotes characteristic quantities	

Abstract

The results and models presented in this thesis are part of the work carried out during the author's PhD studies at Department of Micro- and Nanotechnology, Technical University of Denmark. The PhD project is part the frame programme *Polymer design and processing for microfluidic applications* supported by the Danish Research Council for Technology and Production Sciences, Grant No. 26-04-0074. The over all title of the PhD project is *Theory and design of polymer-based microfluidic systems*. The work has consisted of a number of smaller projects that are connected more by the numerical methods than by the physical phenomena. In the present thesis we discuss some of the issues relating to the numerical simulations of free surfaces and particle sorting in microfluidic systems that we have considered during the project. The thesis contains selected parts of the results obtained during the PhD studies. Other parts of the work have been published in peer reviewed journals or presented at conferences, see section 1.4.

Chronologically, the first topic of the PhD studies was deterministic lateral displacement (DLD) arrays. This work was initiated in collaboration with the experimentalists prof. Jonas O. Tegenfeldt and his PhD student Jason P. Beech from Lund University, Sweeden. As part of the analysis of the DLD arrays we present results of models including particle diffusion as well as analysis of a suggested device design with multiple sorting directions. The investigations of diffusion of particles in DLD arrays was inspired by the work on separation of nanometer-sized particles by Larsen *et al.* [26, 27]. A model of the influence of particle diffusion was published in the paper *A theoretical analysis of the resolution due to diffusion and size dispersion of particles in deterministic lateral displacement devices* [14]. The concept of multidirectional DLD devices and the influence of particle diffusion on separation in DLD devices are presented in chapter 4 together with numerical simulations of the particle distributions in such devices. Further analysis of the DLD devices have been published in collaboration with Brian R. Long, Jason P. Beech, Heiner Linke, Henrik Bruus, and Jonas O. Tegenfeldt in the paper *Multidirectional sorting modes in deterministic lateral displacement devices* [31].

The work on simulating non-spherical particles in DLD devices led us to study ways to represent free boundaries and moving objects in numerical simulations. In particular, we considered two methods: the level set method [18, 19] and the

arbitrary Lagrangian–Eulerian (ALE) method [46, 50]. Both methods were later used to model other systems. Using the level set method we studied capillary flows in micro-cuvettes from the Swedish company HemoCue AB [16]. Some parts of this work was presented at the annual meetings of the Danish and the American Physical Society (see section 1.4) other parts resulted in a course report [2].

The ALE method was used to study the drawing of liquid films from a bath of Newtonian liquid. This work was initiated during a five-month research visit at School of Engineering and Applied Sciences (SEAS) at Harvard University, USA [17]. During the stay at Harvard University I were supervised by prof. Howard A. Stone and worked closely together with his PhD student Ernst van Nierop who is setting up experiments to measure the thickness of a liquid film during its creation. At the time of writing experimental results have not been obtained but I have established a numerical framework capable of simulating the film drawing process including surface tension, Marangoni stresses and insoluble surfactants at the surface. The numerical implementation is presented in chapter 3, and we hope that it will prove useful in future analysis of the experimental results.

During the research stay at Harvard University a collaboration was initiated with PhD student Marjan Rafat from prof. Debra T. Auguste's research group at SEAS, Harvard University (USA) on studying hydrodynamic effects of the geometrical shape of Saccular Aneurysms on the risk of rupture [54]. This work is not included in the thesis but has been presented a at conferences by Marjan Rafat and a paper has been submitted to Stroke – Journal of The American Heart Association, see section 1.4.

In this thesis we briefly state the key governing equations used to simulate microfluidic systems. We go into some details on the implementation of the equations in the finite element (FEM) software package Comsol Multiphysics [7] which we have used for most of the numerical simulations. In particular we discuss how to model time-dependent microfluidic systems with free surfaces. The implementation developed during the work on this thesis handles surface tension and Marangoni stresses and allows to solve the dynamic equations on a domain deforming in time.

Resumé

Resultater og modeller i denne afhandling er udarbejdet i løbet af forfatterens ph.d.-studier. Ph.d.-projektet er en del af et af Forskningsrådet for Teknologi og Produktion (FTP) støttet rammeprogram *Polymerdesign og -processering til mikrofluide applikationer*. Den overordnede titel for ph.d.-projektet er *Teori og design af polymerbaserede mikrofluide systemer*. Arbejdet har bestået af flere mindre projekter med modellering og nummeriske simuleringer af mikrofluide systemer som gennemgående tema. I den hosliggende afhandling gennemgås nogle af de simuleringstekniske problemstillinger, som vi har arbejdet med i løbet af ph.d.-projektet. Desuden præsenteres dele af de i løbet af projektet opnåede resultater. Andre dele af arbejdet er blevet publiceret i fagfællebedømte tidskrifter eller er blevet præsenteret ved konferencer, se afsnit 1.4.

De såkaldte "deterministic lateral displacement (DLD) devices" var projektets første emne. Dette arbejde blev startet som et samarbejde med eksperimentalfysikerne professor Jonas O. Tegenfeldt og hans ph.d.-studerende Jason P. Beech fra Lund Universitet i Sverige. Som en del af analysen af DLD systemer præsenteres resultater fra modeller, der inkluderer partikeldiffusion samt en analyse af et foreslået design af et deterministisk flerretningssorteringssystem. Studierne af betydningen af diffusion af partikler i DLD systemer var inspireret af arbejdet med separation af nanometer-store partikler af Larsen med flere [26, 27]. En model, der inkluderer partikeldiffusion, for størrelsessortering af partikler i DLD systemer er publiceret i artiklen *A theoretical analysis of the resolution due to diffusion and size dispersion of particles in deterministic lateral displacement devices* [14]. Flerretningssorteringssystemet samt modellerne for partikeldiffusion i DLD systemer beskrives i kapitel 4 sammen med nummeriske simuleringer af partikelfordelinger i sådanne systemer. Yderligere analyser af DLD systemer er blevet publiceret i samarbejde med Brian R. Long, Jason P. Beech, Heiner Linke, Henrik Bruus, and Jonas O. Tegenfeldt i en artikel med titlen *Multidirectional sorting modes in deterministic lateral displacement devices* [31].

Arbejdet med simulering af ikke-sfæriske partikler i DLD systemer ledte til undersøgelser af forskellige metoder til at beskrive bevægede frie overflader i nummeriske simuleringer. Specielt undersøgte vi to metoder: level set metoderne [46, 50] samt den Arbitrære Lagrange-Eulerske (ALE) metode [18, 19]. Begge

beskrivelser blev senere brugt til at modellere andre systemer. Ved hjælp af level set metoden studerede vi kapillærstrømninger i mikrosystemer fra det svenske firma HemoCue AB [16]. Dele af dette arbejde blev præsenteret i forbindelse med årsmøderne i Dansk Fysisk Selskab og i American Physical Society (se afsnit 1.4). Andre dele af dette arbejde resulterede i en kursusrapport [2].

arbitrary Lagrangian–Eulerian (ALE) metoden blev benyttet til at studere tilblivelsen af Newtonske væskefilm dannet ved at løfte en hydrofil tråd fra et bad. Dette projekt blev påbegyndt i forbindelse med et fem måneders forskningsophold på School of Engineering and Applied Sciences (SEAS) på Harvard University, USA. Under opholdet blev jeg vejledt af professor Howard A. Stone og arbejdede tæt sammen med hans ph.d.-studerende Ernst van Nierop [17], der arbejder på at opbygge en forsøgsopstilling, hvor tykkelsen af en væskefilm kan måles under dens tilblivelse. I skrivende stund er de eksperimentelle resultater stadig ikke i hus, men jeg har udarbejdet det nødvendige nummeriske fundament til fremtidige numeriske simuleringer af væskefilm. Den numeriske implementering kan indeholde både overfladespænding, Marangoni-effekter samt overfladeaktive stoffer. Den nummeriske implementering er præsenteret i kapitel 3. Det er vores forhåbning, at koden vil komme til gavn i forbindelse med fremtidige analyser af de eksperimentelle resultater.

I forbindelse med opholdet på Harvard University indledtes også et samarbejde med ph.d.-student Marjan Rafat fra professor Debra T. Augustes forskningsgruppe på SEAS ved Harvard University (USA) [54]. Formålet med dette samarbejde var at studere betydningen af Aneurysmers geometri på risikoen for, at de sprænger. Dette arbejde er ikke inkluderet i afhandlingen, men er blevet præsenteret i forbindelse med konferencer af Marjan Rafat. Desuden er en artikel sendt til Stroke – Journal of The American Heart Association, se afsnit 1.4.

I denne afhandling beskriver vi kort de ligninger, der benyttes til numeriske simuleringer af mikrostrømningssystemer. Særligt implementeringen af ligningerne i finite element (FEM) programmet Comsol Multiphysics [7] beskrives i stor detalje. Specielt beskrives vores implementering, der muliggør tidsafhængige simuleringer af mikrofluide systemer med frie overflader. Implementeringen tager både højde for overfladespænding og Marangoni-effekter, og er i stand til at håndtere domæner, der ændrer form.

Preface

The present thesis is submitted in candidacy for the PhD degree from the Technical University of Denmark. The work has been part of the frame programme *Polymer design and processing for microfluidic applications*. The duration of the project has been from 1 October 2005 to 1 October 2008. The main part of the PhD studies has been carried out at Department of Micro and Nanotechnology in the Theoretical Microfluidics group headed by professor Henrik Bruus [55]. During the project I also spend five months from 1 September 2007 to 1 February 2008 in the group of professor Howard A. Stone at the School of Engineering and Applied Sciences (SEAS) at Harvard University, USA.

During the project many people have provided support and feedback and I would like to use this occasion to thank them. I would like to thank prof. Ole Hassager and the participants in the frame programme for interesting and stimulating discussions at our monthly meetings. Without the exceptional working environment in the Theoretical Microfluidics group the work on the thesis would not have been as rewarding as it has been. I would therefore like to express my gratitude to all the members of the Theoretical Microfluidics group. In particular, I would like to thank the alumni Laurits Højgaard Olesen and Mads Jakob Jensen for introducing me to the Comsol finite element software. I would also like to acknowledge Rune Barnkob and Mathias Bækbo Andersen who I worked with and co-supervised during 2007. A special thanks goes to my office mate and fellow PhD student Misha Marie Gregersen who have provided invaluable inputs to both scientific discussions and moral support throughout the entire project.

I would also like to thank professor Howard A. Stone and the members of his research group for hosting me and quickly making me feel part of the group. In particular, I would like to thank PhD student Ernst van Nierop for involving me in his work. Finally I owe a huge thanks to my supervisor professor Henrik Bruus. Henrik first introduced me to the field of microfluidics during my master studies and his inspiring supervision has kept me hooked on the subject ever since. I have benefitted enormously from our many discussions and his huge engagement in his students. At last I would like to thank my friends and family for their support throughout the project.

Martin Heller
Department of Micro and Nanotechnology
Technical University of Denmark

1. Introduction

1.1. Microfluidics and lab-on-a-chip systems

During the last fifteen years microfluidics have received a growing interest [6, 13, 51, 53]. The sophisticated fabrication techniques developed for use in the micro electronics industry kick-started this development and aided the design and fabrication of microfluidic systems utilizing the fascinating and often counter-intuitive physical properties of fluids in confined geometries. Also improved visualization tools such as micro PIV and high-speed cameras have accelerated the development. In resent years polymer processing techniques have evolved and we are now starting to see massproduction of cheap microsystems that can perform accurate and reliable analysis of microfluidic samples. As the complexity of the systems rises and the demand for systems that adresses even more applications grow it becomes of paramount importens with a good understanding of the underlying physical phenomena. When analytical modeling becomes impossible or too difficult, and when experimental verification is not feasible or too time consuming, a good set of tools for performing the analysis is quintessential for the scietific and technological advancement of this promising field. Numerical simulations have proven to be one of the efficient tools for exploring new phenomena and confirming observed behavior of microfluidic systems.

1.2. The thesis work

In the work carried out during this thesis we have focused on addressing some issues relating to theoretical modeling and numerical simulation of fluids on the micro scale. There have been two main parts of this work: (1) to setup a general numerical framework using the finite element (FEM) software package Comsol Multiphysics [7] for studying a broad set of microfluidic problems with free boundaries, specifically the pulling of liquid films, and (2) to study a specific class of microfluidic devices, the deterministic lateral displacement (DLD) arrays, using numerical means. We have chosen to use Comsol as the main tool for carrying out the analysis. Comsol is a versatile and flexible high-level software for solving partial differential equations. This means that the code we have developed

can be adapted to other applications or more phenomena can be included in the analysis of the systems we have been studying. Microfluidic systems with free surfaces are are often encountered. The Young–Laplace pressure due to a curved meniscus can be used as a passive pump to drive fluid into a micro channel, drops and bubbles can be used as small containers for mixing or transport of substances, or they can stick and hinder the flow in a micro system. To model these kinds of microfluidic systems a numerical scheme that can handle the deformation of the boundaries and take the physics at the interfaces into account is needed. During the PhD project we have worked with several models capable of handling the simulation-technical challenges posed by this class of microfluidic systems. We have worked with level set methods where the interface between two immiscible fluids are represented implicitly by a constant valued level curve of a artificial field convected with the fluid [43–46, 50]. This method was used to model the capillary filling of micro cuvettes for analyzing blood samples from the Swedish company HemoCue AB [16].

In this thesis we present a different numerical implementation capable of handling microfluidic systems with free surfaces while accurately tracking the precise position of the interface. The implementation uses the arbitrary Lagrangian–Eulerian (ALE) method to keep track of the points on the boundaries of the deforming fluid domain [18, 19, 40]. At the free interface we have used a boundary condition that takes advantage of the underlying finite element method allowing us to include the effects of surface tension and Marangoni stresses without having to explicitly calculate the curvature of the interface. Both the accurate tracking of a moving interface as well as calculating the curvature of an interface are numerically challenging tasks.

The initial plan regarding the DLD devices was to study non-spherical particles in DLD arrays and examine the limits of deterministic separation on the microscale. Sadly, the clean-room facilities at Lund University broke down before experimental results were obtained and the project were not pursued in full. However, the work by Larsen *et al.* [26, 27] on scaling down DLD devices in order to obtain deterministic separation of nanometer-sized particles inspired us to examine the effects of diffusion on the deterministic lateral separation process. In this thesis we present a discrete model of the separation process as well as a numerical implementation of a continuum model that can be used for studying the expected particle distributions in DLD devices. The numerical model is used to verify the existence of novel sorting modes in a multidirectional DLD array design.

1.3. Outline of the thesis

The specific outline of the thesis is as follows.

Chapter 2: Theoretical framework We state the governing equations used when modeling microfluidic systems including a discussion of the non-dimensionalization of the equations. The details of the implementation of Navier-Stokes equation in an arbitrary Lagrangian–Eulerian (ALE) reference frame in Comsol are discussed. In addition we describe the implementation of a free surface boundary condition taking surface tension and Marangoni stresses into account. The code is verified using a model problem consisting of a viscous ellipse deforming due to surface tension.

Chapter 3: Thin liquid films In this chapter we discuss the results of using our numerical code on the problem of drawing liquid films from a bath of Newtonian liquid. The work on this problem is inspired by experimental work of PhD student Ernst van Nierop, Harvard University (USA).

Chapter 4: Deterministic lateral displacement devices Here we discuss the influence of diffusion on the sorting of particles in deterministic lateral displacement (DLD) devices. We show that the critical radius for a given device depends on the diffusion of particles. We also suggest a novel design of a multidirectional DLD device and present a numerical implementation for analyzing the separation in the devices.

Chapter 5: Conclusions and outlook Finally we discuss possible future improvements and applications af our models and code.

1.4. Publications during the PhD studies

During the PhD project the following three journal papers and five conference contributions were made.

1.4.1. Peer reviewed research papers

1. *A theoretical analysis of the resolution due to diffusion and size dispersion of particles in deterministic lateral displacement devices*,
   Martin Heller and Henrik Bruus,
   J. Micromech. Microeng. **18** (2008).

2. *Multidirectional sorting modes in deterministic lateral displacement devices*, Brian R. Long, Martin Heller, Jason P. Beech, Heiner Linke, Henrik Bruus, and Jonas O. Tegenfeldt, Physical Review E **78**, in press (2008).

3. *Geometry Regulates Hemodynamics in Saccular Aneurysms*, Marjan Rafat, Martin Heller, Howard A. Stone, and Debra T. Auguste, Submitted to Stroke – Journal of The American Heart Association, August 2008.

1.4.2. Conference contributions

1. *Control of capillary flow by shape-perturbation and contact angle modification*, Martin Heller, Mathias Bækbo Andersen, Rune Barnkob, and Henrik Bruus, Annual Meeting of Dansk Fysik Selskab, Nyborg, Denmark, June 2007 [poster presentation].

2. *Control of capillary flow by shape-perturbation*, Martin Heller, Mathias Bækbo Andersen, Rune Barnkob, and Henrik Bruus, 60th Annual Meeting of the American Physical Society Division of Fluid Dynamics, Salt Lake City, USA, November 2007 [oral presentation].

3. *Correlating Hemodynamics and Protein Regulation in Intracranial Correlating Hemodynamics and Protein Regulation in Intracranial Aneurysms*, Marjan Rafat, Martin Heller, Howard A. Stone, and Debra T. Auguste, Biomedical Engineering Society (BMES) Annual Meeting, St. Louis, USA, October 2008. [poster presentation]

4. *Investigation of Hemodynamics In Saccular Aneurysms*, Marjan Rafat, Martin Heller, Howard A. Stone, and Debra T. Auguste, American Institute of Chemical Engineers (AIChE) Annual Meeting, Philadelphia, USA, November 2008 [oral presentation].

5. *Coupling Hemodynamics and Protein Regulation In Cerebral Saccular Aneurysms*, Marjan Rafat, Martin Heller, Howard A. Stone, and Debra T. Auguste, American Institute of Chemical Engineers (AIChE) Annual Meeting, Philadelphia, USA, November 2008 [poster presentation].

2. Theoretical framework

The main work during this thesis has been related to numerical simulation of microfluidic systems. In this chapter we present the main governing equations used in the thesis and describe how we have implemented them in the numerical software Comsol Multiphysics [7].

2.1. Governing equations in static domains

First we state the general form of the equations. Later we will go into issues relating to solving the equations in a domain deforming in time and go over the details of how we have implemented the influence of surface tension which plays a key role in the description of thin liquid films [6, 25, 28].

Conservation of mass is ensured by the continuity equation

$$\partial_t \rho + \boldsymbol{\nabla} \cdot (\rho \boldsymbol{u}) = 0. \tag{2.1}$$

In most microfluidic systems the fluids can be assumed incompressible in which case (2.1) reduces to the incompressibility condition

$$\boldsymbol{\nabla} \cdot \boldsymbol{u} = 0. \tag{2.2}$$

The main equation describing the momentum conservation for an incompressible Newtonian fluid in the continuum approximation is the Naver–Stokes equation

$$\rho\big(\partial_t \boldsymbol{u} + (\boldsymbol{u} \cdot \boldsymbol{\nabla})\boldsymbol{u}\big) = \boldsymbol{\nabla} \cdot \boldsymbol{\sigma} + \boldsymbol{f}, \tag{2.3}$$

where the components of the stress tensor $\boldsymbol{\sigma}$ are

$$\sigma_{ij} = -\delta_{ij} p + \eta(\partial_j u_i + \partial_i u_j), \tag{2.4}$$

and $\boldsymbol{f}$ is a bulk force, e.g. gravity, working on the fluid.

Together with an appropriate set of boundary conditions, equation (2.3) and (2.2) describe the state of an incompressible Newtonian fluid with constant density ρ and viscosity η in terms of the fluid velocity $\boldsymbol{u}$ and the pressure p.

2.1.1. Dimensionless form

When solving the governing equations numerically it is often advantageous to scale the equations using characteristic properties of the system. In this thesis we scale the governing equations with respect to a characteristic velocity u_0 and a characteristic length scale l_0. Viscous forces are often the most dominant in microfluidics [6, 53]. We therefore use $\eta_0 u_0/l_0$ as the characteristic scale for non-dimensionalizing the stress in the fluid. With these characteristic scales the governing equations are made dimensionless by introducing a dimensionless counterpart to each of the physical variables in the following way

$$\boldsymbol{x} = l_0\bar{\boldsymbol{x}}, \qquad \boldsymbol{u} = l_0\bar{\boldsymbol{u}}, \qquad p = \frac{\eta_0 u_0}{l_0}\bar{p}, \qquad t = \frac{l_0}{u_0}\bar{t}, \tag{2.5}$$

where the overbar denotes the dimensionless quantities. Substitution in equation (2.3) and equation (3.37) yields

$$Re\big(\partial_{\bar{t}}\bar{\boldsymbol{u}} + (\bar{\boldsymbol{u}}\cdot\bar{\boldsymbol{\nabla}})\bar{\boldsymbol{u}}\big) = \bar{\boldsymbol{\nabla}}\cdot\bar{\sigma} + \bar{\boldsymbol{f}}, \tag{2.6}$$

$$0 = \bar{\boldsymbol{\nabla}}\cdot\bar{\boldsymbol{u}}, \tag{2.7}$$

where the dimensionless group $Re = \rho_0 u_0 l_0/\eta_0$ is the the Reynolds number relating inertial forces to viscous forces. The specific choices of u_0 and l_0 depends on the actual problem we are studying and will be discussed in the discussions of the specific models during the thesis. However, for the applications we have in mind in this thesis Re is typically of the order 1×10^{-5} to 1×10^{-2}. In this regime we can therefore neglect the left hand side of the dimensionless Naver–Stokes equation and still obtain reliable results. When not specifically mentioned otherwise, we will therefore use the non-dimentionless Stokes equation

$$0 = \bar{\boldsymbol{\nabla}}\cdot\bar{\sigma} + \bar{\boldsymbol{f}}, \tag{2.8}$$

for the remaining part of this thesis to model the flow in the microfluidic systems under study.

2.1.2. Finite element implementation in Comsol

A major part of the work during the thesis has been devoted to implementing and solving microfluidic problems using the finite element (FEM) software Comsol [7]. Comsol is an extremely versatile software package for solving systems of coupled partial differential equations using the finite element method. Depending on which license you buy Comsol comes with predefined application modes for

solving problems relating to specific fields of physics or engineering[1] However, for the problems we wish to solve we ether have boundary conditions which are not available in the application modes (see chapter 3), or we use a formulation of the problem that is not predefined in the application modes (see section 4.4). For this reason we have chosen to use the scripting capabilities of Comsol in combination with Matlab [33] and enter the equations manually. To set the scene for descriptions of the different implementations in the thesis, we will therefore discuss some of the general implementation issues considered during the work on the thesis.

2.1.2.1. General divergence form

In order to solve partial differential equations with Comsol the equations must be stated in a general divergens form

$$d_{a_{ji}} \frac{\partial U_i}{\partial t} + \partial_j \Gamma_{ij} = F_i, \qquad \text{in } \Omega, \tag{2.9}$$

where U_i is a vector with the i dependent variables to be solved for and $d_{a_{ij}}$, $\mathbf{\Gamma}_{ij}$ and F_i are coefficients that can be functions of the spatial coordinates j, time t, and the dependent variables and their derivatives. Here we have used the Einstein summation rule over repeated indices. The bulk equations are solved subject to the boundary conditions

$$R_i = 0, \qquad \text{on } \partial\Omega \tag{2.10a}$$

$$-n_j \Gamma_{ij} = G_i + \mu_k \frac{\partial R_k}{\partial U_i}, \qquad \text{on } \partial\Omega, \tag{2.10b}$$

where n_j is an outward pointing normal vector at the boundary $\partial\Omega$ of the computational domain Ω. The coefficients R_i and G_i must be specified by the user. Equation (2.10a) is a Dirichlet condition on the dependent variable, and equation (2.10b) is a generalized Neumann boundary condition. The Lagrange multiplier μ_k is computed internally by Comsol in order to satisfy eq. (2.10b). If we do not wish to specify a Dirichlet condition at some boundary we can trivially fulfill eq. (2.10a) by specifying $R_i \equiv 0$ at that boundary. The Lagrange multiplier term in equation (2.10b) will then vanish and we must define a Neumann condition on the solution by specifying G_i in $-n_j \Gamma_{ij} = G_i$. If we specify a Dirichlet condition $U_i = U_0$ by setting $R_i = U_0 - U_i$ then equation (2.10b) is relaxed because Comsol can choose the value of μ_k to satisfy the condition independent of the choice of G_i.

[1] There are e.g. application modes for acoustics, fluidics and micro electro mechanical systems (MEMS).

This type of boundary constraint is known as an ideal constraint. One limitation is that if a Dirichlet constraint contains more than one dependent variable Comsol will consider the constraint to be equally a constraint on both of them. This, as we will see, is a problem when specifying boundary conditions in a moving reference frame because only the fluid motion is physical. We want the mesh to follow the fluid without imposing unphysical constraints on the fluid. To control this coupling we need to specify the equations in weak form which we will discuss in section 2.1.2.2.

In a Comsol script, equation (2.9) and the boundary conditions (2.10a) and (2.10b) can be specified by creating a `struct` element `fem` containing the fields `fem.equ.da`, `fem.equ.ga` and `fem.equ.f` corresponding to the coefficients $d_{a_{ji}}$, Γ_{ij} and F_i in the bulk equation and `fem.bnd.r` and `fem.bnd.g` for R_i and G_i, respectively. To implement the two dimensional Stokes equation (2.8) in Comsol general form we can therefore define

$$\boldsymbol{U} = \begin{bmatrix} u \\ v \\ p \end{bmatrix}, \qquad \boldsymbol{d}_a = \mathbf{0}, \qquad \boldsymbol{F} = \begin{bmatrix} 0 \\ 0 \\ \partial_x u + \partial_y v \end{bmatrix}, \tag{2.11a}$$

$$\boldsymbol{\Gamma}_u = \begin{bmatrix} \sigma_{xx} \\ \sigma_{xy} \end{bmatrix}, \qquad \boldsymbol{\Gamma}_v = \begin{bmatrix} \sigma_{yx} \\ \sigma_{yy} \end{bmatrix}, \qquad \boldsymbol{\Gamma}_p = \begin{bmatrix} 0 \\ 0 \end{bmatrix}. \tag{2.11b}$$

The corresponding Comsol implementation is shown in code listing 2.1.

```
fem.form = 'general';
fem.dim = {'u' 'v' 'p'};
fem.expr = {'sigmaxx' '-p+2*ux' 'sigmayx' 'vx+uy' ...
            'sigmaxy' 'uy+vx'   'sigmayy' '-p+2*vy'};
fem.equ.ga = {{{'sigmaxx' 'sigmaxy'} ...
               {'sigmayx' 'sigmayy'} ...
               {'0' '0'}}};
fem.equ.f = {{{'0'} {'0'} {'ux+vy'}}};
```

Listing 2.1: Stokes equation in Comsol script notation using the general equation form.

The general equation form is very convenient, and we have used it to implement the continuum model of the deterministic lateral displacement devices described in chapter 4.

2.1.2.2. Weak equation form

It is not always possible to state the governing equations and corresponding boundary conditions in a way that is compatible with Comsol's general equation form. This does not imply that we cannot use Comsol to solve the equations but we must then specify the equations in variational or weak form. The weak form of the equations is tightly bound to the FEM formulation which Comsol uses to solve the equations. The finite element method has been extensively described in textbooks [8, 41, 58] and we will not go into extensive details with the method but only state what is necessary for discussing the implementation we have used in this thesis.

The general idea in the FEM method is to approximate the ith component $U_i(\boldsymbol{x})$ for $\boldsymbol{x} \in \Omega$ of a solution to a partial differential equation (PDE) by a linear combination of a finite number of basis functions $\phi_{mi}(\boldsymbol{x})$ on a mesh with nodes m. The basis functions must have a compact support, i.e., basis function $\phi_{mi}(\boldsymbol{x})$ is only non-zero in the mesh elements containing node m. Everywhere else they are zero. The finite element solution $U_i(\boldsymbol{x})$ is then given as

$$U_i(\boldsymbol{x}) = \sum_m u_m \, \phi_{mi}(\boldsymbol{x}). \tag{2.12}$$

In the following we suppress the node index m since it never appears explicitly in the Comsol code. Comsol uses the Galerkin discretization method in which the weak equation form corresponding to a given strong equation is obtained by multiplying with the basis function and integrating over the computational domain [37, 41]. The weak form corresponding to equation (2.9) is therefore

$$\int_\Omega \phi_i \left(d_{a_{ji}} \frac{\partial U_i}{\partial t} + \partial_j \Gamma_{ij} \right) \mathrm{d}\boldsymbol{x} = \int_\Omega \phi_i \, F_i \, \mathrm{d}\boldsymbol{x}. \tag{2.13}$$

Integrating by parts and rearranging the equation to have time dependent terms on the left hand side and time independent terms on the right hand side we obtain

$$\int_\Omega \phi_i \, d_{a_{ji}} \frac{\partial U_i}{\partial t} \, \mathrm{d}\boldsymbol{x} = \int_\Omega \left((\partial_j \phi_i) \Gamma_{ij} + \phi_i \, F_i \right) \mathrm{d}\boldsymbol{x} - \int_{\partial\Omega} \phi_i \, n_j \Gamma_{ij} \, \mathrm{d}s. \tag{2.14}$$

The weak equation form can be specified in Comsol by entering the integrands on the left hand side of the equation in the `struct` field `fem.equ.dweak` and the integrands on the right hand side in the fields `fem.equ.weak` and `fem.bnd.weak` for the bulk and boundary contributions, respectfully (see code listing 2.2).

```
1 fem.form = 'weak';
2 fem.dim = {'u' 'v' 'p'};
```

```
fem.expr = {'sigmaxx' '-p+2*ux' 'sigmayx' 'vx+uy' ...
            'sigmaxy' 'uy+vx'   'sigmayy' '-p+2*vy'};
fem.equ.weak = {{ ...
    '-(sigmaxx*test(ux)+sigmaxy*test(uy))'; ...
    '-(sigmayx*test(vx)+sigmayy*test(vy))'; ...
    '-(ux+vy)*test(p)'}};
```

Listing 2.2: Stokes equation in Comsol script notation using the weak equation form. The basis functions are denoted by `test(...)`.

The partially integrated weak form of the equations enable us to easily specify a Neumann boundary condition $n_j \Gamma_{ij}$ simply by substitution in the boundary integral term. If instead we wanted to specify a Dirichlet type condition $R_i = 0$ we would solve the additional problem

$$\int_{\partial\Omega} \phi_i \, R_i \, \mathrm{d}s = 0 \tag{2.15}$$

at the relevant boundary $\partial\Omega$. This way of specifying the boundary condition corresponds to the ideal strong constraint Eq. (2.10a) we could specify using the general equation form. However, we can also enforce the Dirichlet constraint by adding a Lagrange multiplier μ_i discretized using the basis function φ_i to relax the Neumann condition in the the original problem and enforce the Dirichlet constraint. We can then view the Lagrange multiplier as 'whatever force necessary' to enforce the Dirichlet constraint. In this formulation we must change the boundary integral in equation (2.14) to

$$\int_{\partial\Omega} (\mu_i \phi_i + \varphi_i R_i) \, \mathrm{d}s \tag{2.16}$$

on boundaries with a Dirichlet constraint. This method of applying the Dirichlet condition is termed a non-ideal weak constraint. When using this method we can control, on which dependent variables a Dirichlet condition will act. This control comes at the expense of having to solve for an additional variable at the boundaries, the Lagrange multiplier. Normally this will not be a problem as the number of elements at the boundaries is small compared to the number of elements used to discretize the domain interior. As we will discuss in section 2.2.1 we will use the non-ideal weak constraints to enforce the boundary conditions when solving equations on a moving mesh using the Arbitrary Lagrangian Eulerian method. This is done to avoid unphysical contributions from the equations governing the mesh motion to the hydrodynamics of the problem.

2.2. Governing equations in time-dependent domains

One of the challenges faced in this thesis was the modeling of the process of drawing a liquid film from a bath of liquid. This type of problem presents two major hurdles which we had to overcome. We need some way to track the boundaries of the domain as the liquid surface is deformed and we need a scheme to accurately specify the curvature dependent boundary condition at the free surface.

The problem of tracking the boundaries of the domain as it is deforming can be tackled in different ways. One way is to use a two-step approach where the flow problem is first solved with static boundaries in an Eulerian reference frame and the forces at the surface is found. Then in a second step the surface position is updated and the flow is found for the new position of the liquid interface. This method is for example used by Jensen [22] and Jin et al. [23].

An alternative option is to represent the interface implicitly as is done in the various level set methods. Here the evolution of the interface is described by the zero-contour of a continues function which is convected by the fluid. In this formulation forces at the interface are smeared out by treating them as a volume force multiplied with a smeared out delta-function near the interface [43–46, 50].

To avoid the inaccuracies connected with updating the position of the liquid interface separately from the velocity and pressure fields and to avoid the smearing of the forces at the meniscus, we have chosen to solve the governing equations in a coordinate system deforming with the liquid. Due to the large deformations which the fluid undergoes in our film drawing problem, a purely Lagrangian reference frame where the mesh follows the fluid particles is not practical. Instead we use an intermediate between the traditional Eulerian reference frame and the Lagrangian reference frame. This hybrid is commonly known as the Arbitrary Lagrangian-Eulerian (ALE) reference frame [18, 19, 40]. The basic idea is to allow the mesh to deforme arbitrarily (but preferably smooth) in the bulk but still keep track of the interface of the liquid.

2.2.1. Arbitrary Lagrangian–Eulerian formulation

Let us consider a generic partial differential equation[2] which we want to solve in a domain $\Omega(t)$ changing with time. For simplicity we only consider a scalar equation of the form

$$d_a \frac{\partial u}{\partial t} + \boldsymbol{\nabla} \cdot \boldsymbol{\Gamma} = F \qquad \text{for } \boldsymbol{x} \in \Omega(t). \tag{2.17}$$

In the above equation d_a, $\boldsymbol{\Gamma}$ and F are functions of the solution u, time t and position $\boldsymbol{x}$. We wish to map this problem defined in $\Omega(t)$ onto a static domain Ω' in which

[2]This form of the equation is chosen because it matches the 'general form' used by Comsol.

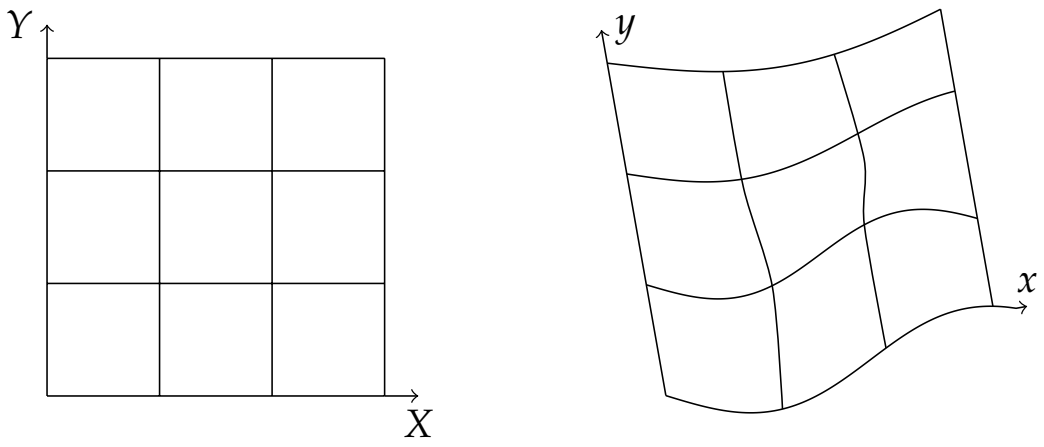

Figure 2.1.: The static reference frame $\boldsymbol{X} \in \Omega'$ and the deformed frame $\boldsymbol{x} \in \Omega(t)$. At $t = 0$ the two frames are identical.

we can solve it numerically. We do this by defining a mapping $r\colon \Omega(t) \mapsto \Omega'$ such that

$$\boldsymbol{x} = r(\boldsymbol{X}, t) \qquad \text{for all } \boldsymbol{x} \in \Omega(t) \text{ and } \boldsymbol{X} \in \Omega'. \tag{2.18}$$

With this map integrals on $\Omega(t)$ transform to Ω' according to the change of variables theorem [1]

$$\int_{\Omega(t)} f(\boldsymbol{x}, t)\, \mathrm{d}\boldsymbol{x} = \int_{\Omega'} f[\boldsymbol{x}(\boldsymbol{X}, t), t] \det \boldsymbol{J}\, \mathrm{d}\boldsymbol{X}, \tag{2.19}$$

where $\det \boldsymbol{J}$ is the determinant of the Jacobian matrix $\boldsymbol{J} = \partial \boldsymbol{x} / \partial \boldsymbol{X}$.

Thus, we can write our original time dependent problem in variational form in the static domain as

$$\int_{\Omega'} \phi \left[d_a \frac{\partial u}{\partial t} \right] \det \boldsymbol{J}\, \mathrm{d}\boldsymbol{X} = \int_{\Omega'} \left[\phi F + \boldsymbol{\nabla} \phi \cdot \boldsymbol{\Gamma} \right] \det \boldsymbol{J}\, \mathrm{d}\boldsymbol{X} - \int_{\partial \Omega'} \phi \left[\boldsymbol{n} \cdot \boldsymbol{\Gamma} \right] \det \boldsymbol{J}_{\mathrm{s}}\, \mathrm{d}S, \tag{2.20}$$

where we have integrated by parts and used a transformation according to (2.19). The boundary Jacobian $\det \boldsymbol{J}_{\mathrm{s}} = \partial s / \partial S$ is defined in terms of the arc-length parameters s in the deforming domain $\Omega(t)$ and S in the stationary domain Ω. The integrands must be evaluated with $\boldsymbol{x} = \boldsymbol{x}(\boldsymbol{X}, t)$. The same is true for derivatives in the two reference frames. The derivatives are related by the chain rule, i.e.,

$$\frac{\partial u(\boldsymbol{x}(\boldsymbol{X}, t), t)}{\partial x_i} = \frac{\partial u(\boldsymbol{X}, t)}{\partial X_J} \frac{\partial X_J}{x_i}. \tag{2.21}$$

The same is true for the time derivatives which are related by

$$\frac{\partial u(\boldsymbol{x}(\boldsymbol{X}, t), t)}{\partial t} = \frac{\partial u(\boldsymbol{X}, t)}{\partial t} - \frac{\partial u(\boldsymbol{X}, t)}{\partial X_j} \frac{\partial X_j}{x_i} \frac{\partial x_i}{\partial t}. \tag{2.22}$$

In the arbitrary Lagrangian–Eulerian (ALE) implementation used in this thesis we introduce the mapping from the stationary reference frame to the deforming physical domain by solving a Laplace equation for the velocity $\partial_t x_i$ of the nodes

$$\boldsymbol{\nabla}^2 \frac{\partial x_i}{\partial t}\bigg|_{\Omega'} = 0. \tag{2.23}$$

in the stationary reference frame. The dynamic boundary condition for the mesh velocity is that it can only be tangential to the boundary $\partial\Omega(t)$, or if we know the velocity or displacement explicitly, we may specify a Dirichlet condition.

In variational form the above equation becomes

$$-\int_{\Omega'} \boldsymbol{\nabla}\psi_i \cdot \boldsymbol{\nabla}\left(\frac{\partial x_i}{\partial t}\right) \mathrm{d}\boldsymbol{X} + \int_{\partial\Omega'} \psi_i \, \boldsymbol{n}' \cdot \boldsymbol{\nabla}\left(\frac{\partial x_i}{\partial t}\right) \mathrm{d}S = 0, \tag{2.24}$$

where ψ_i is the basis function for x_i.

2.2.2. Comsol and implementation

To implement the Naver–Stokes equations and the incompressibility constraint in Comsol we need to use the weak equation form if we want to solve the equations on a deforming mesh. Comsol have some support for specifying multiple reference frames which we can utilize to specify the equations and keeping track of the mapping from the stationary frame to the deforming frame defined by the fluid motion. In particular, if we tell Comsol that a variable is defined in a given frame, Comsol will internally multiply the integrands with the Jacobian according to Eq. (2.20). We still have to specify the equation for the mesh motion (2.23) as well as the derivatives in the moving frame in terms of the stationary coordinates (Eqs. (2.21) and (2.22)). This is very convenient since this allows us to specify the physical equations directly in the deforming frame without taking special care of the coordinate transformation to the stationary frame.

To describe the implementation of a moving ALE reference frame as well as Naver–Stokes and the continuity equation in Comsol we will use a simple model system: a viscous ellipse deforming due to surface tension. We know that such a system will minimize its surface area while conserving its volume. The final geometrical configuration of the model system is therefore a circle. At the same time this example allows us to discuss our implementation of the surface tension boundary condition used in the modeling of the film drawing process in chapter 3.

2.2.3. Verification: relaxation of a deformed body

In this section we will use the implementation of a 2d viscous ellipse deforming due to surface tension to verify the numerical implementation used to model

the process of drawing films from a bath of Newtonian liquid. Both systems are defined in domains deforming in time and surface tension is an important boundary condition. The initial configuration of the model system is an ellipse with semi axis a and b, see figure 2.2(a). We will discuss the implementation in some detail as the main points are equally valid for the implementation of the film drawing process. However, the simple geometry allows for a more clear description of the important details. In particular, the equations for the deforming mesh and the implementation of surface tension at the free boundary is identical to the one used in chapter 3. We will discuss the additional boundary conditions necessary for the film drawing problem in chapter 3.

We want to solve the fluid motion in terms of the velocity field $\boldsymbol{u}$ and pressure p in a domain $\boldsymbol{x} \in \Omega(t)$ deforming in time and moving with respect to a stationary domain $\boldsymbol{X} \in \Omega'$. First, we therefor set up the two reference frames and define the equations for smoothing the mesh in the deformed physical domain. In code listing 2.3 we show how the the stationary reference frame Ω' (`ref`) with coordinates `X` and `Y` and the deforming frame $\Omega(t)$ (`ale`) with coordinates `x` and `y` are set up using Comsol.

```
%% Frame specifications
fem.frame = {'ref','ale'};
fem.sdim = {{'X','Y'},{'x','y'}};
fem.meshtime = 'TIME';

clear sshape
sshape.dvolname = 'dvol';
sshape.frame = 'ref';
sshape.sorder = 2;
sshape.type = 'fixed';
fem.sshape{1} = sshape;

clear sshape
sshape.dvolname = 'dvol_ale';
sshape.frame = 'ale';
sshape.sorder = 2;
sshape.type = 'moving_abs';
sshape.refframe = 'ref';
fem.sshape{2} = sshape;
```

Listing 2.3: Implementation of two reference frames in Comsol.

We use the Laplace equation (2.23) to smooth the mesh in the nondimensionalized deforming frame

$$\boldsymbol{\nabla}^2 \frac{\partial x_i}{\partial t}\bigg|_{\Omega'} = 0, \qquad \text{in } \Omega', \tag{2.25}$$

where the overbars to denote dimensionless variables have been dropped for clarity. The motion of the mesh in the bulk of the domain is free but at the boundaries we require that the mesh nodes move only tangential to the surface

$$\boldsymbol{n} \cdot (\boldsymbol{u} - \partial_t \boldsymbol{x}) = 0 \qquad \text{at } \partial\Omega', \tag{2.26}$$

where $\boldsymbol{u}$ is the fluid velocity field found from solving the governing equations for the flow and $\boldsymbol{n}$ is an outward normal vector on the *deformed* domain. We could specify this equation and boundary condition using the Comsol general equation form. However, as explained in section 2.1.2.1, specifying equation (2.26) as an ideal constraint would make the condition influence both the motion of the fluid and the motion of the mesh. This is not what we want because only the fluid motion is physical. We want the coupling between the fluid velocity field and the velocity of the mesh nodes to go from the fluid to the mesh and not the other way. Therefore we must use the weak equation form and use a non-ideal constraint to specify the boundary condition. We do this by introducing a Lagrange multiplier λ at the boundary. In variational form the equation for the motion of the mesh and the boundary condition therefore reads

$$0 = \int_{\Omega'} \boldsymbol{\nabla}\boldsymbol{x} \colon \boldsymbol{\nabla}(\partial_t \boldsymbol{x}) \, \mathrm{d}\boldsymbol{X} + \int_{\partial\Omega'} \tilde{\lambda}\, \boldsymbol{n} \cdot (\boldsymbol{u} - \partial_t \boldsymbol{x}) \, \mathrm{d}S + \int_{\partial\Omega'} \tilde{\boldsymbol{x}} \cdot (\lambda \boldsymbol{n}) \, \mathrm{d}S. \tag{2.27}$$

The solution to this equation defines the domain $\Omega(t)$ in which we wish to solve the fluid motion. The motion of the incompressible fluid is governed by the full Naver–Stokes equation (2.6) and equation (2.7)

$$Re\big(\partial_t \boldsymbol{u} + (\boldsymbol{u} \cdot \boldsymbol{\nabla})\boldsymbol{u}\big) = \boldsymbol{\nabla} \cdot \boldsymbol{\sigma}, \qquad \text{in } \Omega(t), \tag{2.28}$$

$$0 = \boldsymbol{\nabla} \cdot \boldsymbol{u}, \qquad \text{in } \Omega(t). \tag{2.29}$$

Again we have dropped the overbar on the dimensionless variables for clarity. Due to surface tension γ and the curvature κ of the free surface, the boundary will be subjected to a force

$$\boldsymbol{n} \cdot \boldsymbol{\sigma} = \frac{1}{Ca} \left(\gamma \kappa \boldsymbol{n} + \boldsymbol{\nabla}_s \gamma \right), \tag{2.30}$$

where the capillary number $Ca = \eta_0 u_0 / \gamma_0$ is the ratio between viscous forces and surface tension. The first term on the right hand side of the equation is due to the Young-Laplace pressure caused by surface tension while the second term on the right hand side is the Marangoni force due to gradients in the surface tension along the free interface. Here we denote the surface gradient operator as

$$\boldsymbol{\nabla}_s = \boldsymbol{T}(\boldsymbol{T} \cdot \boldsymbol{\nabla}) = \boldsymbol{T}\partial_s, \tag{2.31}$$

where $\boldsymbol{T}$ is a unit tangent vector to the surface. In case of a constant surface tension, the Manangoni force vanishes. We include the Marangoni force in the description of our implementation as it is elegantly included in the formulation we have developed.

Equation (2.28) and equation (2.29) are also implemented using the weak equation form. In variational form the equations read

$$\begin{aligned}\int_{\Omega(t)} Re\, \tilde{\boldsymbol{u}} \cdot \partial_t \boldsymbol{u} \, \mathrm{d}\boldsymbol{x} = &- \int_{\Omega(t)} [\boldsymbol{\nabla}\tilde{\boldsymbol{u}} \colon \boldsymbol{\nabla}\boldsymbol{\sigma} + Re\, \tilde{\boldsymbol{u}} \cdot (\boldsymbol{u} \cdot \boldsymbol{\nabla})\boldsymbol{u}] \, \mathrm{d}\boldsymbol{x} \\ &+ \int_{\partial\Omega(t)} \tilde{\boldsymbol{u}} \cdot (\boldsymbol{n} \cdot \boldsymbol{\sigma}) \, \mathrm{d}s,\end{aligned} \tag{2.32}$$

$$0 = \int_{\Omega(t)} \tilde{p} \boldsymbol{\nabla} \cdot \boldsymbol{u} \, \mathrm{d}\boldsymbol{x}. \tag{2.33}$$

To enforce the boundary condition at the free surface we substitute equation (2.30) into the boundary integral in equation (2.32). Upon substitution the boundary integral becomes

$$\int_{\partial\Omega(t)} \tilde{\boldsymbol{u}} \cdot (\boldsymbol{n} \cdot \boldsymbol{\sigma}) \, \mathrm{d}s = \frac{1}{Ca} \int_{\partial\Omega(t)} \tilde{\boldsymbol{u}} \cdot (\gamma\kappa\boldsymbol{n} + \boldsymbol{\nabla}_s\gamma) \, \mathrm{d}s. \tag{2.34}$$

We could implement this directly in COMSOL but we would then need to find the curvature κ ether from geometrical reconstruction [22] or by calculating it using (in 2D with $\boldsymbol{x} = [x, y]$)

$$\kappa = \frac{\dot{x}\ddot{y} - \dot{y}\ddot{x}}{(\dot{x}^2 + \dot{y}^2)^{3/2}}, \tag{2.35}$$

where the dot denotes differentiation with respect to the arc-length parameter s. This however requires calculation of higher-order derivatives at the boundary which is not numerically accurate. Instead we use a different approach. Using the Serret–Frenet formula relating the tangent vector $\boldsymbol{T}$ to the curvature κ and normal vector $\boldsymbol{n}$ to a surface [1]

$$\partial_s \boldsymbol{T} = \kappa \boldsymbol{n}, \tag{2.36}$$

we can rewrite the right hand side of equation (2.34) as

$$\frac{1}{Ca} \int_{\partial\Omega(t)} \tilde{\boldsymbol{u}} \cdot (\gamma\partial_s\boldsymbol{T} + \boldsymbol{\nabla}_s\gamma) \, \mathrm{d}s. \tag{2.37}$$

Integration by parts then gives us

$$\frac{1}{Ca}\int_{\partial\Omega(t)}\left(-\boldsymbol{T}\cdot\partial_s(\gamma\tilde{\boldsymbol{u}})+\tilde{\boldsymbol{u}}\cdot\boldsymbol{\nabla}_s\gamma\right)\mathrm{d}s \tag{2.38a}$$

$$=\frac{1}{Ca}\int_{\partial\Omega(t)}\left(-\gamma\boldsymbol{T}\cdot\partial_s\tilde{\boldsymbol{u}}-\tilde{\boldsymbol{u}}\cdot\boldsymbol{T}\partial_s\gamma+\tilde{\boldsymbol{u}}\cdot\boldsymbol{\nabla}_s\gamma\right)\mathrm{d}s \tag{2.38b}$$

$$=\frac{1}{Ca}\int_{\partial\Omega(t)}\left(-\gamma\boldsymbol{T}\cdot\partial_s\tilde{\boldsymbol{u}}-\tilde{\boldsymbol{u}}\cdot\boldsymbol{\nabla}_s\gamma+\tilde{\boldsymbol{u}}\cdot\boldsymbol{\nabla}_s\gamma\right)\mathrm{d}s \tag{2.38c}$$

$$=-\frac{1}{Ca}\int_{\partial\Omega(t)}\gamma\boldsymbol{\nabla}_s\cdot\tilde{\boldsymbol{u}}\,\mathrm{d}s. \tag{2.38d}$$

Here we have used that the free surface in the model problem we are considering in this section does not have any end-points. If that were the case as in chapter 3 we would have to add contributions to the end points of the boundary. Implementation of the free boundary condition using equation (2.38d) instead of the original formulation in terms of the curvature provides several advantages: we do not need to calculate the curvature of the interface explicitly and the Marangoni effect is included automatically. In addition, all terms in the reformulated boundary integral are available in Comsol as internal variables. In particular, the components of the surface gradient operator working on a variable `u` is available as `uTx` and `uTy`, respectively.

The governing equations and free surface boundary conditions rewritten in a form suitable for implementation in Comsol therefore reads

$$\begin{aligned}\int_{\Omega(t)}Re\,\tilde{\boldsymbol{u}}\cdot\partial_t\tilde{\boldsymbol{u}}\,\mathrm{d}\boldsymbol{x}=&-\int_{\Omega(t)}\left[\boldsymbol{\nabla}\tilde{\boldsymbol{u}}\colon\boldsymbol{\nabla}\boldsymbol{\sigma}+Re\,\tilde{\boldsymbol{u}}\cdot(\boldsymbol{u}\cdot\boldsymbol{\nabla})\boldsymbol{u}\right]\mathrm{d}\boldsymbol{x}\\&-\frac{1}{Ca}\int_{\partial\Omega(t)}\gamma\boldsymbol{\nabla}_s\cdot\tilde{\boldsymbol{u}}\,\mathrm{d}s\end{aligned} \tag{2.39}$$

$$0=\int_{\Omega(t)}\tilde{p}\boldsymbol{\nabla}\cdot\boldsymbol{u}\,\mathrm{d}\boldsymbol{x}. \tag{2.40}$$

To implement the equations in Comsol we first need to declare in which domain each of the dependent variables are defined. This is done when specifying the shape functions, see code listing 2.4.

```
%% Shape functions
fem.shape = { ...
    'shlag(''order'',2,''basename'',''x'',''frame'',''ref'')', ...
    'shlag(''order'',2,''basename'',''y'',''frame'',''ref'')', ...
    'shlag(''order'',2,''basename'',''u'',''frame'',''ale'')', ...
    'shlag(''order'',2,''basename'',''v'',''frame'',''ale'')', ...
```

```
    'shlag(''order'',1,''basename'',''p'',''frame'',''ale'')', ...
    'shlag(''order'',2,''basename'',''lm'',''frame'',''ref'')'};
```

Listing 2.4: Specification og shape functions for the coordinates `x` and `y` of the deforming frame and the pressure `p` and velocity components `u` and `v` as well as the Lagrange multiplier `lm` used to enforce the boundary condition on the mesh motion.

When Comsol knows in which frame each dependent variable resides, we simply specify the equations on that domain. We do not have to multiply with the Jacobian as discussed in section 2.2.1 because Comsol has been informed through the shape function definitions in which domain each variable are to be solved. The bulk part of equations (2.27), (2.39) and (2.40) are then implemented as shown in code listing 2.5. We use the coordinates `X` and `Y` of the stationary frame as initial conditions for the coordinates `x` and `y` of the deformed frame to ensure that the two coordinate systems are identical at the onset of the simulations.

```
% Subdomain settings
fem.equ.dim = {'x','y','u','v','p'};
fem.equ.init = {{'X';'Y';0;0;0}};
fem.equ.dweak = {{0;0;'Re*ut*test(u)';'Re*vt*test(v)';0}};
fem.equ.weak = {{ ...
    'xXt*test(xX)+xYt*test(xY)'; ...
    'yXt*test(yX)+yYt*test(yY)'; ...
    '-(sigmaxx*test(ux)+sigmaxy*test(uy))-Re*(u*ux+v*uy)*test(u)'; ...
    '-(sigmayx*test(vx)+sigmayy*test(vy))-Re*(u*vx+v*vy)*test(v)'; ...
    '(ux+vy)*test(p)'}};
```

Listing 2.5: Implementation of Naver–Stokes equation in a deforming reference frame.

The implementation of the boundary conditions are very similar to the implementation of the bulk terms, see code listing 2.6. In addition to the dependent variables solved for in the bulk of the domain we also solve for the Lagrange multiplier `lm` at the boundary of the domain.

```
% Boundary settings
fem.bnd.dim = {'x','y','u','v','p','lm'};
fem.bnd.weak = { ...
    {'test(x*nx)*lm';'test(y*ny)*lm'; ...
```

```
    '-1/Ca*test(uTx)';'-1/Ca*test(vTy)'; ...
    '0';'test(lm)*(nx*(u-xt)+ny*(v-yt))'}};
```

Listing 2.6: Implementation of a free boundary with surface tension.

The derivatives in the deforming `ale` frame must be defined in terms of the chain rules (2.21) and (2.22). This is done by declaring them as expressions in the `struct` field `fem.expr`, see code listing 2.7. We could simply substitute them into the equations, but declaring commonly used expressions globally greatly reduces the risk of introducing typos in the code.

```
%% Expressions
fem.expr = { ...
    'sigmaxx','-p+2*ux','sigmaxy','vx+uy', ...
    'sigmayx','sigmaxy','sigmayy','(-p+2*vy)', ...
    'xt','xTIME','xtt','xTIMETIME',...
    'xXt','xXTIME','xYt','xYTIME',...
    'yt','yTIME','ytt','yTIMETIME',...
    'yXt','yXTIME','yYt','yYTIME',...
    'ut','uTIME-xTIME*ux-yTIME*uy',...
% and so on. See appendix for the remaining expressions
```

Listing 2.7: Expressions used to simplify the implementation of the equations.

With the described implementation we solve the system using the time dependent solver `femtime`. For the solution presented here we have used the the natural speed scale $u_0 = \gamma_0/\eta_0$ implying that the capillary number is $Ca = 1$. We imagine the fluid to be some viscous fluid. Typical characteristic physical scales could then be (parameter values corresponding to glycerin): density $\rho_0 = 1.3 \times 10^3\,\mathrm{kg/m^3}$, viscosity $\eta_0 = 1.5\,\mathrm{Pa\,s}$, surface tension $\gamma_0 = 63\,\mathrm{mN/m}$, characteristic size $r_0 = 2.5\,\mathrm{mm}$. With these parameter values the Reynolds number becomes $Re = \rho_0 u_0 r_0/\eta_0 \approx 0.1$.

The initial geometry used in the simulation is an ellipse with semiaxis 2 and $1/2$, see figure 2.2(a). Surface tension will minimize the surface area and the viscous ellipse therefore changes shape into a circle with radius 1, see figure 2.2(b) and figure 2.3(b). The dynamic condition that the mesh nodes moves only tangential to the free surface, equation (2.26), together with the incompressibility condition ensures that the area $A(t)$ given by the integral

$$A(t) = \int_{\Omega(t)} 1\,\mathrm{d}\boldsymbol{x} \tag{2.41}$$

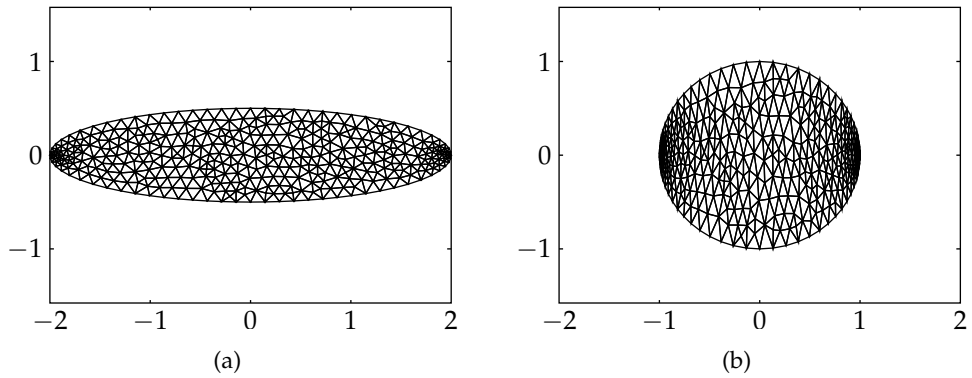

Figure 2.2.: (a) The initial meshed geometry. The simiaxis of the ellipse are 2 and 1/2. (b) The mesh in the deformed geometry after surface tension has minimized the surface area.

is constant within the numerical accuracy throughout the simulation, see figure 2.3(a).

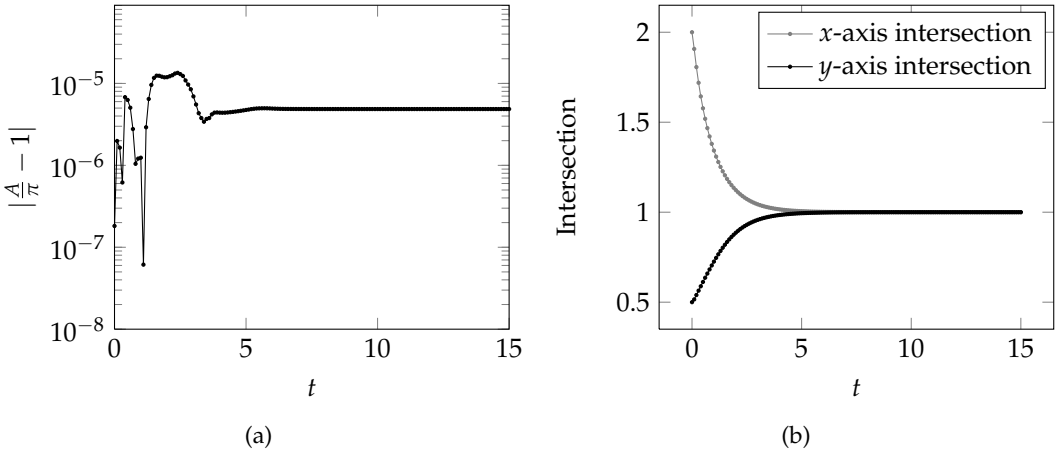

Figure 2.3.: (a) The area of the computational domain is constant within the numerical accuracy. (b) The intersection of the free surface with the positive x-axis and the positive y-axis both converge to 1 as the surface tension minimizes the surface energy of the system.

The simulation results of the model problem gives us confidence that our Comsol implementation of the free surface with surface tension and Marangoni stresses as well as the implementation of a deforming reference frame using the ALE method works as intended. Our confidence in the presented implementation is further

strengthened by the results in chapter 3. In particular we note that the shape of the free surface during film drawing matches the analytical prediction in the quasi-static regime. We hope that the implementation presented here may aid in providing numerical simulation results to match future experimental results on the film-drawing experiment. In chapter 3 we present simulation results, using a similar numerical implementation, of the process of drawing liquid films from a bath of viscous Newtonian liquid.

3. Thin liquid films

We study the breakup height of liquid films drawn from a bath of pure Newtonian liquid. We derive an analytical prediction of the breakup height in the quasi-static limit for zero Reynolds number and low capillary number. We also implement an efficient algorithm for numerical simulation of the full free-surface problem and present results for the breakup dynamics in a wide range of the capillary number.

3.1. Introduction

Recently, van Nierop, Scheid and Stone [56] suggested an alternative to Frankel's law [38] for the initial film thickness of a liquid film withdrawn from a bath of liquid. The conventional derivation of Frankel's law is based on the assumption of a rigid and inextensible surface and a shear flow in the liquid, and is thus identical to that used in the Landau–Levich–Derjaguin problem, where a flat vertically oriented plate is with drawn from the bath, see e.g. [10, 25, 28].

In contrast, the alternative formulation relies on the assumption that the flow in the liquid film is extensional and that the free surfaces are extensible. The aim of the present chapter is to verify this assumption and to study the breakup dynamics by numerical simulations of the film drawing process. As sketched in Fig. 3.1, a typical experimental setup for drawing liquid films and measuring the film thickness consists of a bath from which a horizontal hydrophilic wire is lifted in the vertical direction [4, 30, 32, 38, 39].

In this chapter we first consider the well-known shape of a static liquid film of a pure Newtonian liquid [11]. For completeness and to establish our notation, we derive this shape. Based on this analysis we then study the flow in a liquid film drawn quasi-statically from a bath of liquid. When the pulling speed, measured in terms of the capillary number, exceeds a critical value that we determine in our analysis, the quasi-static analysis becomes invalid. Beyond this critical value we use numerical simulations to solve the full flow equations in the liquid film as a function of the capillary number.

3.2. Properties of a static film

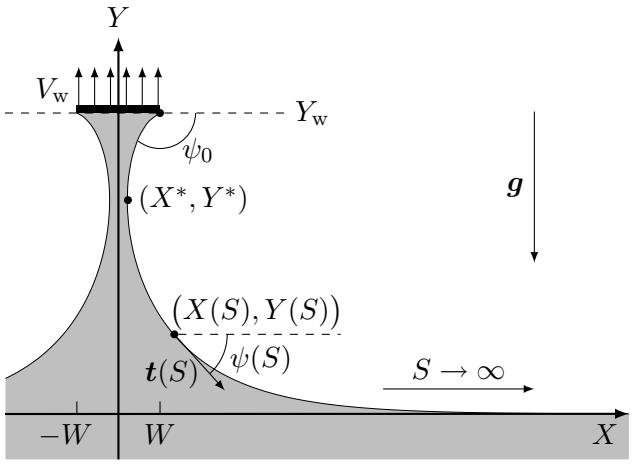

Figure 3.1.: The problem setup, here shown as a 2D cross section in the XY-plane, consists of a bath of pure Newtonian liquid (gray) from which a long (parallel to the Z-axis), hydrophillic wire of rectangular cross section (black) is lifted vertically up in the air (white) against gravity $\boldsymbol{g}$ with a speed V_w. The width of the wire is $2W$. The liquid surface is at rest at $Y = 0$ far away from the wire. As the wire is lifted to a height Y_w, the liquid sticks to its bottom plane, and the liquid/air interface, described by the curve $\big(X(S), Y(S)\big)$, forms an angle $\psi(S)$ between the surface tangent $\boldsymbol{t}(S)$ and the horizontal direction $\boldsymbol{e}_x$. Here S is the arc-length along the surface measured from the edge of the wire. The point on the surface at the thinnest part of the film is denoted (X^*, Y^*). The YZ-plane is a symmetry plane.

In the static limit, when the long horizontal wire is lifted to a given height Y_w, the shape of the free surface [25] of the liquid/air interface of the suspended liquid film is determined by a balance between surface tension γ and the hydrostatic pressure due to gravity ρg. For lift heights and wire widths comparable to or less than the capillary length $\ell_\mathrm{c} = \sqrt{\gamma/(\rho g)}$ this static balance is a stable equilibrium.

In a vertical 2D plane perpendicular to the axis of the wire, we introduce an XY-coordinate system as sketched in Figure 3.1. The characteristic length scale in the horizontal X-direction is the half-width W of the wire, while in the vertical Y-direction it is the capillary length ℓ_c. Consequently, the ratio ϵ between these

length scales becomes an important dimensionless parameter of the problem,

$$\epsilon = \frac{W}{\ell_c}. \tag{3.1}$$

To further simplify the mathematical analysis we change the X-coordinate to the dimensionless x-coordintate by use of the wire half-width W, while the Y-coordinate and the arc-length S of the interface in the XY-plane are changed into the dimensionless variables y and s, respectively, by use of the capillary length ℓ_c,

$$x = \frac{1}{W}\,X, \qquad y = \frac{1}{\ell_c}\,Y, \text{ and} \qquad s = \frac{1}{\ell_c}\,S. \tag{3.2}$$

3.2.1. The shape of the static interface

Initially, at time $t = 0$, both the bottom of the wire as well as the liquid/air interface is at $y = 0$. As the wire moves upward with a vanishingly low speed V_w, the liquid surface far away form the wire, $x \to \infty$, remains at $y = 0$, while the liquid is pulled up by the wire near $x = 0$. In the static limit, where the wire is at rest at the position y_w, the hydrostatic pressure $P_{hyd} = -\rho g Y$ inside the liquid is balanced by the Young–Laplace under-pressure $P_{st} = \gamma K_0$ due to the surface tension γ and the curvature K_0 of the liquid/air interface. Introducing the dimensionless pressure p and curvature κ by the hydrostatic pressure $\rho g \ell_c$ and the inverse capillary length $1/\ell_c$,

$$p_0 = \frac{1}{\rho g \ell_c}\,P, \qquad \text{and} \qquad \kappa_0 = \ell_c K_0 \tag{3.3}$$

the pressure balance $P_{hyd} = P_{st}$ is written

$$\kappa_0 = -y. \tag{3.4}$$

Here, the subscript 0 denotes the static case. The geometry of the surface leading to an expression for the curvature κ is best described by the angle $\psi(s)$ between the x-axis and the tangent vector $\boldsymbol{t}$ of the surface in the vertical plane in terms of the arc-length s,

$$\boldsymbol{t}(s) = \big(\cos\psi(s), -\sin\psi(s)\big) = \big(\epsilon\dot{x}(s), \dot{y}(s)\big). \tag{3.5}$$

Here, the dot signifies the derivative with respect to the dimensionless arc-length s. Now, since the curvature K is given by the arc-length derivative of the tangential angle, $K = \dot{\psi}/\ell_c$, substitution in (3.4) yields

$$\dot{\psi} = -y. \tag{3.6}$$

The chain rule $\dot{\psi} = (\mathrm{d}\psi/\mathrm{d}y)\dot{y}$ and $\dot{y} = -\sin\psi$ from Eq. (3.5) is then used to rewrite Eq. (3.6) as

$$-\sin\psi\,\mathrm{d}\psi = -y\,\mathrm{d}y. \tag{3.7}$$

By integration, using the boundary condition $\psi = 0$ for $y = \infty$, we then find y as a function of ψ,

$$y = 2\sin\left(\frac{\psi}{2}\right), \quad \text{for } 0 \leq \psi \leq 2\pi. \tag{3.8}$$

Substitution of this expression back into (3.6) yields $2\mathrm{d}s = -\mathrm{d}\psi/\sin(\psi/2)$, which by partial integration using the substitution $\ln\left[\tan(\psi/4)\right]$ results in

$$\psi(s) = 4\arctan\left[\tan\left(\frac{\psi_0}{4}\right)\mathrm{e}^{-s}\right], \tag{3.9}$$

where $\psi_0 = \psi(0)$ is the tangential angle of the surface where it attaches to the lower right corner of the wire.

From Eq. (3.9) we can obtain a parametric description of the liquid/air interface. The x-coordinate $x(s)$ is found by integration of the x-component of the tangent vector $\boldsymbol{t}(s)$ in Eq. (3.5) with respect to the arc-length s. Using the expressions $\cos\psi = 2\left[2\cos^2(\psi/4) - 1\right]^2 - 1$ and $\cos^2(\psi/4) = \left[1 + \tan^2(\psi/4)\right]^{-1} = \left[1 + \tan^2(\psi_0/4)e^{-2s}\right]^{-1}$ direct integration leads to

$$x(s) = 1 + \frac{1}{\epsilon}\left[s - 2\sin^2\left(\frac{\psi_0}{2}\right)\,\sinh(s)\,f(s)\right]. \tag{3.10a}$$

The y-coordinate is most easily found from Eq. (3.6) as $y(s) = -\dot{\psi}$ after insertion of Eq. (3.9),

$$y(s) = 2\sin\left(\frac{\psi_0}{2}\right)f(s). \tag{3.10b}$$

The function $f(s)$ in Eqs. (3.10a) and (3.10b) is given by

$$f(s) = \left[\cosh(s) + \sinh(s)\cos\left(\frac{\psi_0}{2}\right)\right]^{-1}. \tag{3.10c}$$

The integration constants are determined by requiring that $x(0) = 1$ and $y(\infty) = 0$. The angle ψ_0 at $s = 0$ is determined by the lift height $y(0) = y_\mathrm{w}$ so that

$$\psi_0 = 2\arcsin\left(\frac{y_\mathrm{w}}{2}\right). \tag{3.11}$$

Note that this expression requires $y_\mathrm{w} \leq 2$ and thus establishes the maximal lift height of the wire in the static case to be 2. As expected from the setup with the wire, the tangent angle of the interface is bounded by $\psi \leq \pi$.

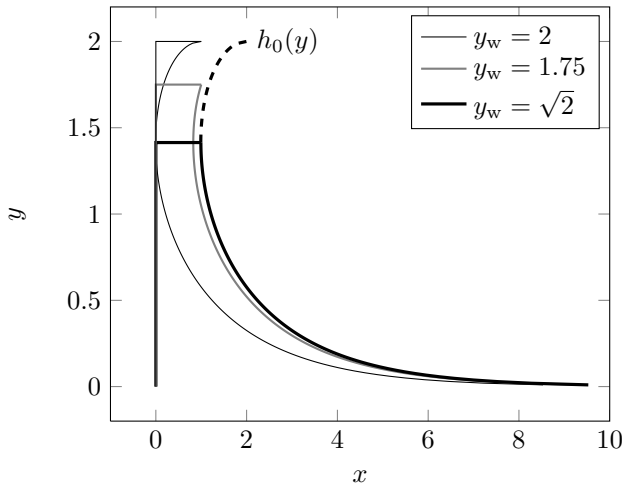

Figure 3.2.: The shape of the liquid film at three different lift heights in the static case. The lowest lift height yielding a vertical surface tangent at some point is $y_w = \sqrt{2}$ (thick black curve). The largest possible lift height in the static case is $y_w = 2$ (thin black curve). Any shape (gray curve) is given by a horizontal displacement to the left of the function $h_0(y)$ (dashed curve).

In Figure 3.2 we have plotted the shape of a static film for different lift heights of the wire. For any lift height y_w of the wire the half-width $h(y)$ of the film at height y is given by the function $h_0(y) = x\big(s(y)\big)$ upon a horizontal displacement to ensure the fulfillment of the boundary condition $\big(x(0), y(0)\big) = (1, y_w)$. We define $h_0(y)$ as the interface that passes through the point $(1, \sqrt{2})$. To determine this interface we consider $\psi_0 = \pi$, which by Eq. (3.10b) implies that $y(s) = 2/\cosh(s)$ or $s(y) = \operatorname{acosh}(2/y)$ and by Eq. (3.10a) yields $x\big(s(y)\big) = x_0 + \big[\operatorname{acosh}(2/y) - \sqrt{4-y^2}\big]$. So we find the shape of the liquid film

$$h_0(y) = x\big(s(y)\big) = 1 + \frac{1}{\epsilon}\left[\operatorname{acosh}\left(\frac{2}{y}\right) - \sqrt{4-y^2} - \operatorname{acosh}\sqrt{2} + \sqrt{2}\right]. \tag{3.12}$$

3.2.2. The breakup height of a static film

To discuss the breakup of a film in the static case, we introduce the coordinates (x^*, y^*) of the point on the surface where the thickness of the film is minimal, see figure 3.1. The corresponding value s^* of the arc-length s is given by the condition that the corresponding tangent angle $\psi(s^*)$ equals $\pi/2$, i.e. the tangent vector is

vertical. Insertion of $\psi(s^*) = \pi/2$ into (3.9) leads to

$$s^* = \ln\left[\frac{\tan\left(\frac{\psi_0}{4}\right)}{\tan\left(\frac{\pi}{8}\right)}\right]. \tag{3.13}$$

We note that a physical sensible solution $s^* \geq 0$ is only possible for $\psi_0 \geq \pi/2$, which according to Eq. (3.11) corresponds to large lift heights $y_w \geq \sqrt{2}$. For small lift heights $0 \leq y_w < \sqrt{2}$ the film is convex, and its most narrow part is at the wire position y_w, so we trivially get

$$(x^*, y^*) = (1, y_w), \text{ for } 0 \leq y_w < \sqrt{2}. \tag{3.14}$$

For the large lift heights, $\sqrt{2} \leq y_w \leq 2$, the point on the surface, where the film is thinnest, indeed does have a vertical tangent. Thus, it is given by $(x^*, y^*) = \big(x(s^*), y(s^*)\big)$, and from Eqs. (3.10b) and (3.13) follows

$$y^* = \sqrt{2}, \text{ for } \sqrt{2} \leq y_w \leq 2. \tag{3.15}$$

Consequently, once the lift height y_w is higher than $\sqrt{2}$ we have that y^* is constant and equal to $\sqrt{2}$. From Eq. (3.10a) it follows after a bit of tedious algebra that

$$x^*(\epsilon, y_w) = \frac{1}{\epsilon}\left[\ln\left(\frac{(1+\sqrt{2})y_w}{2+\sqrt{4-y_w^2}}\right) + \sqrt{4-y_w^2} - \sqrt{2}\right] + 1, \quad \text{for } \sqrt{2} \leq y_w \leq 2, \tag{3.16}$$

and we see that the thinnest half-width x^* of the film depends on both the wire width ϵ and the lift height y_w.

The breakup point of a static film is determined by setting $x^*(\epsilon, y_{wb}) = 0$ in Eq. (3.16). Through this expression we can find the relation between a given wire thickness ϵ and the lowest lift height y_{wb} at which the film attached to this wire breaks, i.e. the lift height up to which a static film can exist,

$$\epsilon = \sqrt{2} - \sqrt{4 - y_{wb}^2} - \ln\left(\frac{(1+\sqrt{2})y_{wb}}{2+\sqrt{4-y_{wb}^2}}\right). \tag{3.17}$$

In Fig. 3.3 is shown some plots of x^* as a function of the lift height y_w for four different wire widths ϵ. The breakup lift height y_{wb} of the wire, where the film breaks, can be read off as the intersections of the four graphs with the y_w-axis. We note that the higher the wire width the higher the lift height y_{wb}. Since the highest possible lift height is $y_w = 2$ the width ϵ_{max} of the widest possible wire allowing for a static solution just reaching the breakup point is given by $x^*(\epsilon_{max}, 2) = 0$ from which we find

$$\epsilon_{max} = \sqrt{2} - \ln(1+\sqrt{2}) \approx 0.5328. \tag{3.18}$$

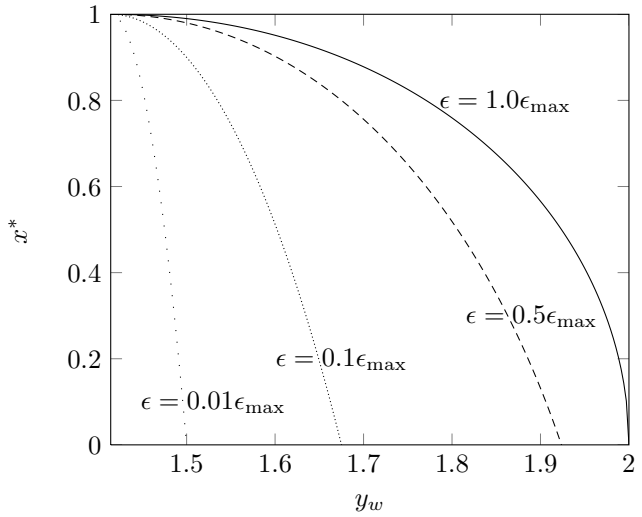

Figure 3.3.: The minimum film thickness x^* of the static film as a function of the lift height y_w of the wire for different wire widths ϵ. The maximum width of the wire for which a static solution exists is $\epsilon_{\max} = \sqrt{2} - \ln(1+\sqrt{2}) \approx 0.5328$.

3.3. Properties of a quasi-static film

We now study the effect of a steady, small but non-zero pulling speed V_w. Provided we draw the wire sufficiently slowly from the bath of liquid, we expect that as the wire passes any height $y_w \leq 2$, the shape of the liquid film under the wire is equal to that of a static film with its wire positioned at a corresponding height. To analyze the properties of quasi-static films we therefore use the solution to the static film problem as a starting point and expand the governing equations in the small pulling speed.

The quasi-static limit is defined by a non-zero, vertical withdrawal velocity V_w, which, however, is so small that the dynamic stress-induced pressure of order $\eta V_w/\ell_c$ is much smaller than the hydrostatic pressure $\rho g \ell_c$, i.e. $V_w \ll \gamma/\eta$. In terms of a dimensionless perturbation parameter α we can thus write

$$V_w = \alpha \frac{\gamma}{\eta}, \text{ for } \alpha \ll 1, \tag{3.19}$$

and we note that α can be interpreted as the capillary number Ca of the system,

$$\alpha = \frac{\eta V_w}{\gamma} = Ca. \tag{3.20}$$

The characteristic time scale in the problem is ℓ_c/V_w, so the dimensionless time t and velocity (u_1, v_1) representing the physical time T and velocity (U, V) become

$$t = \frac{V_w}{\ell_c}\,T \quad \text{and} \quad (u_1, v_1) = \frac{1}{V_w}\left(\frac{1}{\epsilon}U, V\right). \tag{3.21}$$

Here, the subscript 1 indicates that the velocity components, due to the linearity of the Stokes equation, are proportional the imposed pulling speed to the first power. Similarly, the pressure p is written as the sum of the hydrostatic pressure p_0 and the dynamic pressure αp_1, while the film half-width h, given by $\big(x(s), y(s)\big) = \big(h(y), y\big)$, is the sum of the static half-width h_0 and the quasi-static change αh_1,

$$p = p_0 + \alpha p_1, \tag{3.22a}$$
$$h = h_0 + \alpha h_1. \tag{3.22b}$$

The starting position at time $t = 0$ is when the lift height is $y_w = \sqrt{2}$ and the film shape is $h_0(y)$, see Eq. (3.12) and the thick black line in Fig. 3.2. From this starting position the lift height then changes linearly in time,

$$y_w(t) = \sqrt{2} + \alpha t, \tag{3.23a}$$
$$h\big(y_w(t)\big) = 1. \tag{3.23b}$$

3.3.1. Quasi-static dimensionless equations of motion

The non-dimensionalized Stokes and continuity equation governing the first-order fields u_1, v_1 and p_1 in the quasi-static limit of the incompressible liquid film are,

$$0 = \quad -\partial_x p_1 + \partial_x^2 u_1 + \epsilon^2 \partial_y^2 u_1, \tag{3.24a}$$
$$0 = -\epsilon^2 \partial_y p_1 + \partial_x^2 v_1 + \epsilon^2 \partial_y^2 v_1, \tag{3.24b}$$
$$0 = \quad \partial_x u_1 + \partial_y v_1. \tag{3.24c}$$

These equations must be solved subject to the following boundary conditions. At the symmetry line at $x = 0$ we have no tangential stress and the velocity component perpendicular to the boundary must vanish,

$$\partial_x v_1 = 0 \quad \text{and} \quad u_1 = 0, \quad \text{for } x = 0. \tag{3.25}$$

At the wire, $y = y_w$, we have a no-slip condition and the constant film half-width $h(1, t) = h_0(1) = 1$

$$u_1 = 0, \quad v_1 = 1, \quad \text{and} \quad h_1 = 0, \quad \text{for } y = y_w. \tag{3.26}$$

At the free surface, $\big(x(s), y(s)\big) = \big(h(y), y\big)$, the surface normal $\boldsymbol{n}(y)$ is given by

$$\boldsymbol{n}(y) = \big(1, -\epsilon \partial_y h(y)\big) + \mathcal{O}\big(\epsilon^2\big). \tag{3.27}$$

Moreover, in contrast to the $1/\ell_c$-scaling of the static curvature K_0, the dynamic correction K_1 to the Young–Laplace pressure scales as h/ℓ_c^2 which in dimensionless units becomes $\epsilon\kappa_1$. The boundary conditions at the free surface, given by a surface tension induced stress and by conservation of mass, are therefore written as

$$-p_1 + 2\partial_x u_1 - \big(\partial_x v_1 + \epsilon^2 \partial_y u_1\big)\partial_y h = \frac{\epsilon}{\alpha}\,\kappa_1, \tag{3.28a}$$

$$-p_1 + \partial_x v_1 + \epsilon^2(\partial_y u_1 - 2\partial_y v_1\,\partial_y h) = -\frac{\epsilon^3}{\alpha}\kappa_1\,\partial_y h, \tag{3.28b}$$

$$\partial_t h = u_1 - v_1\,\partial_y h. \tag{3.28c}$$

3.3.2. First-order quasi-static film dynamics

The quasi-static film dynamics is now studied to first order in both the capillary number α and the width ratio ϵ. We find the equation system to be

$$0 = -\partial_x p_1 + \partial_x^2 u_1, \tag{3.29a}$$

$$0 = \partial_x^2 v_1, \tag{3.29b}$$

$$0 = \partial_x u_1 + \partial_y v_1, \tag{3.29c}$$

subject to the boundary conditions for the symmetry line $x = 1$ and the wire $y = 1$, Eqs. (3.25) and (3.26) respectively, together with the free-surface condition (3.28) expanded to first order in ϵ:

$$-p_1 + 2\partial_x u_1 - \partial_y h_0 \partial_x v_1 = \frac{\epsilon}{\alpha}\kappa_1, \tag{3.30a}$$

$$\partial_x v_1 = 0, \tag{3.30b}$$

$$\partial_t h_1 = u_1 - v_1 \partial_y h_0. \tag{3.30c}$$

In the limit of very slow pulling speed, $\alpha \ll \epsilon$ we note that the left hand side of (3.30a) is negligible,

$$\kappa_1 = 0, \text{ for } \alpha \ll \epsilon. \tag{3.31}$$

Consequently, the shape of the quasi-static liquid film is simply given by a time-dependent shift of the static solution $h_0(y)$ of Eq. (3.12) to fulfill the boundary

condition (3.23) for $h\big(y_w(t),t\big)$ at the wire position. Thus, the change in film half-width is $\alpha h_1 = 1 - h_0(\sqrt{2}+\alpha t)$, or

$$\alpha h_1 = \frac{1}{\epsilon}\left[\sqrt{4-(\sqrt{2}+\alpha t)^2} - \sqrt{2} + \operatorname{acosh}(\sqrt{2}) - \operatorname{acosh}\left(\frac{2}{\sqrt{2}+\alpha t}\right)\right] \approx -\frac{(\alpha t)^2}{\sqrt{2}\epsilon}. \tag{3.32}$$

Concerning the first-order velocity field, it follows from (3.29b) and the boundary conditions at the symmetry line and the free surface that v_1 is independent of x,

$$v_1 = v_1(y,t), \tag{3.33}$$

implying that the flow is purely extensional as argued in Ref. [56]. Moreover, by integration of the continuity equation (3.29c) it follows that u_1 has the form

$$u_1 = -x\,\partial_y v_1. \tag{3.34}$$

3.4. Dynamic properties of a film, numerical implementation in Comsol

In order to investigate the breakup height as a function of the pulling velocity outside the quasi-static regime, we solve the problem using the finite element method based software package Comsol Multiphysics 3.4 [7].

As mentioned, simulation of the film drawing process involves several challenging problems. One challenge is the boundary condition at the free surface which depends on the curvature of the liquid-gas interface. Direct calculation of the curvature involves second order derivatives along the boundary which can lead to numerical inaccuracy. As discussed in section 2.2.3, we have solved this problem by projecting the curvature calculation onto the velocity test functions. Another challenge involves updating the computational domain as its shape changes with time. We have used an Arbitrary Lagrangian-Eulerian (ALE) reference frame which is solved for simultaneously with the governing physical equations. In this section we will discuss the implementation of the film-drawing problem. The boundary condition at the free surface have been discussed earlier and will but is included in this discussion to highlight the specific additional details considered in the film drawing geometry. In particular, we have contributions at the end-points of the free boundary. These end-point conditions can be used to specify a contact angle if needed. We also discuss the symmetry boundary condition used to reduce the size of the computational domain, the no-slip condition at the wire and the hydro static pressure condition enforced bottom of the computational domain.

To simplify the Comsol implementation, we use the width of the wire as the only length scale when nondimensionalizing the equation system, i.e. we use W as the length scale in the y-direction as well as the x-direction. The nondimensionalized Stokes equation then reads

$$0 = \alpha\, \boldsymbol{\nabla} \cdot \boldsymbol{\sigma} - \epsilon^2 \boldsymbol{e}_y. \tag{3.35}$$

The components of the Cauchy stress tensor are

$$\sigma_{ji} = -\delta_{ij} p + \partial_j u_i + \partial_i u_j. \tag{3.36}$$

This equation must be solved together with the incompressibility condition

$$0 = \boldsymbol{\nabla} \cdot \boldsymbol{u}. \tag{3.37}$$

3.4.1. Weak form

To solve (3.35) and (3.37) with Comsol we state them in weak form. To do so, we multiply the equations with a test function and integrate over the computational domain. The weak form of the incompressibility condition is simply

$$0 = \int_\Omega \tilde{p}\, \boldsymbol{\nabla} \cdot \boldsymbol{u}\, \mathrm{d}\boldsymbol{r}, \tag{3.38}$$

where the tilde denotes the test function used to interpolate the solution over each mesh element.

The weak form of Stokes equation is obtained in a similar fashion

$$0 = \int_\Omega \tilde{\boldsymbol{u}} \cdot (\alpha\, \boldsymbol{\nabla} \cdot \boldsymbol{\sigma} - \epsilon^2 \boldsymbol{e}_y)\, \mathrm{d}\boldsymbol{r}. \tag{3.39}$$

By integrating by parts we can get rid of the divergence of the stress tensor

$$0 = -\int_\Omega \left[\alpha\, \boldsymbol{\nabla}\tilde{\boldsymbol{u}} : \boldsymbol{\sigma} + \epsilon^2\, \tilde{\boldsymbol{u}} \cdot \boldsymbol{e}_y\right] \mathrm{d}\boldsymbol{r} + \int_{\partial\Omega} \alpha\, \tilde{\boldsymbol{u}} \cdot (\boldsymbol{n} \cdot \boldsymbol{\sigma})\, \mathrm{d}s, \tag{3.40}$$

where the colon is the dyadic product defined as $\boldsymbol{\nabla}\tilde{\boldsymbol{u}} : \boldsymbol{\sigma} = (\partial_j \tilde{u}_i)\sigma_{ij}$. This form provides a form of the equations that allows us to specify boundary conditions.

3.4.2. Boundary conditions

There are four different types of boundary conditions in the problem:

$\partial\Omega_1$: the fixed film drawing velocity at the wire,

$\partial\Omega_2$: the free surface with surface tension,

$\partial\Omega_3$: a hydrostatic pressure in the bulk fluid, and

$\partial\Omega_4$: a symmetry boundary condition in the center of the liquid film.

3.4.2.1. The rectangular wire

The wire is drawn from the bath at a fixed velocity $V_w \boldsymbol{e}_y$. We have no-slip at the wire, so the fluid velocity is

$$\boldsymbol{u}_{\text{wire}} = V_w \boldsymbol{e}_y. \tag{3.41}$$

We enforce this boundary condition by introducing a Lagrange multiplier vector $\boldsymbol{\lambda}$ and adding a weak contribution to (3.40) at the wire boundary

$$\int_{\partial\Omega_1} \left[\tilde{\boldsymbol{\lambda}} \cdot (\boldsymbol{u} - \boldsymbol{u}_{\text{wire}}) + \tilde{\boldsymbol{u}} \cdot \boldsymbol{\lambda}\right] \, \mathrm{d}s. \tag{3.42}$$

3.4.2.2. Free surface

The implementation of the free surface boundary condition is almost identical to that used in the example in section 2.2.3. Surface tension exerts a stress at the free boundary

$$\alpha \, \boldsymbol{n} \cdot \boldsymbol{\sigma} = \gamma \kappa \boldsymbol{n}. \tag{3.43}$$

Direct calculation of the curvature involves higher order derivatives which we wish to avoid in order to improve the quality of the simulation results. The Serret–Frenet formula relating the arc-length derivative of the tangent vector to the product of the curvature and the normal vector can be used to rewrite (3.43) as

$$\alpha \, \boldsymbol{n} \cdot \boldsymbol{\sigma} = \partial_s(\gamma \boldsymbol{t}), \tag{3.44}$$

where s is the arc-length parameter along the boundary. Substituting this equation into the boundary term in (3.40) we obtain

$$\int_{\partial\Omega_2} \alpha \, \tilde{\boldsymbol{u}} \cdot (\boldsymbol{n} \cdot \boldsymbol{\sigma}) \, \mathrm{d}s = \int_{\partial\Omega_2} \tilde{\boldsymbol{u}} \cdot \partial_s(\gamma \boldsymbol{t}) \, \mathrm{d}s. \tag{3.45}$$

Using integration by parts we obtain a form of the free boundary condition suitable for use in our simulations

$$\int_{\partial\Omega_2} \tilde{\boldsymbol{u}} \cdot \partial_s(\gamma \boldsymbol{t}) \, \mathrm{d}s = -\int_{\partial\Omega_2} \gamma \, (\boldsymbol{t} \cdot \partial_s \tilde{\boldsymbol{u}}) \, \mathrm{d}s + \sum_P \tilde{\boldsymbol{u}} \cdot (\gamma \boldsymbol{t}). \tag{3.46}$$

The summation is over the end-points of the boundary. This sum was not included in the verification example discussed earlier because the perimeter of the viscous body had no end-points. Specifying a specific tangent vector at the end-points can be used to set a condition involving a contact angle. We have now expressed the boundary condition at the free surface, which in its original form included higher order derivatives, in terms of the velocity test functions and the tangent vector. These are all available directly during the numerical problem solving.

3.4.2.3. Hydrostatic pressure

In the bulk fluid far away from the free meniscus a hydrostatic pressure builds up and the viscous stresses are zero. The hydrostatic pressure is in dimensionless form

$$p_{\mathrm{hs}} = -\epsilon^2 y, \tag{3.47}$$

which we substitute in (3.40) to obtain the weak boundary contributions at hydrostatic pressure boundaries

$$\int_{\partial\Omega_3} \alpha\, \tilde{\boldsymbol{u}} \cdot (\boldsymbol{n} \cdot \boldsymbol{\sigma})\, \mathrm{d}s = -\int_{\partial\Omega_3} \epsilon^2\, y\, \tilde{\boldsymbol{u}} \cdot \boldsymbol{n}\, \mathrm{d}s \tag{3.48}$$

3.4.2.4. Symmetry

At the symmetry boundary there are no horizontal velocity components, i.e. $\boldsymbol{n} \cdot \boldsymbol{u} = 0$. This boundary condition is enforced by adding the weak contribution

$$\int_{\partial\Omega_4} \left[\tilde{\boldsymbol{\lambda}} \cdot \boldsymbol{n}(\boldsymbol{n} \cdot \boldsymbol{u}) + \tilde{\boldsymbol{u}} \cdot \boldsymbol{\lambda}\right]\, \mathrm{d}s \tag{3.49}$$

at the boundary.

Thus, the equation system with boundary conditions in weak form is

$$\begin{aligned} 0 = &-\int_{\Omega} \left[\alpha\, \boldsymbol{\nabla}\tilde{\boldsymbol{u}} \colon \boldsymbol{\sigma} + \epsilon^2\, \tilde{\boldsymbol{u}} \cdot \boldsymbol{e}_y\right] \mathrm{d}\boldsymbol{r} \\ &+ \int_{\partial\Omega_1} \left[\tilde{\boldsymbol{\lambda}} \cdot (\boldsymbol{u} - \boldsymbol{u}_{\mathrm{wire}}) + \tilde{\boldsymbol{u}} \cdot \boldsymbol{\lambda}\right]\, \mathrm{d}s \\ &- \int_{\partial\Omega_2} \gamma\, (\boldsymbol{t} \cdot \partial_s \tilde{\boldsymbol{u}})\, \mathrm{d}s \\ &- \int_{\partial\Omega_3} \epsilon^2\, y\, \tilde{\boldsymbol{u}} \cdot \boldsymbol{n}\, \mathrm{d}s \\ &+ \int_{\partial\Omega_4} \left[\tilde{\boldsymbol{\lambda}} \cdot \boldsymbol{n}(\boldsymbol{n} \cdot \boldsymbol{u}) + \tilde{\boldsymbol{u}} \cdot \boldsymbol{\lambda}\right]\, \mathrm{d}s \\ &+ \sum_P \tilde{\boldsymbol{u}} \cdot (\gamma \boldsymbol{t}) \end{aligned} \tag{3.50a}$$

$$0 = \int_{\Omega} \tilde{p}\, \boldsymbol{\nabla} \cdot \boldsymbol{u}\, \mathrm{d}\boldsymbol{r}. \tag{3.50b}$$

The Comsol implementation can be seen in appendix A.2.

3.4.3. ALE reference frame

Equations (3.50a) and (3.50b) are solved in an arbitrary Lagrangian–Eulerian (ALE) reference frame $\boldsymbol{x} \in \Omega$, as described in section 2.2.1. This frame of reference is

deforming with respect to a fixed computational frame $\boldsymbol{X} \in \Omega'$. The mesh is kept smooth in the bulk of the domain by solving a Laplace equation for the node velocities

$$0 = \nabla^2(\partial_t \boldsymbol{x}) \qquad \text{in } \Omega'. \tag{3.51}$$

In weak form we have

$$0 = -\int_{\Omega'} \boldsymbol{\nabla}\tilde{\boldsymbol{x}} \colon \boldsymbol{\nabla}(\partial_t \boldsymbol{x})\, \mathrm{d}\boldsymbol{r}' + \int_{\partial\Omega'} \tilde{\boldsymbol{x}} \cdot [\boldsymbol{n} \cdot \boldsymbol{\nabla}(\partial_t \boldsymbol{x})]\, \mathrm{d}s'. \tag{3.52}$$

The boundaries and the ALE reference frame follow the deformations of the fluid dictated by the physics of the system. Again we enforce the boundary conditions by introducing Lagrange multipliers $\boldsymbol{\varphi}$ and ϕ at the boundaries. This relaxes the Neumann-condition in (3.52) that we would otherwise need to specify.

On the surface of the rectangular wire $\partial\Omega'_1$ we fix the velocity of the mesh to the velocity of the wire. At the free surface we allow the mesh nodes to move tangential to the boundary, i.e. we have $\boldsymbol{n} \cdot (\partial_t \boldsymbol{x} - \boldsymbol{u}) = 0$ on $\partial\Omega'_2$ and finally, on boundary $\partial\Omega'_3$ and $\partial\Omega'_4$ we suppress the node displacement. The total equation system with boundary conditions for the deforming mesh is therefore

$$\begin{aligned} 0 = &-\int_{\Omega'} \boldsymbol{\nabla}\tilde{\boldsymbol{x}} \colon \boldsymbol{\nabla}(\partial_t \boldsymbol{x})\, \mathrm{d}\boldsymbol{X} \\ &+ \int_{\partial\Omega'_1} \tilde{\boldsymbol{\varphi}} \cdot (\partial_t \boldsymbol{x} - \boldsymbol{u}_{\text{wire}}) + \tilde{\boldsymbol{x}} \cdot \boldsymbol{\varphi}\, \mathrm{d}S \\ &+ \int_{\partial\Omega'_2} \tilde{\phi}\boldsymbol{n} \cdot (\partial_t \boldsymbol{x} - \boldsymbol{u}) + \tilde{\boldsymbol{x}} \cdot \boldsymbol{n}\phi\, \mathrm{d}S \\ &+ \int_{\partial\Omega'_3} \tilde{\boldsymbol{\varphi}} \cdot (\boldsymbol{x} - \boldsymbol{X}) + \tilde{\boldsymbol{x}} \cdot \boldsymbol{\varphi}\, \mathrm{d}S \\ &+ \int_{\partial\Omega'_4} \tilde{\boldsymbol{\varphi}} \cdot (\boldsymbol{x} - \boldsymbol{X}) + \tilde{\boldsymbol{x}} \cdot \boldsymbol{\varphi}\, \mathrm{d}S. \end{aligned} \tag{3.53}$$

3.4.4. Scripting in Comsol

The weak form of all the above mentioned equations is directly implemented in Comsol using the scripting capabilities. Thereby we obtain an easy way to run the various parameter scans, the results of which are shown in the following section.

3.5. Results

The above equation system is solved in Comsol for capillary numbers varying from $\alpha = 10^{-5}$ to $\alpha = 1$ with a wire half-width of $\epsilon = 10^{-2}$. For each simulation, in accordance with Eq. (3.23), the initial lift height and surface shape has been set

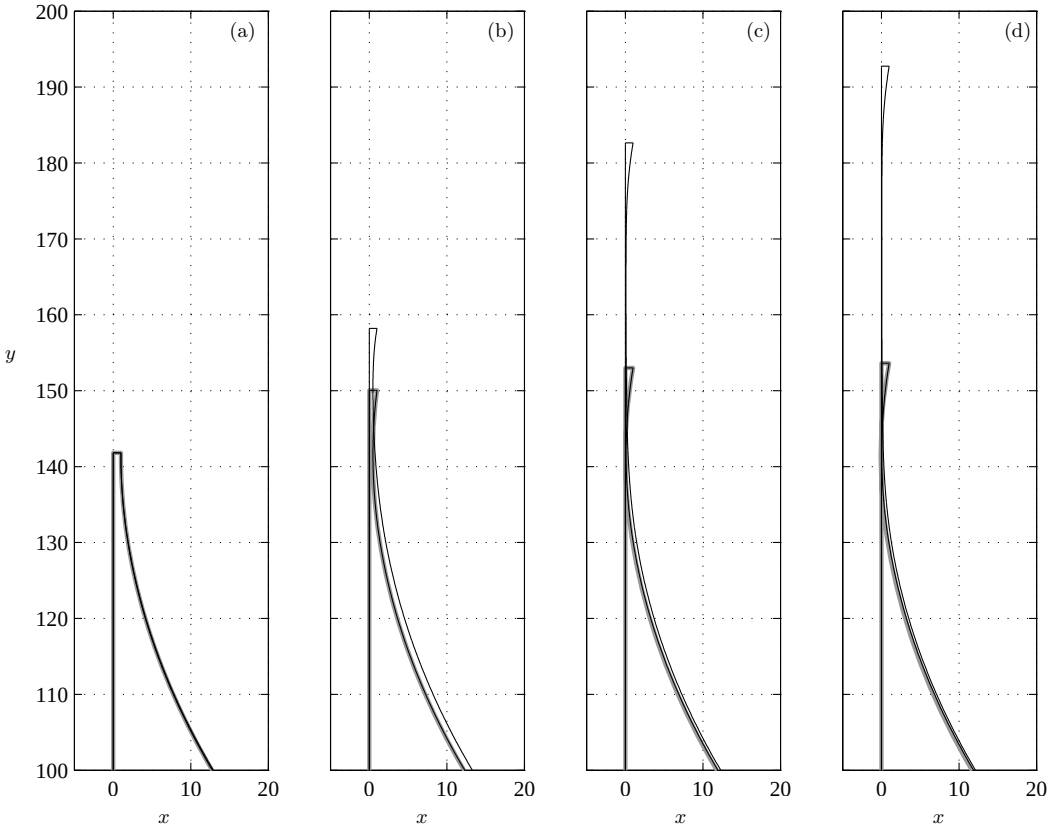

Figure 3.4.: Numerical simulation of film shapes $\big(X(S)/W, Y(S)/W\big)$ for $\ell_c = 100\,W$ (ie. $\epsilon = 0.01$) comparing large and small capillary numbers to the film shape predicted by the quasi static theory. Numerical solutions with $\alpha = 10^{-4} \ll \epsilon$ (medium black lines) fall on top of the corresponding quasi-static film shapes (thick gray lines). Numerical solutions with $\alpha = 1 \gg \epsilon$ (thin black lines) extend much higher for the same minimal film thickness. The four panels show the two shapes when they have the same minimal thickness: (a) $X^* = 1\,W$, (b) $X^* = 0.5\,W$, (c) $X^* = 0.1\,W$ and (d) $X^* = 0.05\,W$.

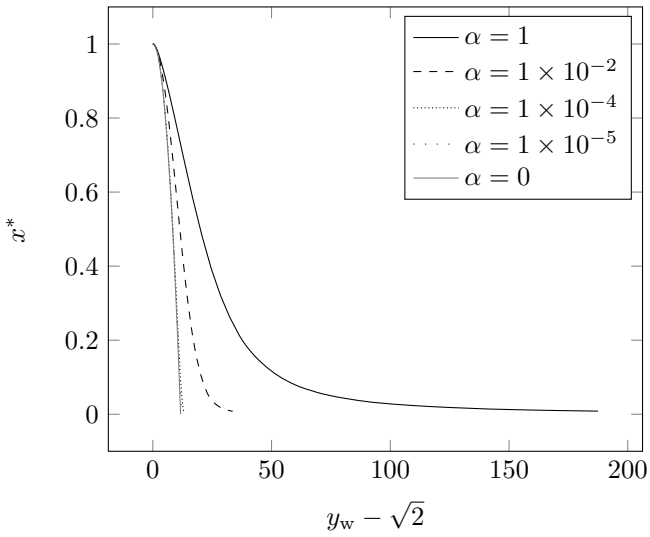

Figure 3.5.: The x-coordinate x^* of the thinnest point on the dynamic film surface with $\epsilon = 0.01$ as a function of the lift height $(y_w - \sqrt{2})$ of the wire for five values of the capillary number: $\alpha = 0$ (the static case), $1, 10^{-2}, 10^{-4}$ and 10^{-5}.

to $y_w(0) = \sqrt{2}$ and $h(y) = h_0(y)$, respectively. Each simulation was stopped when the minimum film thickness reached 1% of w, i.e., $x^* = 0.01$.

3.5.1. Film shapes

First, in Fig. 3.4, we show an example of the effect on the film shape of going from a low capillary number in the quasi-static limit, $\alpha \ll \epsilon$, to a high capillary number in the dynamic limit, $\alpha \gg \epsilon$. An immediate result is that by increasing the capillary number (the pulling speed) the film can be stretched out much further before breaking. In the example with $\epsilon = 0.01$ the stretching ratio $[y_{wb}(1.0) - \sqrt{2}]/[y_{wb}(0.0001) - \sqrt{2}]$ is nearly 5. Here, $y_{wb}(\alpha)$ is the breakup lift height for a film being pulled at the capillary number α, while $y_{wb}(0.03) = 196\epsilon$ and $y_{wb}(0.001) = 153\epsilon$.

3.5.2. Thinning of the film

A further observation in Fig. 3.4 is that for large capillary numbers a long, thin region develops for $\sqrt{2} < y < y_w$ before the film breaks. As a consequence the draining of the film slows down as the film is thinned down towards breaking. This effect is studied further in Figs. 3.5 and 3.6.

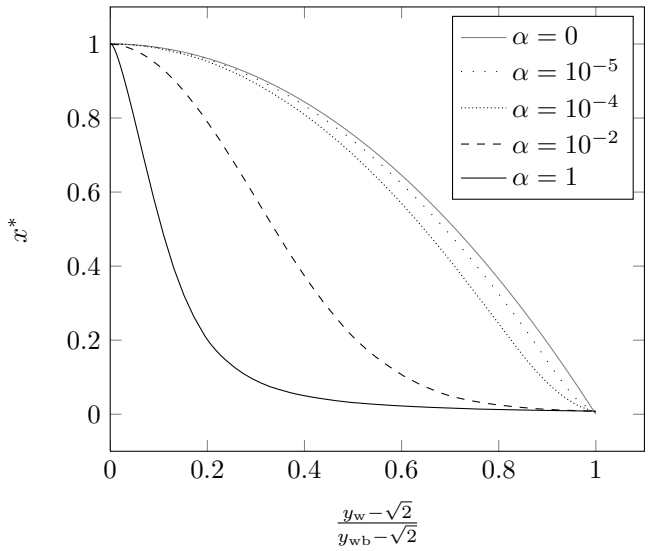

Figure 3.6.: The same data as in Fig. 3.5 but now rescaling the lift height $(y_w - \sqrt{2})$ by the breakup lift height $(y_{wb} - \sqrt{2})$.

In Fig. 3.5 the film half-width x^* is plotted versus the wire lift height y_w for five values of the capillary number α between zero and unity. For $\alpha \ll \epsilon$ the graph for $x^*(y_w)$ approach $x^* = 0$ rapidly, while for $\alpha \gtrsim \epsilon$ a clear slow-down in the breaking process is seen. For low capillary numbers the film thinning as a function of lift height follows the prediction made by the quasi-static model presented in section 3.3 (full lines), while deviations from this is seen at high capillary numbers (dotted lines).

The slow down of the thinning process for high capillary numbers is made more clear in Fig. 3.6, where the lift height $y_w - \sqrt{2}$ has been rescaled by the final lift height $y_{wb} - \sqrt{2}$ at the breaking point. Here it is clearly seen how the film thickness $x^*(y_w)$ undergoes a transition from a purely convex form at $\alpha \ll \epsilon$ to a mainly concave form with a long tail for $\alpha \gg \epsilon$.

3.5.3. The breakup height y^*

In the quasi-static case, $\alpha \ll \epsilon$, the breakup height y^* of the film was found to be constant, namely $\sqrt{2}$, see Eq. (3.15). In the dynamic case it depends on the capillary number, i.e. $y^* = y^*(\alpha)$. Accordingly, there exist a critical capillary number α_c dividing the quasi-static and the dynamic cases.

In Figure 3.7 this is illustrated for a wire of half-width $\epsilon = 0.01$ by plotting y^* versus the (rescaled) lift height y_w for five different capillary numbers in the range

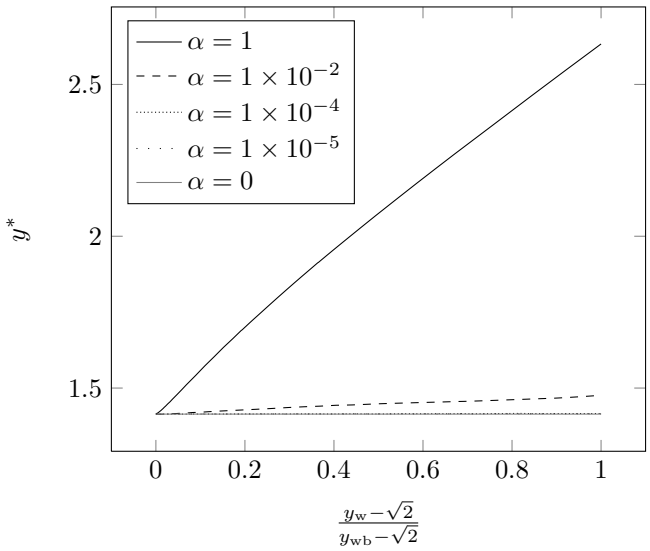

Figure 3.7.: The numerically calculated height y^* in units of ℓ_c of the thinnest point of the film as a function of the lift height $(y_w - \sqrt{2})$ rescaled by the breakup lift height $(y_{wb} - \sqrt{2})$.

from zero to unity. For $\alpha \ll \epsilon$ we see that y^* remains close to $\sqrt{2}$. For $\alpha = \epsilon$ a relative deviation of up to 5% is noted, and for $\alpha \gg \epsilon$ a nearly linear increase of y^* from $\sqrt{2}$ to 2.7 can be seen.

In Eq. (3.31) we argued that $\alpha_c \approx \epsilon$, and this statement we test by direct numerical simulation in the following by calculating the film breakup height $y^*(\epsilon, \alpha)$ as a function of capillary number for six different values of the wire half-thickness ϵ in the range from 0.001 to 0.1. The numerical result for the film breakup height $y^*(\epsilon, \alpha)$ is shown in Figure 3.8. The value is calculated when the minimum film thickness is $x^* = 0.01$ and should therefore give a good indication of the breakup height as a function of capillary number. For capillary numbers lower than approximately 10^{-3} the breakup height is almost constant at $y^* = \sqrt{2}$ as expected from Eq. (3.15). For capillary numbers higher than approximately 10^{-3} the breakup height starts to deviate from the quasi-static prediction.

To obtain a more quantitative measure we define the critical capillary number $\alpha_c(\epsilon)$ for a given value of wire half-width ϵ by the abscissa of the intersection between the quasi-static (horizontal) line $y^* = \sqrt{2}$ and a linear fit to the numerical data $y^*(\epsilon, \alpha)$ for large values of the capillary number, $\alpha > 10^{-2}$. The result is summarized in the legend of figure 3.7, where it is confirmed that with a fair

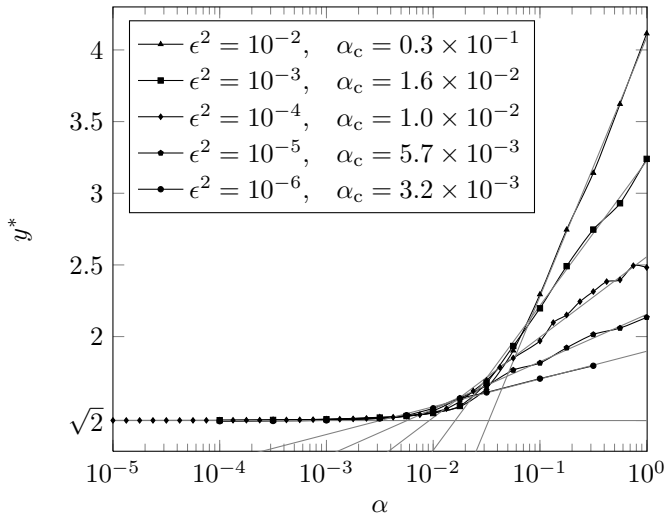

Figure 3.8.: The numerically calculated height y^* in units of ℓ_c of the thinnest point of the film as a function of capillary number α for five values of the wire half-width ϵ. The full black lines are just connecting consecutive data points, while the gray lines are best fits $y^*_{\text{fit}}(\alpha)$ of the numerical data for $\alpha > 10^{-2}$. The critical capillary number α_c, calculated by $y^*_{\text{fit}}(\alpha_c) = \sqrt{2}$, defines where the cross-over from quasi-static flow to full dynamical flow in the film takes place.

agreement

$$\alpha_c(\epsilon) \approx \epsilon. \tag{3.54}$$

3.5.4. Extensional flow

The quasi-static analysis, Eq. (3.33), confirmed the assumption by van Nierop, Scheid and Stone [56] that the flow in film withdrawal is extensional. For a wire half-width $\epsilon = 0.01$, the numerical simulation of the velocity field shown in Fig. 3.9, reveals that even for the relatively large capillary number $\alpha = 0.075$ the flow is seen to be extensional.

3.6. Future extensions and applications for the code

We have established a flexible code base that can be used to model drawing of thin liquid films over a broad parameter space. To demonstrate the flexibility and to suggest future improvements and paths to explore we will briefly show how

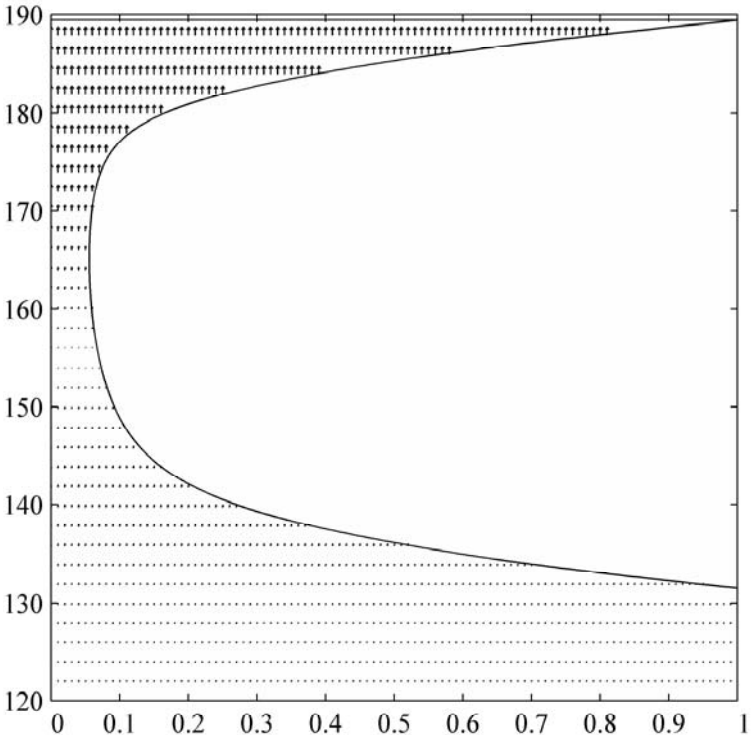

Figure 3.9.: Plot of the velocity vectors in the film region of a simulation with $\epsilon = 0.01$ and $\alpha = 0.075$. The flow is seen to be extensional as suggested by the quasi-static analysis.

to include the effect of Marangoni stresses caused by the influence of an external temperature gradient on surface tension. This model setup closely resembles the planned experiments of Ernst van Nierop, School of Engineering and Applied Sciences (SEAS), Harvard University.

3.6.1. Effects of Marangoni stress at the free surface

One motivation for doing experiments on film drawing and implementing a numerical scheme capable of handling both a constant surface tension as well as a varying surface tension introducing Marangoni stresses at the free liquid interface is the possibility for using an external field (e.g. a temperature gradient) to control the thickness of the film. Experimental results on drawing free liquid films in a thermal gradient have not yet been obtained. However, we wish to demonstrate the flexibility of our numerical implementation by describing how an external temperature gradient influencing the surface tension can be implemented in our

numerical code. Our simple test case will be a liquid film drawn from a bath of liquid in a vertical temperature gradient going from hot at the liquid bath to cold above the bath. The thermocapillary effect has been used to control fluid motion by driving thin fluid films towards regions with lower temperatures and hence higher surface tension [12, 24]. We imagine using the same principle to influence the drainage of liquid films during creation and thereby control their thickness.

In the following we consider a film being drawn in a temperature field $T = T(y)$ with a constant temperature gradient $\partial_y T$ less than 0. If the surface tension $\gamma(T(y))$ is inversely proportional to T we can simply implement the varying surface tension in Comsol by replacing the constant γ in equation (3.53) with a function $\gamma(y)$. For testing we will use a constant gradient and have a cutoff at a maximum value $\gamma_{\max}$. We will introduce the following y-dependance of γ

$$\gamma(y) = \min\left(\gamma_{\max}, \gamma_0\left[1 + \frac{\epsilon}{2}\frac{\gamma_{\max}}{\gamma_0}y\right]\right) \tag{3.55}$$

which makes γ change linearly from γ_0 at $y = 0$ to $\gamma_{\max}$ at twice the capillary length above the surface of the bath at infinity. This is simply introduced in Comsol by introducing an expression in the `struct` field `fem.expr`, see also appendix A.2. We do not account for changes in other fluid parameters such as viscosity or density that might also change with temperature. Implementation of such variations can however be achieved in a similar way.

Running the code for four different maximum values of the surface tension yields film thickness vs. time curves as shown in figure 3.10. The main thing to note is that the Marangoni stress induced by the external field

By inspecting the film profiles of a film drawn with constant surface tension and a film drawn in a surface tension gradient the difference in film drainage is quite noticeable, see figure 3.11.

We hope that this flexibility of the code and the ease at which external influences on surface tension can be implemented will prove useful when the experimental setup is established.

3.6.2. Convection and diffusion at the free interface

An often utilized way to stabilize liquid films is by adding surfactants. When a thin film is generated the flow in the liquid film will affect the concentration of surfactants at the surface and thereby the surface tension at the liquid-gas interface.

The equation governing surfactant transport along a two-dimensional deforming surface is given in terms of the dimensionless surfactant concentration c as [48, 52]

$$\partial_t c + \boldsymbol{\nabla}_s \cdot (c\boldsymbol{u}) = \frac{1}{Pe}\nabla_s^2 c, \tag{3.56}$$

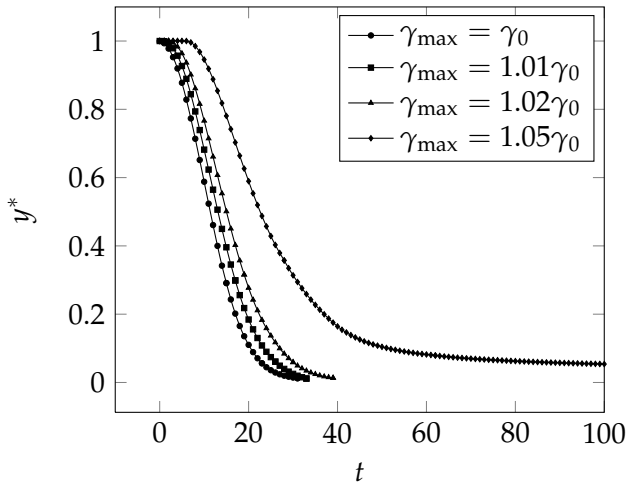

Figure 3.10.: Minimum film thickness y^* vs. time t for runs of the numerical code with four different surface tension gradients. The Marangoni stress drives fluid into the film region which causes the film to drain more slowly.

Typical dimensions would be:

$w = 10\,\mu\text{m}$

$v_0 = 1\,\text{cm/s}$

$D = 1 \times 10^{-9}\,\text{m}^2/\text{s}$,

which would give a typical Péclet number of 100.

where $\boldsymbol{u}$ is the fluid velocity, $Pe = \frac{wv_0}{D}$ is the Péclet number and $\boldsymbol{\nabla}_s = (\mathbf{I} - \boldsymbol{nn}) \cdot \boldsymbol{\nabla}$ is the the surface gradient operator. The surfactants are assumed to be insoluble and are therefore only to be found at the surface of the liquid and not in the bulk.

We wish to solve Eq. (3.56) on the free boundary of a liquid thin film. Typical end-point conditions could be a constant concentration, i.e., a Dirichlet-type point constraint, or a no-flux condition ensuring that the surfactant molecules stays at the free surface. In this section we assume that the surfactant molecules cannot leave the surface and we therefore have a no-flux condition at the endpoints of the free surface

$$\boldsymbol{n} \cdot \left(-\frac{1}{Pe} \boldsymbol{\nabla}_s c + c\boldsymbol{u} \right) = 0. \tag{3.57}$$

This type of condition should be applied near the wire or if the bath have a finite size and the free surface is bounded by a solid wall.

To solve Eq. (3.56) using the finite element method, we state the equation on weak form by multiplying with a test function $\tilde{c}$ and integrating over the free boundary as discussed in section 2

$$\int_{\partial\Omega(t)} \tilde{c}\, \partial_t c \, \mathrm{d}s = \int_{\partial\Omega(t)} \boldsymbol{\nabla}_s \tilde{c} \cdot \left(c\boldsymbol{u} - \frac{1}{Pe} \boldsymbol{\nabla}_s c \right) \mathrm{d}s + \sum_P \tilde{c}\boldsymbol{n} \cdot \left(\frac{1}{Pe} \boldsymbol{\nabla}_s c - c\boldsymbol{u} \right). \tag{3.58}$$

Here $\partial\Omega(t)$ means integration over the boundaries where the convection-diffusion equation are active and the sum over P are the contributions at the endpoints of

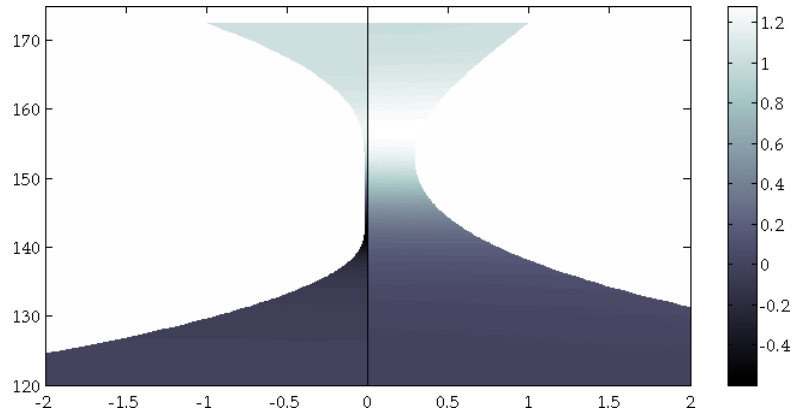

Figure 3.11.: Zoom-in on a gray scale plot of the vertical velocity component in two half-films drawn with a capillary number $\alpha = 10^{-2}$ and $\epsilon = 10^{-2}$. (left) Constant surface tension $\gamma(y) = \gamma_0$ and (right) linear surface tension gradient using equation (3.55) with $\gamma_{\max} = 1.05\gamma_0$. The film with constant surface tension drains very quickly while the film stabilized by a Marangoni stress maintains a much wider film region.

the boundaries. The boundary conditions in enforced by substituting (3.57) in the sum over the endpoints

$$\int_{\partial\Omega(t)} \tilde{c}\, \partial_t c \, \mathrm{d}s = \int_{\partial\Omega(t)} \nabla_s \tilde{c} \cdot \left(c\boldsymbol{u} - \frac{1}{Pe} \nabla_s c \right) \mathrm{d}s. \tag{3.59}$$

The x and y-components of the surface gradient operator ∇_s working on the concentration field are available in Comsol as `cTx` and `cTy`, respectively. The corresponding components of the surface gradient operator working on the concentration test functions are given by `test(cTx)` and `test(cTy)`.

To study the implementation of Eq. (3.59) in Comsol we use the model system sketched in Fig. 3.12. The Comsol code is listed in Appendix A.3.

The result of a simulation is seen in Fig. 3.13. As time progresses, the concentration goes to zero at the left boundary and rises at the right boundary. Diffusion keeps the concentration profile smooth and smeared out even at higher times. The magnitude of the diffusion must be sufficient to keep the concentration profile smooth over a couple of mesh elements. Otherwise instabilities develop with huge numerical oscillations in the solution. This can be circumvented ether by refining the mesh or by using artificial stabilization techniques such as streamline diffusion [37].

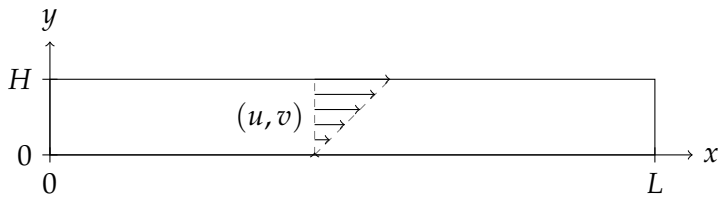

Figure 3.12.: Model system used for testing the implementation of a convection-diffusion equation at a boundary. We choose the height to be $H = 1$, the length $L = 10$. The velocity field is a shear flow $\boldsymbol{u} = (v_0 y/H, 0)$ and the initial concentration of surfactants is $c_0 = 1$ at the top boundary.

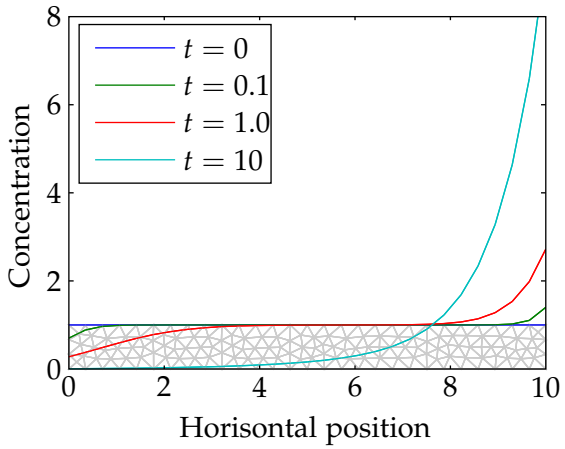

Figure 3.13.: The concentration profile along the upper boundary of the geometry at four different times. The parameters used in the simulation is $Pe = 1$ and $v_0 = 1$. The mesh is shown in gray at the bottom of the figure.

The concentration c of surfactant molecules should be coupled to the surface tension by a constitutive equation [5, 47]. We suggest the implementation of a convection–diffusion equation for the concentration of insoluble surfactants at the free interface as a natural next step in developing the code for future studies.

3.7. Conclusion

We have studied the breakup of liquid films at zero Reynolds number drawn from a bath of pure Newtonian liquid as a function of wire half-width ϵ and capillary number α. We have established that the quasi-static limit is given by $\alpha \ll \epsilon$, and in

that limit we have derived an analytical expression for the shape $\big(h(y), y\big)$ of the free surface of the liquid film.

To be able to study the problem beyond the quasi-static limit, we have developed an efficient numerical implementation in Comsol for simulating the film drawing process including surface tension and deforming boundaries.

The results of the numerical simulations and the analytical predictions agree in the quasi-static limit. For higher capillary numbers we have characterized the changes in the dynamics of the film. In particular for high capillary numbers we have identified a slow-down of the film thinning process as the breakup is approached.

Finally, analytical results in the quasi-static limit and numerical results for capillary numbers up to unity have confirmed that the flow in the film region is more extensional than sheer as argued recently by van Nierop, Scheid and Stone [56].

Within the time frame of the PhD study we have not been able to use the developed code to verify experimental data. However, we now have a flexible and easily extendable code that can be used in future studies of free surface flows.

4. Deterministic lateral displacement devices

Originally, it was the intend to extend the studies of finite sized particles in deterministic lateral displacement (DLD) devices done during the authors MSc studies during the thesis work [15]. The idea was to use level set methods and ALE to study the dynamics of non-spherical particles as they pass through arrays of obstacles. The main motivation for such studies were to develop means of morphological separation, i.e., to be able to separate particles of comparable hydrodynamic size but with different morphologies. The numerical studies should be performed alongside experimental investigations at Lund University. Unfortunately, the clean room facilities broke down and these studies were not pursued. Instead of studying the behavior of individual particles we choose to do more general statistical or concentration-based models and simulations of the deterministic lateral separation principle. This allowed us to investigate the limits of deterministic lateral displacement, in particular the influence of diffusion on the critical particle size for a given device.

This chapter contains the results of the analysis of DLD devices carried out during the work on this thesis. Some of the results have been presented in the paper *A theoretical analysis of the resolution due to diffusion and size dispersion of particles in deterministic lateral displacement devices* by Heller and Bruus [14] and are included here with some rewording and additional comments. Other parts of this chapter are based on the section "Basic theoretical analysis" from the paper *Multi-directional sorting modes in deterministic lateral displacement devices* which was written in collaboration with Brian R. Long, Jason P. Beech, Heiner Linke, Henrik Bruus, and Jonas O. Tegenfeldt [31]. In addition to the results from the two papers this chapter presents new results from finite-element simulations of the flow and particle distribution in DLD devices.

In the following sections we will introduce DLD devices by presenting a discrete model of the separation process in traditional $1/N$-devices [20]. This model is used to analyze the influence of diffusion and particle-size dispersion on the separation process. Next we present an analysis of separation in a general M/N-device and show that these devices add two novel separation directions in addition to the two

separation directions known from the $1/N$-arrays.

4.1. Background: Separation on the micro-scale using DLD devices

In 2004 Huang et al. [20] developed the elegant method of particle separation by deterministic lateral displacement in so-called microfluidic bumper arrays. The method, which relies on the laminar flow properties characteristic of microfluidics, shows a great potential for fast and accurate separation of particles on the micrometer scale [3, 9, 20, 21, 57] as well as the ability to steer and focus streams of suspended particles [35]. Among the key assets of the deterministic lateral displacement separation principle are that clogging can be avoided because particles much smaller than the feature size of the devices can be separated, that the devices are passive, i.e. the particles bump into solid obstacles or bumpers, and that the separation process is continuous.

Particle transport in microfluidic DLD arrays is primarily governed by convection due to the fluid flow and by displacement due to interaction with the bumpers in the array [20]. These processes are deterministic and the critical diameter for separation of relatively large particles in these devices is well understood in terms of the width of flow lanes bifurcating around the bumpers in the periodic arrays [21]. However, if DLD arrays and particles are scaled down, diffusion will influence the separation process and affect the critical particle size significantly. Previously reported data on separation of particles in DLD arrays all show a bias towards larger critical particle size than that given by the width of the flow lanes nearest to the bumpers of the array [20, 21, 57]. In this chapter we extend the simple models by adding diffusion and taking particle-diameter dispersion into account, and thereby explain some of the observed discrepancy.

In DLD arrays particles are convected by the fluid flow through an array of bumpers placed in columns separated by the distance λ in the flow direction, see Figure 4.1(a). For a given integer N, the array is made N-periodic in the flow direction by displacing the bumpers in a given column a distance λ/N perpendicular to the flow direction with respect to the bumper positions in the previous column. Due to this periodicity of the array and the laminarity of the flow, the stream can naturally be divided into N lanes, each carrying the same amount of fluid flux, and each having a specific path through the device, see Ref. [20].

For a given steady pressure drop, the fluid in the device moves with an average velocity u_0. Assuming a parabolic velocity profile $u(x)$ in the gap of width w_g

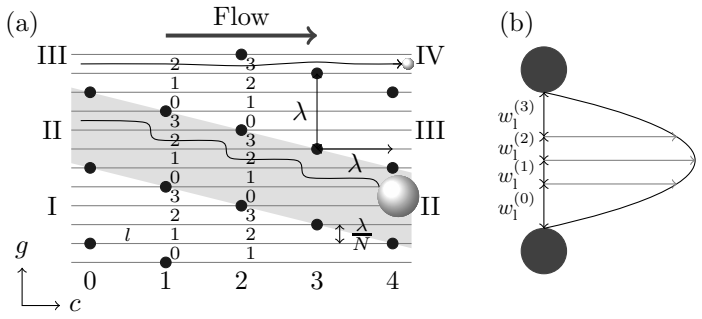

Figure 4.1.: (a) An array of bumpers (black dots) with the definition of the lane number l (small arabic numbers), the column number c (large arabic numbers), and the gap number g (roman numbers). The shaded region illustrates how the shift in the position of gap II follows the geometry of the array. Large particles following the displacement path will therefore stay in the same gap number and lane number throughout the entire array as illustrated by the skew bumping trajectory of a large particle (large illuminated sphere). Small particles will not be displaced by the bumpers and will therefore visit all lane numbers as they follow the so-called zigzag path through an entire period of the array [20]. This is illustrated by the almost horizontal trajectory of a small particle in the upper flow lane (small illuminated sphere). (b) Close-up of a single gap between two bumpers (disks) in the array. Each of the four flow lanes carries the same flow rate. Due to the parabolic flow profile in the gap region, the width $w_l^{(l)}$ of flow-lane l depends on its position in the gap.

between two neighboring bumpers, see Figure 4.1(b),

$$u(x) = 6u_0 \frac{x}{w_g}\left(1 - \frac{x}{w_g}\right), \tag{4.1}$$

the total flow rate Q_{tot} in the gap between two obstacles is given by

$$Q_{tot} = \int_0^{w_g} u(x)\,\mathrm{d}x = w_g u_0. \tag{4.2}$$

By numerical simulations at low Reynolds numbers relevant for the actual devices, $Re \approx 10^{-3} - 10^{-2}$, we find the assumption of a parabolic flow profile in the gap region well justified. This also agrees with the usual estimate for the entrance length $l_{entr} = 0.06 Re\, w$, which here is of the order 1 nm.

For an N-periodic array, the N flow lanes in a given gap carry the same flow rate Q_{tot}/N. The width $w_{\text{l}}^{(l)}$ of lane l is found by solving

$$\frac{Q_{\text{tot}}}{N} = \int_{x^{(l)}}^{x^{(l)}+w_{\text{l}}^{(l)}} u(x)\,\mathrm{d}x, \tag{4.3}$$

where $x^{(l)} = \sum_{j=0}^{l} w_{\text{l}}^{(j)}$ is the starting position of lane l. In the simple bifurcating flow-lane model [20, 21] the critical diameter d_{c} is given as $d_{\text{c}}/2 = w_{\text{l}}^{(1)}$. A small particle with $d < d_{\text{c}}$ will never leave its initial flow lane and will thus be convected in the general flow direction following a so-called zigzag path. The conventionally used name zigzag path refers to the case where the bumpers are large compared to their center-to-center distance. In this case the path, which appears almost straight in Figure 4.1 given the smallness of the bumpers, becomes truly zigzag-shaped [20]. Large particles with $d > d_{\text{c}}$ will quickly bump against a bumper and from then on be forced by consecutive bumping to follow the skew direction of the array geometry, the so-called displacement path. When a particle gets bumped by a bumper in the array it will be displaced perpendicular to the flow direction until its center is located one particle radius $d/2$ from the surface of the bumper. This corresponds to n_{l} lanes of displacement,

$$n_{\text{l}} = \frac{N}{w_{\text{g}} u_0} \int_0^{d/2} u(x)\,\mathrm{d}x = N \frac{d^2}{4w_{\text{g}}^2}\left(3 - \frac{d}{w}\right). \tag{4.4}$$

In the bulk fluid, where the lanes are assumed to have equal width λ/N, see Figure 4.1(a), the displaced distance ℓ_{disp} is therefore

$$\ell_{\text{disp}}(d) = n_{\text{l}} \frac{\lambda}{N} = \lambda \frac{d^2}{4w_{\text{g}}^2}\left(3 - \frac{d}{w_{\text{g}}}\right). \tag{4.5}$$

In the following sections we extend the simple bifurcating flow-lane model by including diffusion and particle-diameter dispersion.

4.2. Model including diffusion

During the average time $\tau = \lambda/u_0$ it takes a particle to move by convection from one column to the next, the particle also diffuses. We assume that the diffusion process perpendicular to the flow direction is normally distributed with mean value zero and variance

$$\sigma^2 = 2D\tau, \tag{4.6}$$

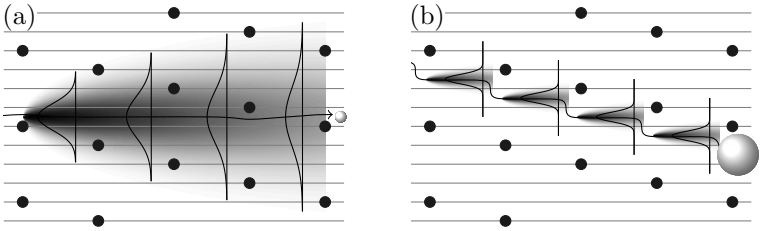

Figure 4.2.: (a) The motion of very small particles is dominated by diffusion. Their distribution at the end of the array is therefore determined by their transverse diffusion during the time spend in the array. The intensity of the shaded region indicates the probability of finding the small particle at a given position in the array. A non-diffusive particle would follow the solid black trajectory straight through the array. (b) A large particle diffuse as well—but not very much—and every time the large particle interacts with a bumper its position in the gap is reset to the particle radius. Large particles therefore only have a slight probability of escaping the displacement path represented by the full black line. In both panels the Gaussian distribution of the diffusing particles is shown at four cross-sections.

where the diffusivity D is given by the Stokes–Einstein expression

$$D = \frac{k_B T}{3\pi\eta d}. \tag{4.7}$$

Here k_B is Boltzmann's constant, T is the temperature and η is the viscosity of the fluid. Throughout this thesis we use this expression to calculate D for any given particle size.

Figure 4.2 shows the two limits of (a) a small strongly diffusing particle, for which the interaction with the bumpers as well as the role of the flow lanes are negligible, and (b) a large particle, for which diffusion rarely brings the particle out of its given lane, and where each bumping event resets the position of the particle.

Note that we do not model Taylor-Aris dispersion explicitly. This convection-diffusion phenomenon mainly affects the particle distribution along the flow direction [6]. However, we are not interested in the detailed arrival times of the particles in the outlet, only in their transverse distribution.

4.2.1. Diffusion model

In order to escape bumping, a particle must in the time interval τ diffuse more than the difference $\ell_{\text{disp}} - \lambda/N$ between the bulk displacement and the shift in

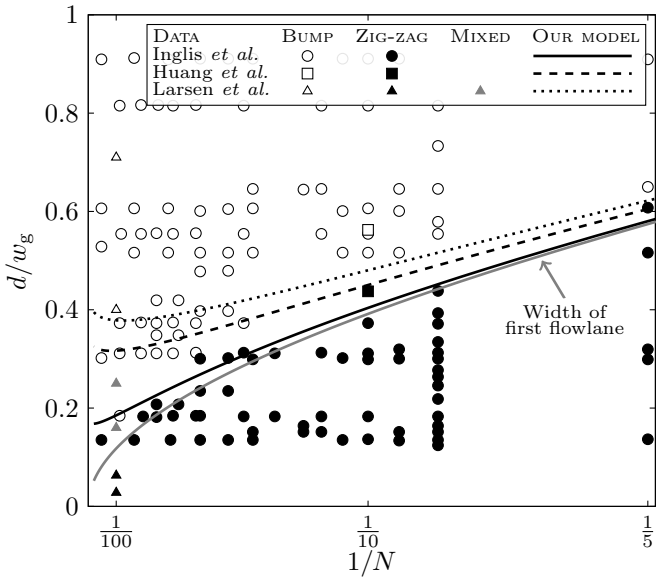

Figure 4.3.: Our model applied to the experimental data of Inglis et al. [21], Huang et al. [20] and Larsen [27]. Particle diameter d over gap width w_g is plotted as a function of the inverse period $1/N$. The full, dashed and dotted black lines show the theoretically predicted critical particle size for the bumper arrays used by Inglis et al. [21] (only points with $\varepsilon = 1/N$), Huang et al. [20] (only for $N = 10$) and Larsen [27] (only for $N = 100$), respectively. The experimental data points are representing particles following bumper paths (open symbols), zigzag paths (solid black symbols), and neither of these paths (solid gray symbols).

position of the next bumper. The probability p_{esc} that this will happen is given by the integral of the Gaussian tails (see figure 4.2) in the neighboring lanes, i.e., by the error function

$$p_{\text{esc}}(d) = \frac{1}{2} - \frac{1}{2}\,\text{erf}\left(\frac{\ell_{\text{disp}}(d) - \frac{1}{N}\,\lambda}{\sqrt{2}\,\sigma(d)}\right), \tag{4.8}$$

where we have introduced the d-dependence explicitly. When a particle is transported through a bumper array it must bump at every bumper within one period of the array in order to be displaced one gap at the outlet. Thus, if the particle escapes at least one time in N attempts, it will not be displaced. We define the critical particle size d_c as the size for which half of the particles escape bumping as

they pass one period of the array. Thus d_c can be found by solving

$$\sum_{k=1}^{N} \binom{N}{k} p_{esc}(d_c)^k \Big[1 - p_{esc}(d_c)\Big]^{N-k} = \frac{1}{2}. \tag{4.9}$$

In Figure 4.3 we have plotted the result of our model calculation for the critical particle sizes as a function of the bumper period for parameter values corresponding to the DLD arrays used by Inglis et al. [21] (full line), Huang et al. [20] (dashed line), and Larsen [27] (dotted line). The corresponding measured data points from these papers are plotted as circular, square, and triangular points, respectively.

It must be emphasized that although the authors of Ref. [21] in their text only describe DLD arrays with a relative column displacement $\varepsilon = 1/N$, they do plot, without comments, data points with other displacements, e.g. $\epsilon = 0.3$. These non-$1/N$ DLD arrays lead to more complicated displacement characteristics which we will look into in section 4.3. In this section we focus on the influence of diffusion and particle-size distribution on the more simple and most widely used $1/N$ DLD arrays. In Figure 4.3 we have therefore only plotted data points from Ref. [21] with $\epsilon = 1/N$.

4.2.2. Comparison to experiments

The observation that the critical particle size in a $1/N$ bumper device is larger than the width of the first flow lane is also supported by the experimental data in figure 2 of Ref. [21]. Our model suggests that the deviation of the critical particle size from the width of the first flow lane can be explained by diffusion of the particles. In Figure 4.3 it is seen how well the theoretical lines are predicting the transition between zigzag paths and displacement paths: the full line is dividing open and closed circles, the dashed line is dividing open and closed squares, and the dotted line is dividing open and closed triangles.

Using parameter values corresponding to the bumper device presented by Huang et al. [20] our model predicts a critical particle diameter of 0.45 times the width of the gap for the particles traveling through the device with an average velocity of 400 µm/s. This is in good agreement with figure 2(a) in Ref. [20].

4.2.3. A discrete model including diffusion and dispersion

Particles typically used in experiments on particle separation are not mono-disperse. Their average diameters are distributed around a certain mean value with a relative standard deviation $\Delta d/d$, which typically is 20 %, 10 % and 5 % for particles with $d = 25\,\text{nm}$, $d = 100\,\text{nm}$ and $d = 500\,\text{nm}$, respectively.

Faced with such a size dispersion it is very useful to have a simple method to predict its effect. In the following we therefore introduce a discrete model of the transport of particles with different diameters d in an N-periodic bumper array taking convection, diffusion and size-dispersion into account. The model allows us to study the relative influence of all three phenomena on the separation efficiency in a fast and simple manner. We illustrate our model by using the specific parameters from the bumper device presented in Ref. [27], see figure 4.4. In particular our results suggest that the critical size for separation or displacement, studied above, must be supplemented by a smaller critical size, below which pure diffusion governs the motion of the particles in the bumper array. This prediction has not yet been tested experimentally.

4.2.4. Definition of the discrete model

At any instant, a particle is assumed to be positioned in the center of a flow lane l of gap g in some column c of the array. For simplicity we further assume that the size distribution of any given set of particles is a normal distribution with a mean value given by the size quoted by the manufacturer and a relative standard deviation of 10 %.

By convection any given particle moves from one column to the next. If it ends up in the last lane ($l = N - 1$) in one gap, it will be shifted to the first lane ($l = 0$) in the subsequent gap. Otherwise it will stay in the current gap and move up one lane. In our model pure convection is therefore described by the discrete map

$$(c, g, l) \mapsto \begin{cases} (c+1, g+1, 0), & \text{if } l = N-1, \\ (c+1, g, l+1), & \text{otherwise.} \end{cases} \tag{4.10}$$

Because of the finite diameter d of the particle there is a minimum and a maximum lane number that it can occupy. The minimum lane number is the smallest integer $l_{\min}$ that satisfies

$$\sum_{l=0}^{l_{\min}} w_1^{(l)} > \frac{d}{2}. \tag{4.11a}$$

Similarly, the maximum lane number $l_{\max}$ is the largest integer that satisfies

$$\sum_{l=l_{\max}}^{N-1} w_1^{(l)} > \frac{d}{2}. \tag{4.11b}$$

Consequently, the simple convection mapping from (4.10) needs to be modified to

account for the finite size of the particles

$$(c, g, l) \mapsto \begin{cases} (c+1, g+1, l_{\min}), & \text{if } l = N-1, \\ (c+1, g, l+1), & \text{if } l < l_{\max} - 1, \\ (c+1, g, l_{\max}), & \text{otherwise.} \end{cases} \tag{4.12}$$

The above convection scheme accounts for the separation of particles in deterministic lateral displacement devices according to size. The critical particle diameter predicted by this model is

$$d_{\mathrm{c}} = 2w_1^{(0)} \tag{4.13}$$

in accordance with the geometric arguments of Ref. [21].

To characterize the separation quantitatively, we define the relative particle numbers r_0, r_1 and r_{d} as

$$r_0 = \text{relative number of particles following the zigzag path.} \tag{4.14a}$$

$$r_1 = \text{relative number of particles following the displacement path.} \tag{4.14b}$$

$$r_{\mathrm{d}} = \text{relative number of all other particles.} \tag{4.14c}$$

With these definitions the sum $r_0 + r_1 + r_{\mathrm{d}}$ is always unity. If $r_0 = 1$ all particles follow the zigzag path and if $r_1 = 1$ all particles follow the displacement path. If $r_{\mathrm{d}} \neq 0$ some of the particles end up at positions not explained by the deterministic analysis of the separation process. In Figure 4.4 we have plotted the relative particle numbers r_0, r_1, and r_{d} as a function of average particle diameter d.

4.2.5. Pure mono-disperse convection

For mono-disperse and non-diffusing particles, the model results, as expected, in two modes: the zigzag mode and the displacement mode, see the closed circles in Figure 4.4. For $d < d_{\mathrm{c}}$ we have $r_0 = 1$, and for $d \geq d_{\mathrm{c}}$ we have $r_1 = 1$, while we always have $r_{\mathrm{d}} = 0$. The relative particle numbers can therefore be written as

$$r_0 = \int_{-\infty}^{d_{\mathrm{c}}} \frac{1}{\sqrt{2\pi(\Delta d)^2}} \exp\left(\frac{-(s-d)^2}{2(\Delta d)^2}\right) \mathrm{d}s. \tag{4.15a}$$

Similarly, the relative number of particles following the displacement path r_1 can be found by integrating over all particle sizes larger than d_{c}

$$r_1 = \int_{d_{\mathrm{c}}}^{\infty} \frac{1}{\sqrt{2\pi(\Delta d)^2}} \exp\left(\frac{-(s-d)^2}{2(\Delta d)^2}\right) \mathrm{d}s. \tag{4.15b}$$

The system is still a bi-modal system because $r_{\mathrm{d}} = 0$ for all particle sizes.

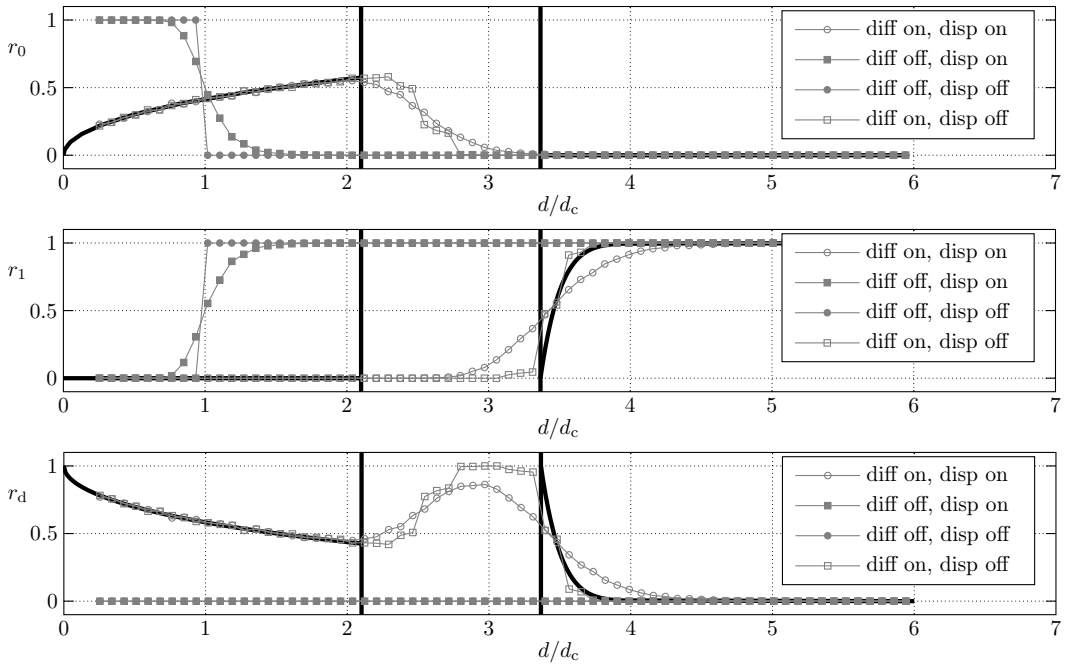

Figure 4.4.: Relative number r_0, r_1 and r_d of particles following the zigzag path, the displacement path, and neither of these two paths, respectively, plotted as a function of the normalized, average particle diameter d/d_c, where $d_c = 118\,\text{nm}$. The parameters of the bumper array is taken from Ref. [27]: $N = 100$, $\lambda = 8\,\mu\text{m}$, $w_g = 1\,\mu\text{m}$, $L = 20N\lambda = 16\,\text{mm}$, and $u_0 = 250\,\mu\text{m/s}$. The buffer liquid is water at room temperature. Neglecting diffusion (solid symbols), the particles follow the zigzag path if $d < d_c$ and the displacement path if $d > d_c$. Including diffusion (open symbols), with D given by equation (4.7), the small particles are not influenced by the bumpers. For $d > 2.1\,d_c$ the influence of the bumpers sets in, and for $d > 3.4\,d_c$ the particles follow the displacement path. The full black curves are the predictions using the results in Secs. 4.2.6.1 and 4.2.6.2, while the thick black vertical lines indicate the particle size when small particles stop behaving purely diffusive (left-most lines) and when large particles begin a purely deterministic displacement (right-most lines).

4.2.6. Influence of diffusion

In 1D during the time step τ a particle diffuses the distance ℓ, the average of which is the size-dependent diffusion length $\sigma(d)$ given by

$$\sigma(d) = \langle \ell \rangle = \sqrt{2D\tau} = \sqrt{2\frac{k_B T}{3\pi\eta d}\frac{\lambda}{u_0}}. \tag{4.16}$$

In our model we discretize the transverse diffusion as the properly rounded number n_{jump} of flow lanes crossed by the particle during diffusion,

$$n_{\text{jump}} = \frac{N}{\lambda}\,\ell. \tag{4.17}$$

The addition of diffusion smears out the displacement of the particles and causes the critical diameter to be larger than in the diffusion-less case (Figure 4.4, open symbols).

4.2.6.1. Bumping criterion for small particles.

Very small particles are completely dominated by diffusion, and the particle distribution at the end of the array is simply given by the transverse diffusion of the particles during the time L/u_0 it takes for the particle to be convected all the way L through the array, see Figure 4.2(a). For small particles we therefore have

$$r_0 = \int_{-\frac{3}{2}\frac{\lambda}{N}}^{\frac{3}{2}\frac{\lambda}{N}} \frac{1}{\sqrt{2\pi\sigma^2}} \exp\left(\frac{-x^2}{2\sigma^2}\right) \mathrm{d}x, \tag{4.18}$$

where $\sigma^2 = 2DL/u_0$. In figure 4.4 we have plotted r_0 versus d/d_c and $r_d = 1 - r_0$ as the thick black curves in the interval $0 < d/d_c < 2.1$.

As the particle diameter d is increased, the bumpers begin to become important as the diffusion length $\sigma(d)$, equation (4.16), is decreased and becomes equal to the displacement length ℓ_{disp}, equation (4.5). Using the criterion $\sigma(d_1) = \ell_{\text{disp}}$, with the parameter values used in figure 4.4, we find that particles stop behaving as small diffusion-dominated particles and start interacting with the bumpers when $d_1 = 2.1\,d_c$. This cross-over value is indicated by the left-most vertical lines in figure 4.4, and it fits well with the simulation data. Note that the specific value of the pre-factor is determined for $d_c = 118\,\text{nm}$.

4.2.6.2. Bumping criterion for large particles.

Large particles will interact with the bumpers at every row in the array and their positions are thus reset at every bump to be ℓ_{disp}, see Figure 4.2(b). Diffusion can

therefore be neglected for such particles. They all follow the displacement path, and $r_1 = 1$.

As the particle diameter is lowered, the probability p_{esc} that a particle escapes the displacement path can be estimated by the probability of diffusing from the displaced position to the last flow lane in the gap, i.e. the distance $\ell_{\mathrm{disp}} - \frac{\lambda}{N}$. This probability p_{esc} is given by (4.8). In figure 4.4 we have plotted $r_d = p_{\mathrm{esc}}$ and $r_1 = 1 - r_d$ as thick black curves in the interval $3.4 < d/d_{\mathrm{c}} < 6$.

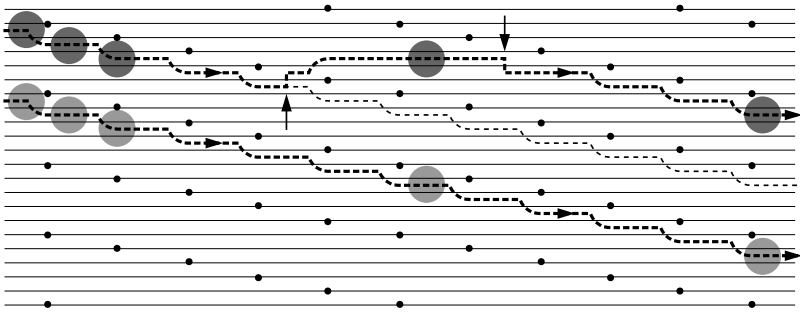

Figure 4.5.: Schematics of an $N = 5$ bumper array (black dots) in which a large particle (light gray) moves along the displacement path (lower thick dashed line) without diffusion, and another particle of the same size (dark gray) moves partially along the displacement path (upper thick dashed line) under the influence of diffusion. The corresponding displacement path without diffusion is also shown (thin dashed line). Two diffusion-induced jumping events, each causing the particle to jump to a neighboring lane, are marked by the vertical arrows. The upward event induces a shift in gap number by one, while the downward event does not induce a shift in gap number. The diffusing particle thus exits the bumper array one gap above its diffusionless counter part.

In order to follow the displacement path, a particle must bump at each row in the array. If we consider an N-periodic array with m full periods, the particles will have mN bumping opportunities as they pass through the entire array. If a particle evades bumping at a bumper, it will be convected by the flow through a full period of the array before bumping is possible again. Because of the escape, it will miss N bumping opportunities and end up one gap from the displacement path, see Figure 4.5. Consequently, if a particle escapes one time, it will only have $(m-1)N$ bumping opportunities and has therefore escaped bumping with a probability of $1/[(m-1)N]$. The upper critical particle size d_2 for convection-

induced displacement is defined using (4.8) as

$$p_{\mathrm{esc}}(d_2) = \frac{1}{(m-1)N}. \tag{4.19}$$

For the device used in the experiments by Larsen [27] we find $d_2 = 3.4d_c$. The predicted upper limit for diffusion dominated motion and the lower limit for convection-induced displacement compare well with the experimental observation by Larsen [27] that some particles end up in a transition region between the displacement path and the zigzag path (Figure 4.3, gray triangles). Based on the data for $1/N = 1/100$ in Figure 4.3 the experimentally observed transition region begins at $d_1 = 0.16w_g = 1.4d_c$ (the highest lying gray triangle) and ends at $d_2 = 0.40w_g = 3.4d_c$ (the lowest lying white triangle). Considering the simplicity of the discrete model this is in fair agreement with our model predictions, $d_1 = 2.1d_c$ and $d_2 = 3.4d_c$.

4.2.7. Conclusion

Experimental data on separation of particles in DLD arrays all show a systematic deviation from predictions made from the bifurcating flow lane model [20, 21, 27]. Application of the model presented in this paper to the available data suggests that this systematic deviation may be explained by diffusion. In addition, we have proposed a simple discrete model for quickly simulating particle separation in DLD arrays. In contrast to the single critical particle size found in earlier analyses solely based on the deterministic separation processes, our work including diffusion identifies two particle sizes characteristic for the separation in DLD arrays: a small particle size, d_1, below which diffusion dominates, and a larger particle size, d_2, above which the deterministic processes govern the sorting. Particles of intermediate sizes will neither follow the average flow direction nor the direction set by the array geometry. If bumper devices are scaled down both d_1 and d_2 are larger than the critical size predicted in the existing literature.

The presented model takes particle diffusion and size dispersion into account and has been validated against experimental data for a bumper device with period $N = 100$. In this example the transition from zigzag paths to displacement paths happens at particle sizes in the interval from 2.1 to 3.4 times the critical particle size predicted from geometrical arguments. This transition interval is in qualitative correspondence with the experimental observations from Larsen [27]. Our discrete model and the estimates presented in this paper suggest that particles smaller than twice the geometrical critical size of the $N = 100$ bumper device behave diffusively and are not affected by the bumpers because the small diffusive particles rarely

come into contact with the bumpers due to random Brownian motion. We do believe that our discrete model will be useful for design and evaluation of DLD arrays with any given specification.

4.3. Multidirectional DLD arrays

Our previous analysis of DLD sorting was focused on predicting r_c as a function of array parameters, the width of the gap between posts and the shift of posts between rows. Once basic hydrodynamics is included, theoretical calculations of r_c agree with experimental results within about 5 % [3, 14, 21]. Inclusion of diffusion in DLD sorting has been described using rough estimations [9, 20, 21], and in more detailed studies that incorporate both microfluidic advection and diffusion to calculate r_c under a range of experimental conditions [14].

Previous analysis of the geometry of the DLD array has been limited to the following conventional case. In a given row the center-to-center distance between the posts is denoted λ, see Fig. 4.6. The subsequent row of posts is placed at a distance $\alpha\lambda$ downstream from the first row. Normally, α is chosen to be unity, however this is not an essential requirement. The posts in this second row are displaced a distance $(1/N)\,\lambda$ along the row, where N traditionally has been an integer. The ratio $1/N$ is also denoted the row-shift fraction ϵ. In row number $N+1$ the posts have the same positions as in the first row, and consequently the array is cyclic with period N. Due to this periodicity of the array and the laminarity of the flow, the stream can naturally be divided into N flow lanes, each carrying the same amount of fluid flux, and each having a specific path through the device [20].

For devices with the simple row-shift fraction $\epsilon = 1/N$ and disregarding particle diffusion, only one critical separation size r_c is introduced. Spherical particles with a radius smaller than r_c will move forward along the main flow direction through the device, defining the angle $\theta = 0$. However, particles with a radius larger than r_c are forced by collisions with the posts to move in a skew direction at an angle θ given by $\tan\theta = 1/(\alpha N)$. Taking diffusion into account the transition from straight to skew motion takes place over a finite range of particle sizes [9, 14, 20, 21].

In this section we generalize the array geometry by studying the effects of row-shift fractions different from that of the conventional, simple $(1/N)$-array. We show in Sec. 4.3.1 that by displacing consecutive rows by the rational fraction $\epsilon\lambda = (M/N)\lambda$, where M is an integer that is not a divisor of N, two new separation modes appear, each associated with a distinctive range of particle sizes and separation directions θ. Furthermore, to test experimental feasibility of the novel separation modes, we present in section. 4.4 a numerical model of the DLD system reduced to its essential elements: particles subject to convection and diffusion through a periodic array of posts. The model includes a particle size-dependent excluded volume around the posts which accounts for the particle-post interactions. With this simple numerical model we investigate the advection and diffusion of

particles in the M/N-array geometries, and discuss possible experimental consequences of the novel multidirectional DLD system.

In the numerical model of the DLD system described in section 4.4 we first study the separation in a post array with point-like obstacles. We maintain a hydrodynamic interaction between the array geometry and the flow by enforcing a no-slip velocity at the point-obstacle. This particular array geometry is currently of interest to researchers looking to apply DLD separation to high-throughput microfluidic devices. Such a reduced post size decreases hydraulic resistance and thus increases the liquid throughput for a given pressure difference applied along the device. One promising method to create such devices is to use arrays of semiconductor nanowires [36] in a microfluidic channel. We also apply our numerical model to post arrays with finite size posts which is more like the post arrays currently produced.

4.3.1. Basic theoretical analysis

The introduction of a non-simple row-shift fraction $\epsilon = M/N$ in the DLD system is first discussed in Sec. 4.3.2 for the specific case of $M/N = 3/8$, since all the novel separation modes are present in that device geometry. Fig. 4.6 shows the principle of the fractionally displaced DLD array leading to multi-directional separation of particles of different sizes. As was the case for the simple row shift fraction $1/N$, the rational row-shift fraction M/N also naturally leads to N flow lanes, each carrying the same amount of fluid flux. In this section, all particles are assumed to follow these flow lanes unless bumped by an interaction with a post. However, in contrast to the traditional DLD geometries, now the posts are displaced M flow lanes instead of just a single flow lane when passing from one row of posts to the next.

In Sec. 4.3.3 we analyze this more general case of M/N-arrays, where the integer row-shift M and the integer array-period N have no common divisors.

4.3.2. The specific row-shift fraction 3/8

First we consider the explicit choice of parameters given in Fig. 4.6, namely, a period $N = 8$, and a row-shift of $M = 3$ lanes in the y-direction $\mathbf{e}_y$, i.e., a row-shift fraction of $\epsilon = 3/8$. The flow $\mathbf{v}$ is in the x-direction $\mathbf{e}_x$. For simplicity, we employ the most simple model where all flow lanes are assumed to have the same width λ/N, and where the particles are not subject to Brownian motion. The analysis can straightforwardly be extended to take the different widths of the flow lanes [21] into account or, as discussed in section 4.2, correct for the effects of diffusion [14].

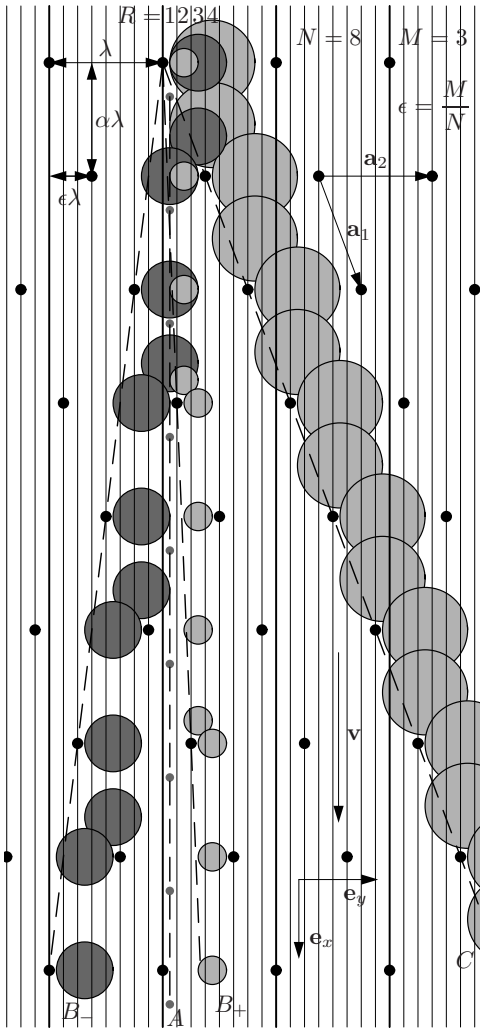

Figure 4.6.: An array of posts (marked by black dots) with period $N = 8$ and a shift of $M = 3$ flow lanes per row, i.e., a row-shift fraction $\epsilon = 3/8 = 0.375$. The flow $\mathbf{v}$ is directed along the x-axis from top to bottom. The dashed lines indicate the four possible separation directions. First, the two well-known modes: the straight mode A with $\theta_A = 0°$ for particles of radius r with $r < (1/N)\lambda$ (small dark gray circles starting in flow lane $R = 1$), and the maximal displacement mode C with $\theta_C = 20°$ for $(3/N)\lambda < r$ (large light gray circles starting in flow lane $R = 4$). Additionally, the two novel separation modes: one B_+ towards the right with angle $\theta_{B_+} = 2.4°$ for $(1/N)\lambda < r < (2/N)\lambda$ (small light gray circles starting in flow lane $R = 2$), and another B_- towards the left with angle $\theta_{B_-} = -7.1°$ for $(2/N)\lambda < r < (3/N)\lambda$ (large dark gray circles starting in flow lane $R = 3$). The solid vertical lines indicate the flow lanes of width λ/N, while $\mathbf{a}_1$ and $\mathbf{a}_2$ are the lattice vectors, and α is an aspect ratio.

The analysis is most easily carried out by considering spherical particles of increasing radius r. As the rows in Fig. 4.6 are shifted to the right, it is natural to choose the starting point of a given particle to be directly to the right of a post, placing the particle's center in flow lane $R = 1, 2, 3$, or 4 according to size.

For the smallest particles with $r < \lambda/N$, labeled A in Fig. 4.6, we obtain a path corresponding to the familiar so-called zigzag path defined in Ref. [20]. Due to the point-like nature of our obstacles, the path is a straight line, indicated by the dashed vertical line in Fig. 4.6. The path angle is $\theta_A = \arctan 0 = 0°$.

For the next set of particles with $\lambda/N < r < 2\lambda/N$, ($B_+$ in Fig. 4.6), we note that they are not affected significantly by passing the second rows of posts. The displacement of $(M/N)\lambda$ is larger than the size of the particle. By simple inspection we find that the particles interact with a post in the fourth row leading to a bump of one lane width to the right. This bumping brings the particles back to a position just right of a post, and we have identified a new separation mode, B_+. The direction of mode B_+ can be characterized by the integers

$$p = \text{the number of rows after which the bumping pattern repeats itself, and} \tag{4.20a}$$

$$q = \text{the number of flow lanes that the particles are bumped to the right while traveling through } p \text{ rows.} \tag{4.20b}$$

Here, with $p = 3$ and $q = 1$ and the array parameters indicated in Fig. 4.6, the path angle of mode B_+ is found to be $\theta_{B_+} = \arctan\left[1/(\alpha \times 3 \times 8)\right] = 2.4°$. Here and in the following we choose the aspect ratio $\alpha = 1$.

For the third set of particles with $2\lambda/N < r < 3\lambda/N$, marked as B_- in Fig. 4.6, we note that they collide with a post in the second row and are bumped two lanes to the left. After two rows, the particles are again bumped two lanes to the left, and we have identified another new separation mode, B_-. Given this period $p = 2$ bumping of $q = -2$ flow lanes (where minus indicates displacement to the left), the path angle of mode B_- is found to be $\theta_{B_-} = \arctan\left[-2/(\alpha \times 2 \times 8)\right] = -7.1°$.

Finally, the fourth set of particles (with $3\lambda/N < r$) is considered, shown as the large light gray circle in Fig. 4.6. Since $3\lambda/N$ equals the row-shift $\epsilon\lambda$, these large particles collide with a post in each row ($p = 1$) where they are bumped $q = M = 3$ lanes to the right. This is the conventional maximal displacement mode C [20]. As a result the path angle for mode C here is found to be $\theta_C = \arctan\left[3/(\alpha \times 8)\right] = 20.6°$.

Table 4.1.: List of separation radii r and angles θ as a function of the integer array parameters N, M, p and q for $\alpha = 1$.

N	M	mode	particle radius in units of lane width	q/p	separation angle θ
5	2	A	$0 < r < 1$	$0/1$	$0.0°$
		B_-	$1 < r < 2$	$-1/2$	$-5.7°$
		C	$2 < r < 2.5$	$2/1$	$21.8°$
7	2	A	$0 < r < 1$	$0/1$	$0.0°$
		B_-	$1 < r < 2$	$-1/3$	$-2.7°$
		C	$2 < r < 3.5$	$2/1$	$15.9°$
7	3	A	$0 < r < 1$	$0/1$	$0.0°$
		B_-	$1 < r < 3$	$-1/2$	$-4.1°$
		C	$3 < r < 3.5$	$3/1$	$23.2°$
8	3	A	$0 < r < 1$	$0/1$	$0.0°$
		B_+	$1 < r < 2$	$1/3$	$2.4°$
		B_-	$2 < r < 3$	$-2/2$	$-7.1°$
		C	$3 < r < 4.0$	$3/1$	$20.6°$
9	2	A	$0 < r < 1$	$0/1$	$0.0°$
		B_-	$1 < r < 2$	$-1/4$	$-1.6°$
		C	$2 < r < 4.5$	$2/1$	$12.5°$
9	4	A	$0 < r < 1$	$0/1$	$0.0°$
		B_-	$1 < r < 4$	$-1/2$	$-3.2°$
		C	$4 < r < 4.5$	$4/1$	$24.0°$
10	3	A	$0 < r < 1$	$0/1$	$0.0°$
		B_-	$1 < r < 3$	$-1/3$	$-1.9°$
		C	$3 < r < 5.0$	$3/1$	$16.7°$
11	2	A	$0 < r < 1$	$0/1$	$0.0°$
		B_-	$1 < r < 2$	$-1/5$	$-1.0°$
		C	$2 < r < 5.5$	$2/1$	$10.3°$
11	3	A	$0 < r < 1$	$0/1$	$0.0°$
		B_+	$1 < r < 2$	$1/4$	$1.3°$
		B_-	$2 < r < 3$	$-2/3$	$-3.5°$
		C	$3 < r < 5.5$	$3/1$	$15.3°$
11	4	A	$0 < r < 1$	$0/1$	$0.0°$
		B_+	$1 < r < 3$	$1/3$	$1.7°$
		B_-	$3 < r < 4$	$-3/2$	$-7.8°$
		C	$4 < r < 5.5$	$4/1$	$20.0°$
11	5	A	$0 < r < 1$	$0/1$	$0.0°$
		B_-	$1 < r < 5$	$-1/2$	$-2.6°$
		C	$5 < r < 5.5$	$5/1$	$24.4°$
12	5	A	$0 < r < 1$	$0/1$	$0.0°$
		B_+	$1 < r < 2$	$1/5$	$1.0°$
		B_-	$2 < r < 5$	$-2/2$	$-4.8°$
		C	$5 < r < 6.0$	$5/1$	$22.6°$

4.3.3. General row-shift fractions M/N

In the general case of a DLD device with period N and a row-shift of M flow lanes, it is useful to introduce the floor function $\lfloor x \rfloor$ of x, which gives the largest integer smaller than or equal to x, eg., $\lfloor 8/3 \rfloor = 2$ and $\lfloor 10/3 \rfloor = 3$, and the ceiling function $\lceil x \rceil$ of x which gives the smallest integer larger than or equal to x.

Using the notation in Fig. 4.6, the flow lane R occupied by the center of the particles can be expressed in terms of the particle radius r as $R = \lceil rN/\lambda \rceil$, so that $R = 1, 2, 3, \ldots, \lceil N/2 \rceil$ for $0 < r < \lambda/2$.

Two cases are straightforward to analyze. For small radii with $R = 1$, the particles will follow the streamlines without any systematic net lateral displacement, i.e., a mode A in the direction $\mathbf{t}_A$ given by

$$\mathbf{t}_A = \alpha\, \mathbf{e}_x, \tag{4.21}$$

and forming the path angle θ_A with the x-axis,

$$\theta_A = 0, \quad R = 1. \tag{4.22}$$

For large radii with $M < R < \lceil \frac{N}{2} \rceil$, the particles collide with the posts and are bumped M flow lanes to the right in each row, but they do not get stuck between the posts; this is mode C. The path is directed along the direction $\mathbf{t}_C$ given by

$$\mathbf{t}_C = \alpha\, \mathbf{e}_x + \frac{M}{N}\, \mathbf{e}_y, \tag{4.23}$$

and forming the path angle θ_C with the x-axis,

$$\theta_C = \arctan\left[\frac{M}{\alpha N}\right], \quad M < R < \left\lceil \frac{N}{2} \right\rceil. \tag{4.24}$$

In a given M/N array, modes with larger sorting angles are excluded because of the post spacing in the y-direction: particles with radius $r > \lambda/2$ are unable to fit between the posts.

If the particles are small enough to pass the second row without getting bumped to the right, but too large for mode A, $1 < R \leq M$, their trajectories fall into one or two B modes.

As a particle is convected through the array, a post will approach the particle from the left in steps of M flow-lanes per row the particle advances, hence the use of modulus M arithmetic in the following analysis.

If $(N \bmod M) < R \leq M$ the particle will hit the post with its center to the left of this obstacle and will therefore enter mode B_- where it is displaced to the left with a period $p_- = \lfloor \frac{N}{M} \rfloor$. This is most readily seen by starting the analysis

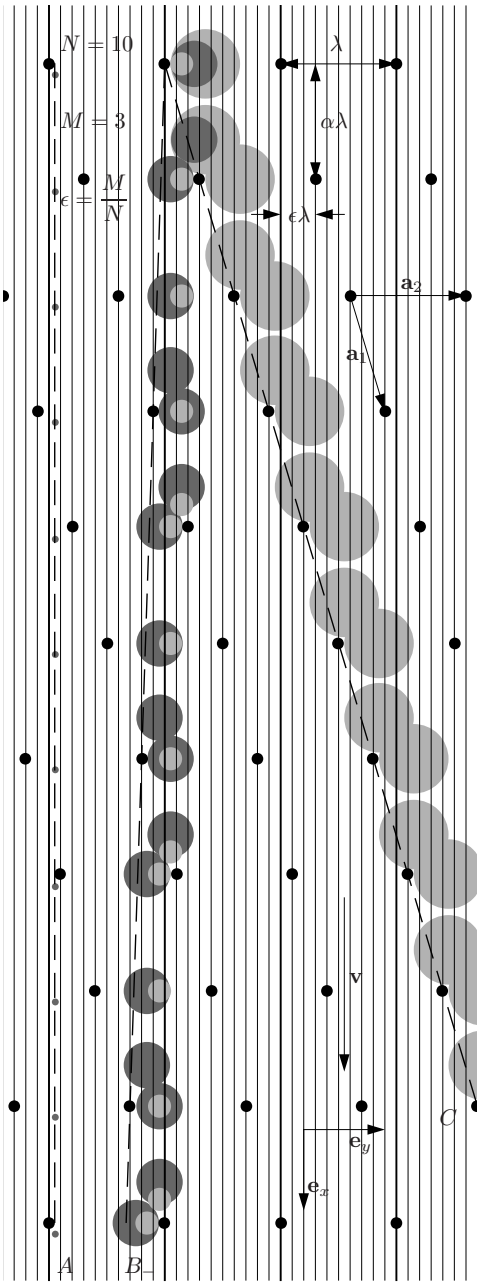

Figure 4.7.: An array with period $N = 10$ and a shift of $M = 3$ flow lanes per row, giving a row-shift fraction $\epsilon = 3/10 = 0.3$. The flow $\mathbf{v}$ is directed along the x-axis from top to bottom. Here there are three sorting modes, delimited by two critical radii. Mode A for particles of radius r with $r < r_{c1} = (1/10)\lambda$ (shown on the far left), and mode C, the maximal displacement mode for $(3/10)\lambda = r_{c2} < r < (1/2)\lambda$ (large light gray circles). A novel mode B_- displaces particles with $r_{c1} < r < r_{c2}$ towards the left (large dark gray and intermediate, light gray circles).

with a particle position just left of a post. A particle with $(N \bmod M) < R \leq \left\lceil (N - R + 1) \bmod M \right\rceil$ will bump left after $p_- = \left\lfloor \frac{N}{M} \right\rfloor$ rows and will again be in a position just left of a post. The small particle in mode B_- of Fig. 4.7 is an example of this behavior. Slightly larger particles with $\left\lceil (N - R + 1) \bmod M \right\rceil < R \leq M$ will bump right after $p = \left\lfloor \frac{N-R+1}{M} \right\rfloor$ rows. Since we are only considering particles with $R \leq M$, this displacement will always be less than M flow lanes, and the particle is therefore bound to bump left on the post in the following row, i.e., after a total of $p_- = \left\lfloor \frac{N}{M} \right\rfloor$ rows. The large B_- mode particle in Fig. 4.7 is an example of this behavior.

The trajectories in mode B_- have period $p_- = \left\lfloor \frac{N}{M} \right\rfloor$. The number q_- of lanes bumped after passing these p_- rows is $q_- = Mp_- - N < 0$. The path is directed along the direction $\mathbf{t}_{B_-}$ given by

$$\mathbf{t}_{B_-} = \alpha p_- \, \mathbf{e}_x + \frac{q_-}{N} \mathbf{e}_y, \tag{4.25a}$$

$$p_- = \left\lfloor \frac{N}{M} \right\rfloor, \tag{4.25b}$$

$$q_- = Mp_- - N < 0, \tag{4.25c}$$

forming the path angle θ_{B_-} with the x-axis,

$$\theta_{B_-} = \arctan \left[\frac{q}{\alpha p_- N} \right] < 0. \tag{4.26}$$

If $1 < R \leq (N \bmod M)$ the particle will enter mode B_+ where it is displaced to the right with a period $p_+ = \left\lfloor \frac{N+R}{M} \right\rfloor$. To realize this it is natural to start the analysis with the particle just right of a post. Again, a post will approach the particle from the left in steps of M lanes as the particle moves through the array. A particle with $1 < R \leq \left\lceil \frac{M}{2} \right\rceil$ will follow the flow for $p_+ = \left\lfloor \frac{N+R}{M} \right\rfloor$ rows and then bump right. If $\left\lceil \frac{M}{2} \right\rceil < R \leq (N \bmod M)$ the particle will bump left already in the second row of posts. The particle is now in a position just left of a post. However, since it is not large enough to follow the B_- path, it will bump right when it meets the post after $p_+ = \left\lfloor \frac{N+R}{M} \right\rfloor$ rows.

The trajectories in mode B_+ have period $p_+ = \left\lfloor \frac{N+R}{M} \right\rfloor$. After p_+ rows the particles will get bumped q_+ flow lanes to the right given by $q_+ = Mp_+ - N > 0$. The path is directed along the direction $\mathbf{t}_{B_+}$ given by

$$\mathbf{t}_{B_+} = \alpha p_+ \, \mathbf{e}_x + \frac{q_+}{N} \mathbf{e}_y, \tag{4.27a}$$

$$p_+ = \left\lfloor \frac{N+R}{M} \right\rfloor, \tag{4.27b}$$

$$q_+ = Mp_+ - N > 0, \tag{4.27c}$$

forming the path angle θ_{B_+} with the x-axis,

$$\theta_{B_+} = \arctan\left[\frac{q_+}{\alpha p_+ N}\right] > 0. \tag{4.28}$$

In terms of the flow lane number R, the criteria for the four different displacement modes can be summarized as follows

$$\text{mode } A, \qquad \text{if } R = 1 \tag{4.29a}$$
$$\text{mode } B_+, \qquad \text{if } 1 < R \leq (N \bmod M) \tag{4.29b}$$
$$\text{mode } B_-, \qquad \text{if } (N \bmod M) < R \leq M \tag{4.29c}$$
$$\text{mode } C, \qquad \text{if } M < R \leq \left\lceil \tfrac{N}{2} \right\rceil. \tag{4.29d}$$

Note that mode B_+ vanishes if $(N \bmod M) = 1$.

We have identified novel sorting modes in a model of transport through a DLD device characterized by row-shift fractions M/N. The two additional sorting modes may provide provide a way for producing efficient DLD devices for separating particles in several distinct sizes by running a sample through a single chip. In devices where the additional sorting modes cannot be completely resolved because the displacement angle deviation is too small the additional sorting modes will appear as a spacial broadening of zigzag particle distributions in experimental data. We hope the above model will help experimentalists easily determine if a DLD device design fall in the latter category. In section 4.4 we propose a finite element based numerical model for verifying the existence of the novel sorting modes as well as the changes of the critical radius caused by diffusion.

4.4. Continuum finite element model

The discrete model presented in the previous sections captures the functionality of the deterministic lateral displacement devices and account qualitatively for the influence of particle diffusion and size dispersion. The discrete models do not account for the actual flow in the array or the shape of the posts. In this section we present a numerical model that extends our previously published model for the particle distribution in a deterministic lateral displacement device taking the flow and the shape of the posts into account. We believe that such a model will be useful for more accurate studies of actual devices and will be important for establishing the feasibility of the multidirectional DLD devices.

Generally the deterministic lateral displacement devices are large compared to the particles. In the following we therefore assume the array to be infinite and only consider the flow in a unit cell of the array. The model takes the hydrodynamic

influence of the array geometry including finite sized posts into account but we do not model the influence of the finite-sized particles on the flow. This simplification allows us to solve the fluid flow and the particle distribution in a two step process because there is only a one-way coupling from the velocity field to the particle distribution.

4.4.1. Implementation

To reduce the computational requirements for solving the problem we use a unit cell of the array as the domain for the simulations, see figure 4.8. We assume the array to be infinitely deep so we can model the flow field and the particle separation using a two-dimensional approximation.

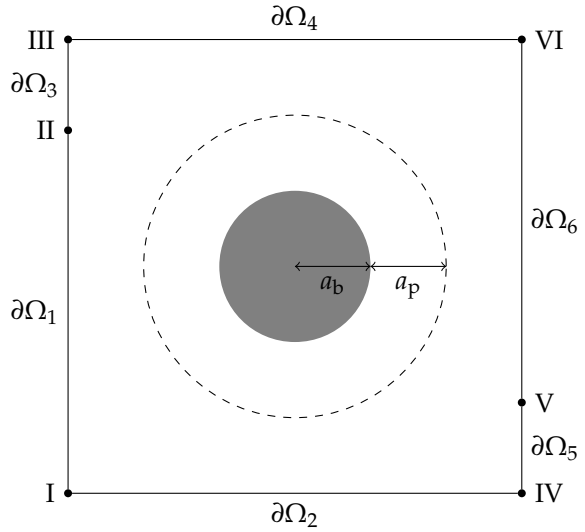

Figure 4.8.: The square unit cell used for simulation of the flow and particle distribution in a deterministic lateral displacement device. The solid gray circle indicates the obstacle with radius a_b. Due to the finite size of the particles there will be an excluded volume around the obstacle which can not be occupied by particles. The width of the excluded volume is given by the particle radius a_p. The flow and particle distribution is solved subject to skew periodic boundary conditions such that boundary $\partial\Omega_1$ and $\partial\Omega_6$ are equivalent, boundary $\partial\Omega_3$ and $\partial\Omega_5$ are equivalent, and boundary $\partial\Omega_2$ and $\partial\Omega_4$ are equivalent. The length of the boundary segments $\partial\Omega_3$ and $\partial\Omega_5$ are M/N of the total side length of the unit cell.

In the following we use the average flow velocity u_0 as the characteristic scale for the flow. The length λ of the sides of the unit cell is used as the characteristic length scale. The side length of the non-dimensional unit cell is therefore 1 and the flow rate through the unit cell is likewise normalized to 1. As in the two previous models we will assume the particles to be spherical with radius a_p and use the Einstein-relation to define the diffusion constant D of the particles

$$D = \frac{k_\mathrm{B} T}{6\pi\eta a_\mathrm{p}}, \tag{4.30}$$

where $k_\mathrm{B} \approx 1.23 \times 10^{-23}\,\mathrm{J\,K^{-1}}$ is Boltzmann's constant, $T = 300\,\mathrm{K}$ is the temperature of the system and $\eta = 1 \times 10^{-3}\,\mathrm{Pa\,s}$ is the viscosity of the fluid. The ratio Pe between convection and diffusion of the particles is introduced as the Péclet number

$$Pe = \frac{\lambda u_0}{D}. \tag{4.31}$$

We imagine the circular obstacle with radius a_b to be placed in the center of the unit cell. The left and right boundaries are divided into two parts of different lengths. The shorter sections of the left and right boundaries are M/N, see figure 4.8. We will use the sectioning of the left and right boundaries for defining 'skew periodic' boundary conditions.

4.4.1.1. The flow in the unit cell

As discussed in the previous sections the separation in deterministic lateral displacement devices rely on laminar flow through the post arrays. We therefore use the non-dimensional Stokes equation (Eq. (2.8)) as the governing equation to model the flow

$$0 = \boldsymbol{\nabla} \cdot \boldsymbol{\sigma} \tag{4.32}$$

as well as the incompressibility condition (Eq. (2.7))

$$0 = \boldsymbol{\nabla} \cdot \boldsymbol{u}. \tag{4.33}$$

The flow must be solved subject to no-slip boundary conditions at the surface of the obstacles. In order to model the displacement of the consecutive rows of obstacles we use skew periodic boundary conditions on the perimeter of the unit cell as indicated in figure 4.8. We do this by mapping the values of the velocity components from the bottom boundary to the top boundary and then specify a Dirichlet condition here to ensure that the velocity field is periodic from from bottom to top. Similarly, we map the values of the velocity components from the two boundary segments at the right of the unit cell to the boundary segments of

similar length at the left of the unit cell and specify a Dirichlet condition on the velocity. Specifying the boundary conditions for the velocity in this way is easy and very intuitive. The flow field resolving from solving the flow subject to such boundary conditions will be 'skew periodic' and we can recreate the flow in an entire DLD device by placing unit cells on a grid defined by $(i, j - Mi/N)$, where i and j are integers.

The boundary conditions for the pressure are not as easy. One approach could be to drive the fluid through the unit cell by applying a pressure drop Δp from the left to the right of the cell. But we also need to specify a condition on the pressure in order to force the overall flow direction to be in the horizontal direction. In a physical device this would be ensured by solid walls near the edges of the devices. This is not easy to implement in our numerical model. To remedy this problem we do not implement Eq. (4.32) and Eq. (4.33) directly but introduce a stream function ψ defined as

$$\boldsymbol{u} = \left(\partial_y \psi, -\partial_x \psi\right), \tag{4.34}$$

which ensures that the incompressibility condition is automatically satisfied. Taking the divergence of Eq. (4.32) we obtain in terms of ψ

$$0 = \nabla^2(\partial_x v - \partial_y u) = -\nabla^2(\nabla^2 \psi), \tag{4.35}$$

i.e., ψ fulfills the fourth-order bi-harmonic equation. These equations are independent of the pressure which we can therefore eliminate from the original equations and still obtain the same solution for the stream function. In the stream function formulation we therefore to not need to solve for the pressure and hence do not have to specify boundary conditions for the pressure. In stead we must specify the conditions on the velocity as Neumann conditions on ψ and specify the total flow rate through the unit cell and enforce the average flow direction by prescribing the value of ψ as a Dirichlet condition at the corners of the unit cell (see figure 4.8). By setting $\psi = 0$ at point I and IV and $\psi = 1$ at point III and VI we ensure that a continuous stream line connects each pair of corner points, i.e., the average flow direction is in the horizontal direction as desired. The difference in the value of the stream function from top to bottom of the unit cell is exactly the flow rate into the cell which in this way is constrained to unity.

The implementation of the stream function in Comsol can be seen in listing 4.1. To handle the fourth order equation for ψ and to ensure that the velocity components, i.e., the derivative of the stream function, are continues across mesh element boundaries we have used the high-order Argyris element `'sharg_2_5(''psi'')'` as the shape function of the stream function in Comsol.

```
fem.form = 'general';
fem.frame = {'ref'};
fem.sdim = {'x','y'};
fem.shape = {'sharg_2_5(''psi'')'};
fem.gporder = {[8] [4]};

% Subdomain settings
fem.equ.ind = {[1]};
fem.equ.dim = {'u','v'};
fem.equ.expr = {...
  'u','psiy','ux','psiyx','uy','psiyy', ...
  'v','-psix','vx','-psixx','vy','-psixy'};
fem.equ.ga = {{{'2*ux';'uy+vx'};{'uy+vx';'2*vy'}}};
fem.equ.f = {{'0';'0'}};

% Boundary settings
fem.bnd.ind = {[1] [3] [4] [7:10]};
fem.bnd.dim = {'u','v'};
fem.bnd.expr = {'u','psiy','v','-psix'};
fem.bnd.constr = {...
    {'u_out2-u' 'v_out2-v'}, ...
    {'u_out1-u' 'v_out1-v'}, ...
    {'u_bot-u'  'v_bot-v'}, ...
    {'u' 'v'}};

% Point settings
fem.pnt.ind = {[2,4:7,9] [1,8] [3,10]};
fem.pnt.constr = {0,'psi','1-psi'};
fem.pnt.constrf = {0,'test(psi)','test(psi)'};
```

Listing 4.1: Comsol code for specifying Stokes equation in terms of a stream function ψ.

In figure 4.9 we show a surface plot of the velocity field from a typical simulation.

4.4.1.2. The particle distribution in the unit cell

Following Li and Drazer [29] and Mikkelsen and Bruus [34] we use the Fokker-Planck equation to describe the transport of the suspended particles in terms of the

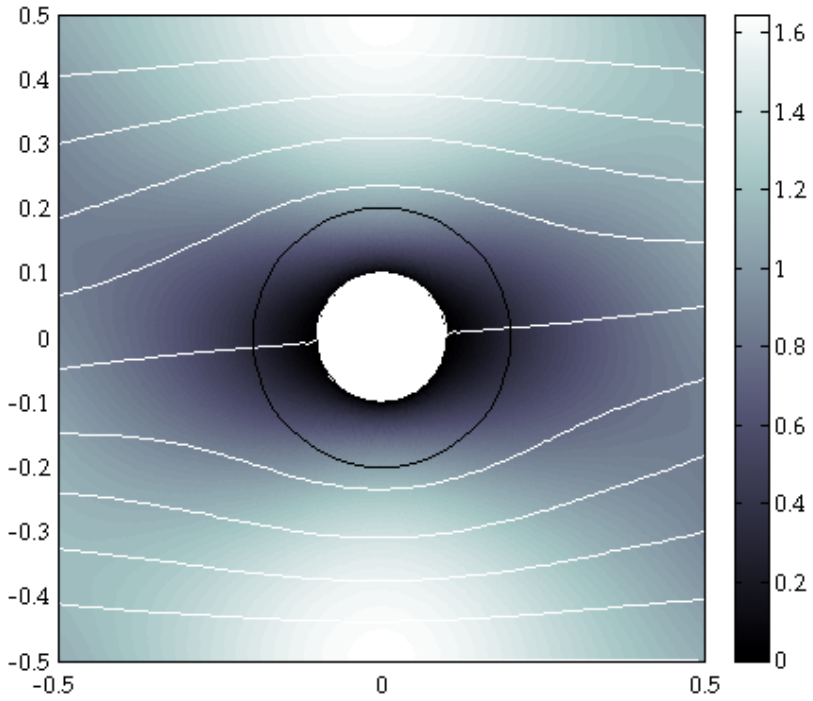

Figure 4.9.: A gray scale plot of the magnitude $\sqrt{\boldsymbol{u}\cdot\boldsymbol{u}}$ of the velocity field in the unit cell. Here the bumper (white circle in the center of the cell) radius is $a_\mathrm{b} = 0.1$. The excluded volume for at particle with radius a_p is indicated by the black circle. The white flow lines indicate the laminar flow lanes.

reduced probability density c [49]

$$\boldsymbol{\nabla}\cdot\left(\boldsymbol{u}c - \frac{1}{Pe}\boldsymbol{\nabla}c\right) = 0, \tag{4.36}$$

where $\boldsymbol{u}$ is the velocity field found from solving Stokes equation and Pe is the Péclet number for a given particle size as defined above. The reduced probability density is defined and normalized inside a unit cell with periodic boundary conditions. Implementation of Eq. 4.36 in Comsol is done using the general equation form and setting `fem.equ.ga` equal to the expression in the parenthesis (see lines 6–13 of code listing 4.2).

We solve Eq. 4.36 subject to the same skew periodic boundary conditions as defined above on the outer boundaries of the unit cell. As mentioned, the particle-

obstacle interaction is modeled as an excluded volume around the posts. The boundary of the excluded volume is therefore impermeable to particles which we enforce by specifying a no-flux condition

$$\boldsymbol{n} \cdot \left(\boldsymbol{u}c - \frac{1}{Pe} \boldsymbol{\nabla} c \right) = 0, \tag{4.37}$$

at the boundary of the excluded volume (see lines 15–22 of code listing 4.2).

The implementation of the Fokker-Plank equation can be seen in code listing 4.2.

```
1  fem.form = 'general';
2  fem.frame = {'ref'};
3  fem.sdim = {'x','y'};
4  fem.shape = {'shlag(2,''c'')'};
5
6  % Subdomain settings
7  fem.equ.ind = {[1] [2]};
8  fem.equ.dim = {'c'};
9  fem.equ.ga = {{{'c*u-1/Pe*cx';'c*v-1/Pe*cy'}};{{'0';'0'}}}; %
       ;{{'0';'0'}}
10 fem.equ.f = 0;
11 fem.equ.init = {'1/(1-a*a*pi)' 0};
12 fem.equ.shape = {[1] []};
13 fem.equ.sshape = 1;
14
15 % Boundary settings
16 fem.bnd.ind = {[1] [3] [4] [2,5,6] [7:10]};
17 fem.bnd.g = { ...
18     '-(nx*u+ny*v)*c+1/Pe*(nx*cx+ny*cy)' ...
19     '-(nx*u+ny*v)*c+1/Pe*(nx*cx+ny*cy)' ...
20     '-(nx*u+ny*v)*c+1/Pe*(nx*cx+ny*cy)' ...
21     '-(nx*u+ny*v)*c+1/Pe*(nx*cx+ny*cy)' ...
22     0};
23 fem.bnd.constr = {...
24     {'c_out2-c'}, ...
25     {'c_out1-c'}, ...
26     {'c_bot-c'}, ...
27     0 0};
```

Listing 4.2: Comsol code for specifying the Fokker-Planck equation.

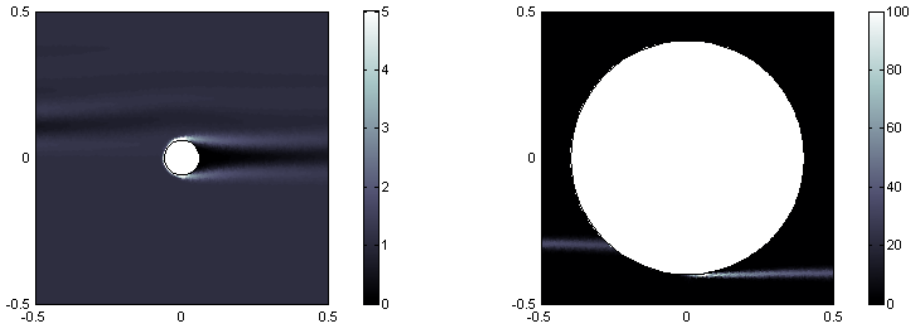

(a) (b)

Figure 4.10.: Gray scale plot of the reduced probability density distribution c of particles in a deterministic lateral displacement device with $N = 10$, $M = 1$, and a point obstacle in the center of the unit cell. (a) Distribution of particles with $a_\mathrm{p} = 0.05 w_\mathrm{g}$. Due to the rapid diffusion of the small particles and the fact that the particles are only slightly displaced due to the hard-wall interaction with the bumper the particle distribution is almost uniform indicating that the particles follow the flow. (b) Distribution of particles with $a_\mathrm{p} = 0.4 w_\mathrm{g}$. The reduced probability density is almost zero everywhere except in a narrow band. This is due to the large excluded volume which collapses the distribution function because all particles will interact with the bumper when passing the unit cell.

4.4.2. Results

Using the model introduced above we wish to verify the findings from the previous two models. In particular, we wish to verify the result that diffusion leads to a larger critical size and introduces a smeared out transition between the different sorting modes. We also wish to verify the findings from the analysis of the multidirectional deterministic lateral displacement devices that a row shift fraction M/N with $M > 1$ can introduce additional sorting angles. Furthermore we will use the numerical model to address the question of the influence of finite-sized obstacles on the separation in deterministic lateral displacement devices.

For the calculations presented below we we have used the following experimentally relevant parameter values. We assume the carrying fluid to be water at room temperature $T = 300\,\mathrm{K}$ with viscosity $\eta = 1 \times 10^{-3}\,\mathrm{Pa\,s}$. The side length of the unit cell is $\lambda = 10\,\mu\mathrm{m}$. We have carried out simulations for two different obstacle

radii; a point-shaped obstacle with $a_\mathrm{b} = 0\,\mu\mathrm{m}$ and a finite-sized circular obstacle with $a_\mathrm{b} = 3\,\mu\mathrm{m}$. In the four array geometries we have carried out simulations with particle radii ranging from $0.02w_\mathrm{g}$ to $0.46w_\mathrm{g}$ for a series of different average flow velocities u_0 ranging from $1\,\mu\mathrm{m/s}$ to $200\,\mu\mathrm{m/s}$.

For each array geometry we have solved for the periodic flow using the stream function implementation described above. We have then used the flow solution as input for solving Fokker-Plank equation in an excluded volume geometry for each set of particle radii and average flow velocities.

The main quantity of interest when analyzing the results of the numerical simulations is the displacement angle θ. The average flow velocity has been constrained to the horizontal direction due to the point conditions on the stream function ψ. This is the direction given by $\theta = 0$. The displacement angle for a particle is defined in terms of the average probability fluxes F_x and F_y in the horizontal and vertical directions, respectively

$$(F_x, F_y) = \frac{1}{A}\int_\Omega (c\boldsymbol{u} - \frac{1}{Pe}\boldsymbol{\nabla} c)\,\mathrm{d}\boldsymbol{r}. \tag{4.38}$$

The displacement angle is then defined as

$$\theta = \mathrm{atan}\left(\frac{F_y}{F_x}\right). \tag{4.39}$$

4.4.3. Transport in arrays with point-obstacles

The deterministic lateral displacement device with point-shaped obstacles is the simpler to understand and compare with the observations from the discrete model including diffusion and the analysis of the multidirectional DLD devices. We therefore start the discussion of the results from the numerical finite element model by examining the findings from running the simulations using a geometry with $a_\mathrm{b} = 0$. Unlike the model presented in Ref. [31] we constrain the flow velocity to zero at the point-obstacle in order to include the effect of a non-uniform flow profile in the gap between two posts.

The 1/10-arrays have according to section 4.3.3 two distinct sorting modes A and C with the directions $\boldsymbol{t}_A$ and $\boldsymbol{t}_C$ given by

$$\boldsymbol{t}_A = \boldsymbol{e}_x, \tag{4.40a}$$

$$\boldsymbol{t}_C = \boldsymbol{e}_x + \frac{1}{10}\boldsymbol{e}_y. \tag{4.40b}$$

The corresponding displacement angles are

$$\tan\theta_A = 0, \tag{4.41a}$$

$$\tan\theta_C = \frac{1}{10}. \tag{4.41b}$$

Running the simulations for a device with $N = 10$ and $M = 1$ result in a separation angle vs. particle radius as shown in figure 4.11. As expected, we find the two sorting modes A, given by the average flow direction, and C, given by the geometry because of the row shift fraction $1/N = 0.1$.

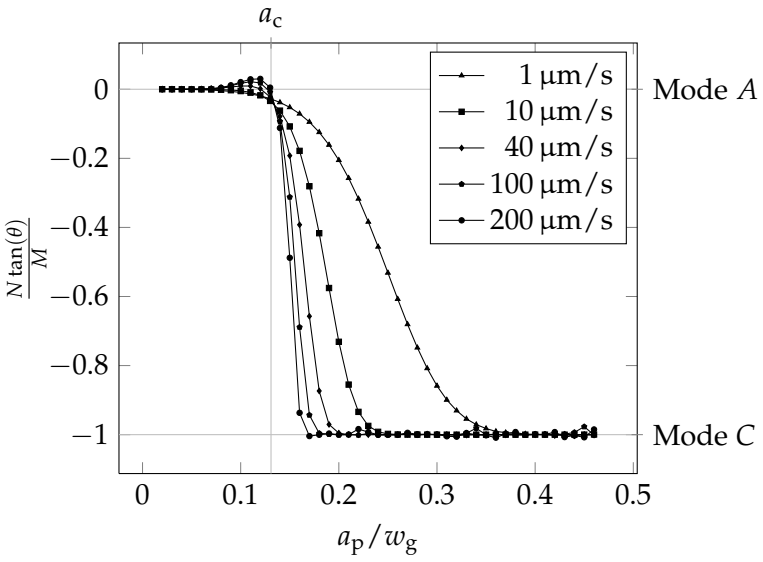

Figure 4.11.: Normalized sorting directions as a function of particle radius a_p/w_g for a device with $N = 10$ and $M = 1$ for a range of flow velocities. Diffusion blurs the ideal sharp transition between the two sorting modes of the device and the true critical radius is shifted towards larger particle sizes than the width a_c of the flow lane nearest to the obstacle.

As the average velocity u_0 of the flow is increased the transition from mode A to displacement mode C approaches the sharp transition given by the width a_c of the flow lane carrying $1/N$ of the total flow through the unit cell. This distance is found from the stream function

$$|\psi(0,0) - \psi(0,a_c)| = \frac{1}{N}. \tag{4.42}$$

In the case of a point-shaped post in the $1/N$-array, $a_c = 0.13$ as indicated by the vertical gray line in figure 4.11. The speeds at which diffusion becomes negligible

can be estimated by comparing the time, λ/u_0 it takes a particle to be advected horizontally along the x-direction through the unit cell to the time used by a particle to diffuse transverse to the general flow direction to reach a position where it would be bumped, $2D/(a_\mathrm{p} - a_\mathrm{c})^2$. For flow speeds

$$u \gg \frac{2D\lambda}{(a_\mathrm{p} - a_\mathrm{c})^2} \tag{4.43}$$

diffusion can be neglected and we would obtain a sharp transition at $a_\mathrm{p} = a_\mathrm{c}$.

One interesting thing to note is the small positive displacement of particles with a radius slightly smaller than a_c. This deviation from the predictions in the previous sections of the transition from mode A to mode C for the higher convection velocities is an effect caused by the non-uniform flow profile induced by the no-slip condition at the point-obstacles. By inspecting particle probability density distributions for particle sizes near the region of interest we can obtain an understanding of what is happening. In figure 4.12 we show four representative distributions.

Very small particles as shown in figure 4.12(a) are displaced less than the row-shift fraction and will consequently have time to diffuse during convection through N cells of the array before they are again in the vicinity of an obstacle. Therefore diffusion completely smears out the effect of the bumper and the particles follow the overall flow direction. Slightly larger particles as shown in figure 4.12(b) are displaced more than the row-shift fraction $1/N$ but less than the width of the flow lane nearest to the bumper. The analysis is therefore similar to the analysis of the B_- mode in the general M/N DLD arrays. As the particle radius is increased further as in figure 4.12(c) the particles are slightly larger than a_c but some particles still manages to escape consecutive bumping because they diffuse. This leads to an average displacement angle less than the geometrically defined angle followed by the larger particles shown in figure 4.12(d). In the latter case the particle still diffuse but due to their size escaping bumping is very improbable.

In the case of an array with $N = 10$ and $M = 3$ our analysis from section 4.3.3 tells us that we have three distinct sorting modes, mode A following the average flow direction, mode C following the array displacement and one of the novel sorting modes, mode B_-, introduced by the row shift fraction $\epsilon = 3/10$. The directions $\boldsymbol{t}_A$ and $\boldsymbol{t}_C$ of the conventional modes A and C are given directly by Eqs. (4.21) and (4.23)

$$\boldsymbol{t}_A = \boldsymbol{e}_x, \tag{4.44a}$$

$$\boldsymbol{t}_C = \boldsymbol{e}_x + \frac{3}{10}\,\boldsymbol{e}_y, \tag{4.44b}$$

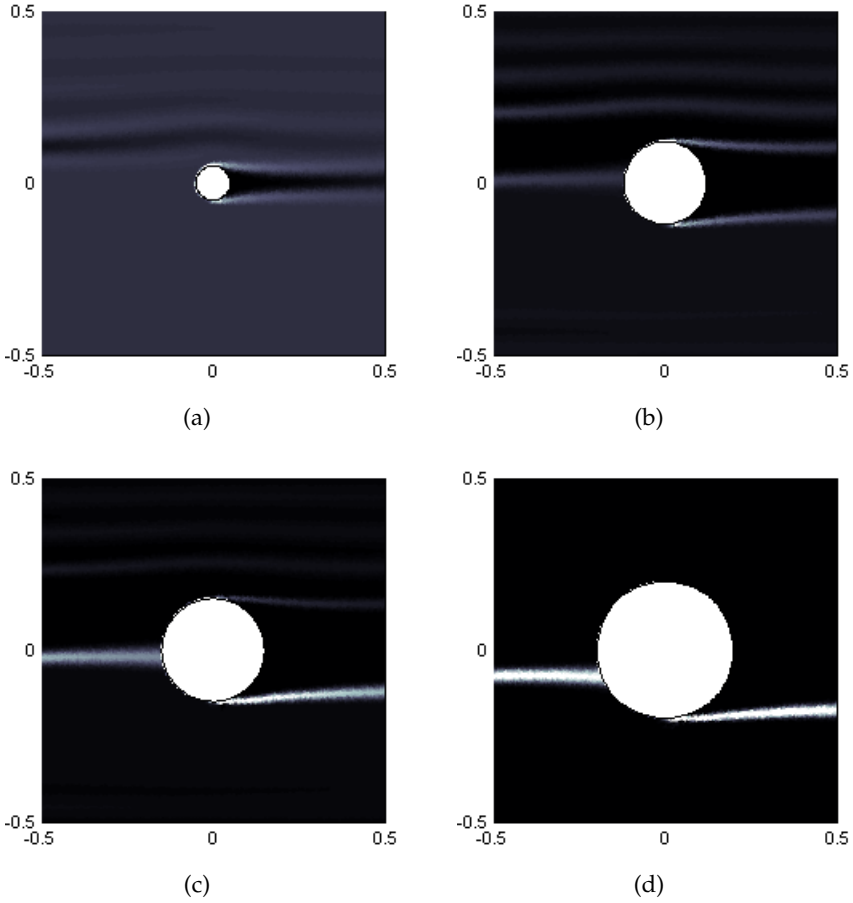

Figure 4.12.: Particle probability density distributions for particles near the transition from displacement mode A to mode C. The array has $N = 10$, $M = 1$ and a point-shaped post in the center. All surface plots are for an average flow velocity $u_0 = 100\,\mu\text{m/s}$. The white circle in each subfigure is the excluded volume for the corresponding particle radius. (a) Particles with radius $a_\text{p} = 0.05$ have an almost uniform distribution before the post. This leads to the sorting direction $\theta = 0$. (b) Particles with radius $a_\text{p} = 0.12$ are slightly larger than the row-shift fraction but the non-uniform flow profile causes the particles to diffuse towards the center of the unit cell causing a significant fraction of the particles to bump in the upward direction. (c) Particles with radius $a_\text{p} = 0.15$ are for the most part bumped by the obstacles but a fraction of the particles are still bumped in the upward direction. On average these particles are therefore displaced less than the geometrical displacement of the array. (d) Particles with radius $a_\text{p} = 0.20$ cannot diffuse enough to escape bumping. The probability density function is therefore collapsed into a narrow band and the particles will bump all the way through the array.

while the direction $\boldsymbol{t}_{B_-}$ of mode B_- is found through the path period $p_- = \left\lfloor \frac{N+R}{M} \right\rfloor = \left\lfloor \frac{10+1}{3} \right\rfloor = 3$ and the lane shift $q_- = p_- M - N = 3 \times 3 - 10 = -1$, and thus

$$\boldsymbol{t}_{B_-} = 3\,\boldsymbol{e}_x - \frac{1}{10}\,\boldsymbol{e}_y. \tag{4.44c}$$

The corresponding displacement angles become

$$\theta_A = \quad 0.0°, \quad 0 < r < a_{c1}, \tag{4.45a}$$
$$\theta_{B_-} = \quad 1.9°, \quad a_{c1} < r < a_{c2}, \tag{4.45b}$$
$$\theta_C = -16.7°, \quad a_{c2} < r \ < \frac{1}{2}, \tag{4.45c}$$

where a_{c1} and a_{c2} are the width of the first and the three first flow lanes near the obstacle, respectively.

Solving for the particle probability distributions using our numerical model yields a displacement angle vs. particle radius plot as shown in figure 4.13. According to the analysis of the multidirectional displacement devices there are two critical radii a_{c1}: the width of the first flow lane near the obstacle and a_{c2} the width of the first $M = 3$ flow lanes near the obstacle. Again we find the critical radii using the stream function

$$|\psi(0,0) - \psi(0,a_{c1})| = \frac{1}{N} \tag{4.46a}$$
$$|\psi(0,0) - \psi(0,a_{c2})| = \frac{3}{N}. \tag{4.46b}$$

The angle vs. particle radius plot (figure 4.13) clearly shows the three sorting modes of the 3/10-array. Again diffusion smears out the transitions between the different sorting modes and shifts the critical particle size for the B_- to C transition towards larger particles. One interesting point is that for the very slow average flow velocity $u_0 = 1\,\mu\text{m/s}$ mode B_- completely vanishes and only mode A and C is present. This corresponds well with the estimate for when diffusion can be neglected from Eq. (4.43).

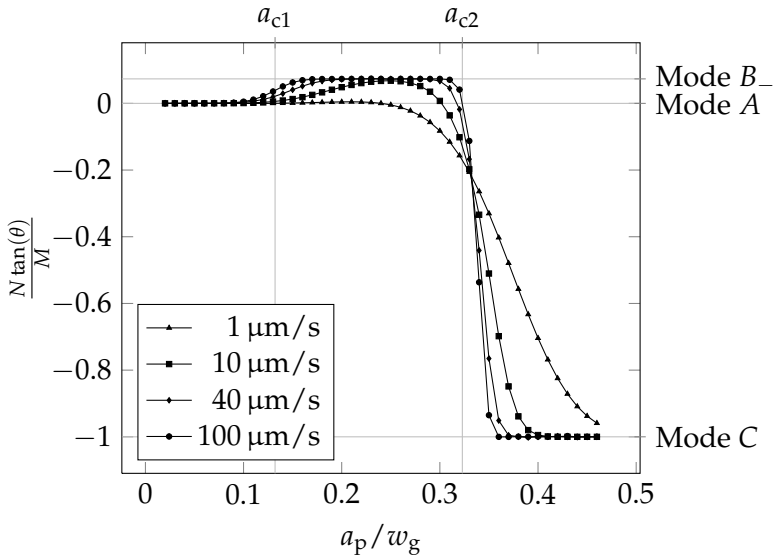

Figure 4.13.: Normalized sorting directions as a function of particle radius for a device with $N = 10$ and $M = 3$ for a range of flow velocities. Diffusion blurs the ideal sharp transition between the three sorting modes of the device and the true critical radius is shifted towards larger particle sizes than the width a_{c2} of the three flow lane nearest to the obstacle. The width a_{c1} of the flow lane nearest to the obstacle indicates the transition to sorting mode B_- for the diffusion less case.

4.4.3.1. Transport in array with finite-sized obstacles

The influence of finite sized posts have until now only been considered in terms of the gap width, w_g, to post separation, λ, ratio. The actual hydrodynamic changes introduced by the change in geometry was reduced to changing the width of the parabolic flow profile in section 4.2 and was not considered in the analysis of the multidirectional sorting modes in section 4.3. Real deterministic lateral displacement devices typically have post radii that are comparable to the gap width. The device used by Larsen *et al.* [27] used a post with a diameter of 7 μm and a gap of only 1 μm and Huang *et al.* [20] used a device with equal gap and post diameter of 8 μm.

The finite element implementation allows us to investigate the influence of finite-sized posts on the separation in DLD arrays. Here we will use a DLD device with $N = 10$ and $M = 1$ and a post radius $a_b = 0.3$ as example. In figure 4.14 we show the displacement angle vs. particle radius for the device. Compared with the corresponding plot for the point-shape obstacle device (figure 4.11) the most noticeable difference is that the shift in the actual critical radius towards larger particle sizes compared with the width a_c of the flow lane nearest to the obstacle. An other interesting observation is that the smearing of the separation curve for an average speed of the carrying fluid of $u_0 = 1\,\mu\text{m/s}$ is much greater.

4.4.4. Conclusion

Treating the particle–obstacle interaction as an excluded volume and using the Fokker–Planck equation to describe the particle distribution in the DLD arrays allows us to efficiently test the expected properties of a device design. Our numerical continuum model confirms the shift in critical radius predicted by the simpler discrete model. The shift towards larger critical radii when diffusion influences the separation process is further enhanced when the obstacles have a finite size.

The implementation suggested here could provide the grounds for future studies of DLD devices. Among the interesting things to explore are the effects of changing the post shape. Narrow elongated posts that are placed parallel to the flow would ensure that the flow lanes keep an almost equal width throughout the array, but steric hindrance would influence the motion of large particles through most of the passage through the arrays. Narrow elongated posts placed transverse to the flow would have a huge effect on the flow but particle interaction with the obstacles would only occur in a small fraction of the time the particles spend in the array. Another interesting possibility is to use topology optimization to optimize the obstacle shape. The time-independent formulation presented here should be easily adaptable to e.g. the topology optimization routine by Olesen *et al.* [42].

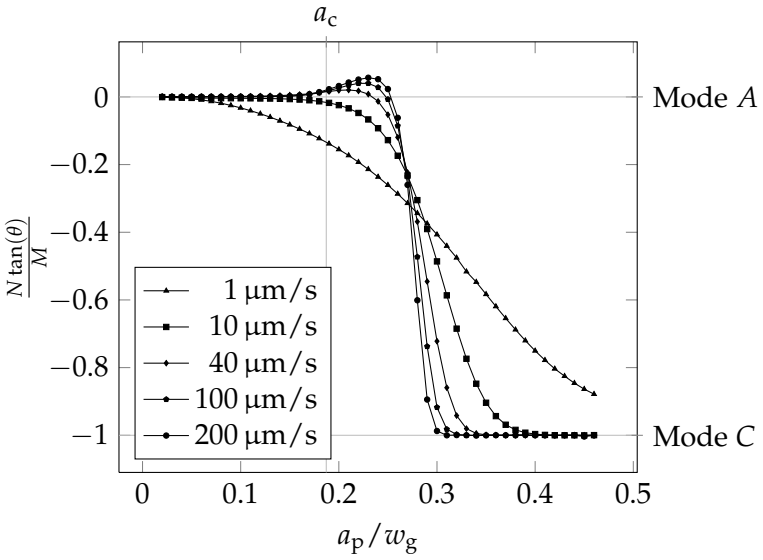

Figure 4.14.: Normalized sorting directions as a function of particle radius for a device with $N = 10$ and $M = 1$ for a range of flow velocities. The radius of the post is Diffusion blurs the ideal sharp transition between the three sorting modes of the device and the true critical radius is shifted towards larger particle sizes than the width a_{c2} of the three flow lane nearest to the obstacle.

5. Conclusions and outlook

During the work with the present thesis we have setup a flexible framework for making numerical simulations of microfluidic systems with free surfaces as well as a model of the separation of particles using the principle of deterministic lateral displacement.

The implementation of the free surface flows in domains with deforming boundaries has been applied to the problem of drawing liquid films from a bath of Newtonian liquid. The results accurately reproduce the analytical predictions in the low capillary number regime and the code is robust enough to handle variations in capillary number over several decades. The robustness and accuracy of the code is aided by the implementation of the boundary condition at the free surface. We have used an arbitrary Lagrangian–Eulerian formulation in order to accurately track the position of the liquid/gas interface and have proposed a general way to implement the free surface boundary condition in a fashion that takes both surface tension and Marangoni stresses into account without the need to explicitly calculate the curvature of the interface. This greatly improves the performance of the code because calculation of the interface curvature would require finding second-order derivatives at the boundary – something that is not easily done numerically.

We hope that the generality of the code will make it useful for analyzing the experimental results on the drawing of liquid films that are expected to be obtained by Ernst van Nierop and Howard A. Stone within the near future.

The proposed models of the separation by deterministic lateral displacement have helped draw attention to the importance of careful device design in order to obtain sorting of particles at the expected critical size. Ideally, the suspended particles can be send through the DLD devices using a high flow rate. In that case diffusion becomes negligible. However, oftentimes practical issues or experimental shortcomings will limit the possible flow rates making diffusion play an important role that should be considered when designing the devices. Diffusion will play a particularly important role if the particles to be separated are very small. Modern micro fabrication techniques easily allow to produce DLD devices with gap sizes in the sub-micro meter regime. Such devices will have large hydraulic resistances and driving the liquid through the device fast enough to impede diffusion becomes a challenge. Here it can prove useful to tweak the design parameters by numerical

simulations before fabrication of the devices.

We have put forward the novel concept of multi-directional deterministic lateral displacement devices. We believe that additional sorting modes may be useful in some applications. The presence of the additional sorting modes is also important to consider when designing devices – even if one do not wish to utilize the extra critical particle sizes. In particular, the presence of one of the multi-directional sorting modes may experimentally lead to extra broadening of the main sorting directions if the sorting angles are not fully resolved. We hope that our analysis of the novel sorting directions will prove helpful to avoid such array designs.

The implementation of a model for the sorting of particles in DLD devices in Comsol can prove to be a useful tool for future analysis of array designs. In the view of the author, it would be particularly interesting to study the effects of different post shapes on the sorting efficiency of DLD arrays. Examining designs with long and slender obstacles (1d-like) could be an interesting way to affect the hydrodynamic impact on the flow by the posts and the influence of particle–obstacle interaction caused by steric hindrance. If a long and slender obstacle is placed parallel to the average flow direction the time for particle–obstacle interaction is maximized while the disturbance of the flow is small due to the small cross-sectional area of the obstacle. If a slender obstacle is placed transverse to the average flow direction the cross-sectional area seen by the flow is large but the time for the particles to interact with the obstacle is very short. Another possible fruitful path to explore it topology optimization of the bumper-shape. The time-independent unitcell formulation proposed in the thesis is well suited for implementation in existing Comsol topology optimization codes [42].

Bibliography

[1] George B. Arfken and Hans J. Weber. *Mathematical Methods for Physicists*. Harcourt Academic Press, 5 edition, 1966.

[2] Rune Barnkob and Mathias Bækbo Andersen. Two phase flow by level set method. Course report, Department of Micro and Nanotechnology, Technocal University of Denmark, 2007. `http://www2.mic.dtu.dk/research/MIFTS/publications/3week/Jan2007_capillarity.pdf`.

[3] Jason P. Beech and Jonas O. Tegenfeldt. Tuneable separation in elastomeric microfluidics devices. *Lab on a Chip*, 8(5):657–659, 2008.

[4] Steffen Berg, Eric A. Adelizzi, and Sandra M. Troian. Experimental study of entrainment and drainage flows in microscale soap films. *Langmuir*, 21: 3867–3876, 2005.

[5] Christopher James William Breward. *The Mathematics of Foam*. PhD thesis, University of Oxford, St Anne's College, 6 1990.

[6] Henrik Bruus. *Theoretical Microfluidics*. Oxford Oxford University Press, 2007.

[7] Comsol Multiphysics. `http://www.comsol.com`.

[8] Robert D. Cook, David S. Malkus, Michael E. Plesha, and Robert J. Wiltt. *Concepts and Applications of Finite Element Analysis*. John Wiley & Sons, 2002.

[9] John A Davis, David W Inglis, Keith J Morton, David A Lawrence, Lotien R Huang, Stephen Y Chou, James C Sturm, and Robert H Austin. Deterministic hydrodynamics: taking blood apart. *Proceedings of the National Academy of Sciences of the United States of America*, 103(40):14779–14784, 2006.

[10] P. G. de Gennes, F. Brochard-Wyart, and D. Quéré. *Capillarity and Wetting Phenomena: Drops, Bubbles, Pearls, Waves , Springer Verlag (New York, 2004).* Springer Verlag, New York, 2004.

[11] Markus Deserno. The shape of a straight fluid meniscus. Max-Planck-Institut für Polymerforschung, `http://www.mpip-mainz.mpg.de/~deserno/science_notes/meniscus/meniscus.pdf`, 3 2004.

[12] X. Fanton, A. M. Cazabat, and D. Cuéré. Thickness and shape of films driven by a marangoni flow. *Langmuir*, 12:5875–5880, 1996.

[13] Oliver Geschke, Henning Klank, and Pieter Telleman. *Microsystem Engineering of Lab on a Chip Devices*. Wiley, 2008.

[14] M. Heller and H. Bruus. A theoretical analysis of the resolution due to diffusion and size dispersion of particles in deterministic lateral displacement devices. *Journal of Micromechanics and Microengineering*, 18(7):075030 (6 pp.), 2008.

[15] Martin Heller. Dynamics of finite-sized particles in microfluidic systems. MSc thesis, Department of Micro- and Nanotechnology, Technical University of Denmark, 7 2005. `http://www2.mic.dtu.dk/research/MIFTS/publications/MSc/MScMHE.pdf`.

[16] HemoCue AB. `http://www.hemocue.com`.

[17] Howard A. Stone's reseach group. School of Engineering and Applied Sciences, Harvard University. `http://www.seas.harvard.edu/fluidsgroup/`.

[18] H. H. Hu. Direct simulation of flows of solid-liquid micxtures. *Journal of Multiphase Flow*, 22:335–352, 1996.

[19] Howard H. Hu, N. A. Patankar, and M. Y. Zhu. Direct numerical simulations of fluid–solid systems using the arbitrary lagrangian–eulerian technique. *Journal of Computational Physics*, 169:427–462, 2001.

[20] Lotien Richard Huang, Edward C. Cox, Robert H. Austin, and James C. Sturm. Continuous particle separation through deterministic lateral displacement. *Science*, 304(5673):987–990, 2004.

[21] D.W. Inglis, J.A. Davis, R.H. Austin, and J.C. Sturm. Critical particle size for fractionation by deterministic lateral displacement. *Lab on a Chip*, 6(5):655–658, 2006.

[22] Mads Jacob Jensen. *Numerical Simulations of Interface Dynamics in Microfluidics*. PhD thesis, Department of Micro- and Nanotechnology, Technical University of Denmark, 8 2005. `http://www2.mic.dtu.dk/research/MIFTS/publications/PhD/PhDthesisMJJ.pdf`.

[23] Bo Jin, Andreas Acrivos, and Andreas Münch. The drag-out problem in film coating. *Physics of Fluids*, 17:103603, 2005.

[24] Dawn E. Kataoka and Sandra M. Troian. Stabilizing the advancing front of thermally driven climbing films. *Journal of Colloid and Interface Science*, 203: 335–344, 1998.

[25] L. D. Landau and E. M. Lifshitz. *Fluid Mechanics*. Butterworth–Heinemann, 1987.

[26] A. V. Larsen, J. Beech, V. Özkapici, B. Bilenberg, A. Kristensen, and J. O. Tegenfeldt. Pushing the limits of deterministic lateral displacement. In *10th International Conference on Miniaturized Systems for Chemistry and Life Sciences*, Tokyo, Japan, Nov. 5–9 MicroTAS 2006.

[27] Asger Vig Larsen. Deterministic bio-separation devices. MSc thesis, Department of Micro- and Nanotechnology, Technical University of Denmark, 11 2006. URL `www.mic.dtu.dk/Research/NSE/Optofluidics/Publications`.

[28] B. Lautrup. *Physics of continous matter: exotic and everyday phenomena in the macroscopic world*. Institute of Physics Publishing, 2005. ISBN 0750307528.

[29] Zhigang Li and German Drazer. Separation of suspended particles by arrays of obstacles in microfluidic devices. *Physical Review Letters*, 98(5):050602, 2007.

[30] Sylvie Lionti-Addad and Jean-Marc di Meglio. Stabilization of aqueous foam by hydrosoluble polymers. 1. sodium dodecyl sulfate-poly(ethylene oxide) system. *Langmuir*, 8:324–327, 1992.

[31] Brian R. Long, Martin Heller, Jason P. Beech, Heiner Linke, Henrik Bruus, and Jonas O. Tegenfeldt. Multidirectional sorting modes in deterministic lateral displacement devices. *Physical Review E*, 78:In press, 2008.

[32] J. Lyklema, P. C. Scholten, and K. J. Mysels. Flow in thin liquid films. *Journal of Physical Chemietry*, 69:116–123, 1964.

[33] MATLAB. `http://www.mathworks.com/`.

[34] Christian Mikkelsen and Henrik Bruus. Microfluidic capturing-dynamics of paramagnetic bead suspensions. *Lab on a Chip*, 5:1293–1297, 2005.

[35] Keith J Morton, Kevin Loutherback, David W Inglis, Ophelia K Tsui, James C Sturm, Stephen Y Chou, and Robert H Austin. Hydrodynamic metamaterials: Microfabricated arrays to steer, refract, and focus streams of biomaterials. *Proceedings of the National Academy of Sciences of the USA*, 105(21):7434, 2008.

[36] T Mårtensson, M Borgström, W Seifert, B J Ohlsson, and L Samuelson. Fabrication of individually seeded nanowire arrays by vapour-liquid-solid growth. *Nanotechnology*, 14(12):1255, 2003.

[37] Comsol Multiphysics. User's guide. Technical report, Comsol AB, 2005.

[38] Karol J. Mysels and Michael C. Cox. An experimental test of Frankel's law of film thickness. *Journal of colloid science*, 17:136–145, 1962.

[39] S. Naire, R. J. Braun, and S. A. Snow. A $2+1$ dimensional insoluble surfactant model for a vertical draining free film. *Journal of Computational and Applied Mathematics*, 166:385–410, 2004.

[40] MIFTS note. Eulerian, Lagrangian, or other reference frames. `www.mic.dtu.dk/microfluidics`.

[41] Laurits Højgaard Olesen. Computational fluid dynamics in microfluidic systems. MSc thesis, Department of Micro- and Nanotechnology, Technical University of Denmark, 7 2003. `http://www2.mic.dtu.dk/research/MIFTS/publications/MSc/MScLHO.pdf`.

[42] Laurits Højgaard Olesen, Fridolin Okkels, and Henrik Bruus. A high-level programming-language implementation of topology optimization applied to steady-state navier–stokes flow. *International Journal for Numerical Methods In Engineering*, 65:975–1001, 2006.

[43] Elin Olsson. Mass conserving simulations of two phase flow. Master's thesis, Department of Numerical Analysis and Computer Science, Royal Institute of Technology, 2006.

[44] Elin Olsson and Gunilla Kreiss. A conservative level set method for two phase flow. *Journal of Computational Physics*, 210:225–246, 2005.

[45] Elin Olsson, Gunilla Kreiss, and Sara Zahedi. A conservative level set method for two phase flow ii. *Journal of Computational Physics*, 225:785–807, 2007.

[46] Stanley Osher and Ronald Fedkiw. *Level Set Methods and Dynamic Implicit Surfaces*, volume 153 of *Applied mathematical sciences*. Springer, Springer-Verlag New York Inc., 1 edition, 2003. ISBN: 0-387-95482-1.

[47] Yashodhara Pawar and Kathleen J. Stebe. Marangoni effects on drop deformation in an extensional flow: The role of surfactant physical chemistry. i. insoluble surfactants. *Physics of Fluids*, 8:1738–1751, 1996.

[48] C. Pozrikidis. A finite-element method for interfacial surfactant transport, with application to the flow-induced deformation of a viscous drop. *Journal of Engineering Mathematics*, 49:163–180, 2004.

[49] P. Reimann. Brownian motors: noisy transport far from equilibrium. *Physics Reports*, 361(2-4):cp1–265, 2002.

[50] J. A. Sethian. *Level Set Methods and Fast Marching Methods*. Cambridge University Press, 2 edition, 1999. ISBN: 0-521-64557-3 paperback.

[51] Todd M. Squires and Stephen R. Quake. Microfluidics: Fluid physics at the nanoliter scale. *reviews of Modern Physics*, 77:977–1026, 2005.

[52] H. A. Stone. A simple derivation of the time-dependent convective-diffusion equation for surfactant transport along a deforming interface. *Physics of Fluids A*, 2:111–112, 1990.

[53] Patrick Tabeling. *Introduction to Microfluidics*. OUP Oxford, 2005.

[54] The Auguste Biomaterials Lab. School of Engineering and Applied Sciences, Harvard University. `http://www.seas.harvard.edu/biomat/`.

[55] Theoretical Microfluidics research group. Department of Micro and Nanotechnology, Technical University of Denmark. `http://www.nanotech.dtu.dk/microfluidics`.

[56] Ernst A. van Nierop, Benoit Scheid, and Howard A. Stone. On the thickness of soap films: An alternative to frankel's law. *Journal of Fluid Mechanics*, 602: 119, 2008.

[57] Siyang Zheng, Raylene Yung, Yu-Chong Tai, and Harvey Kasdan. Deterministic lateral displacement MEMS device for continuous blood cell separation. In *18th IEEE International Conference on Micro Electro Mechanical Systems*, pages 851–854, Miami, USA, 30 Jan.-3 Feb. 2005 2005.

[58] William B. J. Zimmerman. *Multiphysics Modelling with Finite Element Methods*. World Scientific, 2006.

A. Comsol code

A.1. Verification: viscus ellipse

Comsol script used to verify the ALE implementation and the surface tension condition at the free boundary.

```
clear

%% Constants and expressions
fem.const = {'Re','0.1','Ca','1','b','0.5','a','1/b'};

fem.expr = { ...
    'sigmaxx','-p+2*ux', ...
    'sigmaxy','vx+uy', ...
    'sigmayx','sigmaxy', ...
    'sigmayy','(-p+2*vy)', ...
    'xt','xTIME','xtt','xTIMETIME',...
    'xXt','xXTIME','xYt','xYTIME',...
    'yt','yTIME','ytt','yTIMETIME',...
    'yXt','yXTIME','yYt','yYTIME',...
    'ut','uTIME-xTIME*ux-yTIME*uy',...
    'utt','uTIMETIME',...
    'uxt','uxTIME-xTIME*uxx-yTIME*uxy',...
    'uyt','uyTIME-xTIME*uyx-yTIME*uyy',...
    'vt','vTIME-xTIME*vx-yTIME*vy',...
    'vtt','vTIMETIME',...
    'vxt','vxTIME-xTIME*vxx-yTIME*vxy',...
    'vyt','vyTIME-xTIME*vyx-yTIME*vyy',...
    'pt','pTIME-xTIME*px-yTIME*py',...
    'ptt','pTIMETIME',...
    'pxt','pxTIME-xTIME*pxx-yTIME*pxy',...
    'pyt','pyTIME-xTIME*pyx-yTIME*pyy'};

%% Geometry and mesh
fem.geom = ellip2('a','b','const',fem.const);
fem.mesh = meshinit(fem,'hauto',3);


```

```
%% Frame specifications
fem.frame = {'ref','ale'};
fem.sdim = {{'X','Y'},{'x','y'}};
fem.meshtime = 'TIME';

clear sshape
sshape.dvolname = 'dvol';
sshape.frame = 'ref';
sshape.sorder = 2;
sshape.type = 'fixed';
fem.sshape{1} = sshape;

clear sshape
sshape.dvolname = 'dvol_ale';
sshape.frame = 'ale';
sshape.sorder = 2;
sshape.type = 'moving_abs';
sshape.refframe = 'ref';
fem.sshape{2} = sshape;

fem.gporder = {4,2,30};
fem.cporder = {2,1};
clear sshape

%% Shape functions
fem.shape = { ...
    'shlag(''order'',2,''basename'',''x'',''frame'',''ref'')', ...
    'shlag(''order'',2,''basename'',''y'',''frame'',''ref'')', ...
    'shlag(''order'',2,''basename'',''u'',''frame'',''ale'')', ...
    'shlag(''order'',2,''basename'',''v'',''frame'',''ale'')', ...
    'shlag(''order'',1,''basename'',''p'',''frame'',''ale'')', ...
    'shlag(''order'',2,''basename'',''lm'',''frame'',''ref'')'};

%% Equation form
fem.form = 'weak';
fem.solform = 'weak';

% Subdomain settings
fem.equ.ind = [1];
fem.equ.dim = {'x','y','u','v','p'};
fem.equ.shape = [1:5];
fem.equ.cporder = {{1;1;1;1;2}};
fem.equ.gporder = {{1;1;1;1;2}};
fem.equ.sshapedim = {{1;1;2;2;2}};
```

```
77  fem.equ.init = {{'X';'Y';0;0;0}};
78  fem.equ.dweak = {{0;0;'Re*ut*test(u)';'Re*vt*test(v)';0}};
79  fem.equ.weak = {{ ...
80      'xXt*test(xX)+xYt*test(xY)'; ...
81      'yXt*test(yX)+yYt*test(yY)'; ...
82      '-(sigmaxx*test(ux)+sigmaxy*test(uy))-Re*(u*ux+v*uy)*test(u)'; ...
83      '-(sigmayx*test(vx)+sigmayy*test(vy))-Re*(u*vx+v*vy)*test(v)'; ...
84      '(ux+vy)*test(p)'}};
85
86  % Boundary settings
87  fem.bnd.ind = {[1:4]};
88  fem.bnd.dim = {'x','y','u','v','p','lm'};
89  fem.bnd.shape = {[1:6]};
90  fem.bnd.sshapedim = {{1;1;2;2;2;1}};
91  fem.bnd.weak = { ...
92      {'test(x*nx)*lm';'test(y*ny)*lm'; ...
93      '-1/Ca*test(uTx)';'-1/Ca*test(vTy)'; ...
94      '0';'test(lm)*(nx*(u-xt)+ny*(v-yt))'}};
95
96  %% Solve problem
97  fem.xmesh = meshextend(fem);
98  fem.sol = femtime(fem, ...
99      'solcomp',{'u','v','p','x','y','lm'}, ...
100     'outcomp',{'u','v','p','x','y','lm'}, ...
101     'tlist',[0:0.1:15],'initialstep',1e-6);
```

A.2. Script for modeling film drawing

Comsol script for modeling the drawing of a liquid film from a bath of Newtonian liquid. The script includes the effects of surface tension and Marangoni stress.

```
clear

Bo = 1e-4;
Ca = 1e-2;

%% Geometry
const.w = 10e-6;
const.lc = 1/sqrt(Bo)*const.w;
xscale = const.w; yscale = const.w;

[geom,boundary,point] = static_geometry(const.lc,const.w,xscale,yscale);
fem.geom = geom;

%% Constants and expressions
fem.const = { ...
  'Re','0', ...
  'Bo',Bo, ...
  'Ca',Ca, ...
  'stopminqual',0.1, ...
  'stopthickness',0.008};

% Change gamma to 1 for no Marangoni stress
fem.expr = { ...
  'gamma','min(1+0.05/200*(y),1.05)', ...
  'sigmaxx','-p+2*ux', ...
  'sigmaxy','vx+uy', ...
  'sigmayx','sigmaxy', ...
  'sigmayy','-p+2*vy', ...
  'xt','xTIME','xtt','xTIMETIME', ...
  'xXmt','xXmTIME','xYmt','xYmTIME', ...
  'yt','yTIME','ytt','yTIMETIME', ...
  'yXmt','yXmTIME','yYmt','yYmTIME', ...
  'ut','uTIME-xTIME*ux-yTIME*uy', ...
  'utt','uTIMETIME', ...
  'uxt','uxTIME-xTIME*uxx-yTIME*uxy', ...
  'uyt','uyTIME-xTIME*uyx-yTIME*uyy', ...
  'vt','vTIME-xTIME*vx-yTIME*vy', ...
  'vtt','vTIMETIME', ...
  'vxt','vxTIME-xTIME*vxx-yTIME*vxy', ...
  'vyt','vyTIME-xTIME*vyx-yTIME*vyy', ...
```

```
  'pt','pTIME-xTIME*px-yTIME*py', ...
  'ptt','pTIMETIME', ...
  'pxt','pxTIME-xTIME*pxx-yTIME*pxy', ...
  'pyt','pyTIME-xTIME*pyx-yTIME*pyy', ...
  'xinit_ale','Xm','yinit_ale','Ym'};

%% Frame specifications
fem.frame = {'mesh','ref','ale'};
fem.sdim = {{'Xm','Ym'},{'X','Y'},{'x','y'}};
fem.meshtime = 'TIME';

clear sshape
sshape.dvolname = 'dvol';
sshape.frame = 'mesh';
sshape.sorder = 2;
sshape.type = 'fixed';
fem.sshape{1} = sshape;
clear sshape
sshape.dvolname = 'dvol_ale';
sshape.frame = 'ale';
sshape.sorder = 2;
sshape.type = 'moving_abs';
sshape.refframe = 'mesh';
fem.sshape{2} = sshape;
clear sshape
sshape.dvolname = 'dvol_ref';
sshape.frame = 'ref';
sshape.sorder = 2;
sshape.type = 'moving_abs';
sshape.refframe = 'mesh';
fem.sshape{3} = sshape;
clear sshape

fem.gporder = {4,30,2};
fem.cporder = {2,1};

%% Shape functions
fem.shape = { ...
    'shlag(2,''x'')', ...
    'shlag(2,''y'')', ...
    'shlag(''order'',2,''basename'',''u'',''frame'',''ale'')', ...
    'shlag(''order'',2,''basename'',''v'',''frame'',''ale'')', ...
    'shlag(''order'',1,''basename'',''p'',''frame'',''ale'')', ...
    'shlag(2,''X'')', ...
```

```
85      'shlag(2,''Y'')', ...
86      'shlag(2,''lm1'')', ...
87      'shlag(2,''lm2'')', ...
88      'shlag(2,''lm3'')', ...
89      'shlag(2,''lm4'')', ...
90      'shlag(2,''lm5'')'};
91
92  %% Equation form
93  fem.form = 'weak';
94  fem.solform = 'weak';
95
96  %% Subdomain settings
97  fem.equ.ind = [1];
98  fem.equ.dim = {'x','y','u','v','p'};
99  fem.equ.shape = [1:7];
100 fem.equ.cporder = {{1;1;1;1;2}};
101 fem.equ.gporder = {{1;1;1;1;3}};
102 fem.equ.sshapedim = {{1;1;2;2;2}};
103 fem.equ.init = {{'Xm';'Ym';0;0;0}};
104 fem.equ.dweak = {{0;0;'Re*ut*test(u)';'Re*vt*test(v)'}};
105 fem.equ.weak = {{ ...
106     'xXmt*test(xXm)+xYmt*test(xYm)'; ...
107     'yXmt*test(yXm)+yYmt*test(yYm)'; ...
108     '-(sigmaxx*test(ux)+sigmaxy*test(uy))-Re*(u*ux+v*uy)*test(u)'; ...
109     '-(sigmayx*test(vx)+sigmayy*test(vy))-Re*(u*vx+v*vy)*test(v)-Bo/Ca*test(
            v)'; ...
110     '(ux+vy)*test(p)'}};
111
112 %% Boundary settings
113 fem.bnd.ind = { ...
114     [boundary.symmetry] ...
115     [boundary.bottom] ...
116     [boundary.piston] ...
117     [boundary.right] ...
118     [boundary.free]};
119 fem.bnd.dim = {'x','y','u','v','p','lm1','lm2','lm3','lm4','lm5'};
120 fem.bnd.shape = { ...
121     [1:8,10],[1:9],[1:11],[1:8],[1:7,12]};
122 fem.bnd.sshapedim = {{1;1;2;2;2;1;1;2;2;1}};
123 fem.bnd.cporder = {{1;1;1;1;2;1;1;1;1;1}};
124 fem.bnd.gporder = {{1;1;1;1;3;1;1;2;2;2}};
125
126 fem.bnd.weak = {...
127     {'test(x)*lm1+test(lm1)*(x-X)';0;'test(u)*lm3-test(lm3)*(u)'}, ...
```

```
128     {'test(x)*lm1+test(lm1)*(x-X)';'test(y)*lm2+test(lm2)*(y-Y)';'-nx*p_hyd*
            test(u)';'-ny*p_hyd*test(v)'}, ...
129     {'test(x)*lm1+test(lm1)*xt';'test(y)*lm2+test(lm2)*(yt-1)';'test(u)*lm3+
            test(lm3)*u';'test(v)*lm4+test(lm4)*(v-1)'}, ...
130     {'test(x)*lm1+test(lm1)*(x-X)';0;'-nx*p_hyd*test(u)';'-ny*p_hyd*test(v)'
            }, ...
131     {'test(x*nx)*lm5';'test(y*ny)*lm5';'-1/Ca*gamma*test(uTx)';'-1/Ca*gamma*
            test(vTy)';0;0;0;0;0;'test(lm5)*(nx*(u-xt)+ny*(v-yt))'}};
132
133 fem.bnd.expr = { ...
134     'kappa',{'' '' '' '' 'Ca*(nx^2*sigmaxx+ny^2*sigmayy+2*nx*ny*sigmaxy)'},
            ...
135     'p_hyd','-y*Bo/Ca'};
136
137 %% Point settings
138 fem.pnt.ind = {[point.other] [point.piston] [point.right]};
139 fem.pnt.dim = {'x','y','u','v','p','lm5'};
140 fem.pnt.shape = {[1:7],[1:7,12],[1:7,12]};
141 fem.pnt.sshapedim = {{1;1;2;2;2;1}};
142 fem.pnt.constrf = {0,'test(lm5)','test(lm5)'};
143 fem.pnt.constr = {0,'lm5','lm5'};
144 fem.pnt.weak = {0, ...
145     {0;0;'test(u)*1/Ca*gamma*Tx1';'test(v)*1/Ca*gamma*Ty1'}, ...
146     {0;0;'test(u)*1/Ca*gamma*Tx2';'test(v)*1/Ca*gamma*Ty2'}};
147
148 %% Elem for remeshing purposes
149 clear el gd;
150 el.elem = 'elvar';
151 el.g = {'1'};
152 gd_pnt.ind = {cellstr(num2str([1:flgeomnv(fem.geom)]','%d'))'};
153 gd_pnt.var = {'X',{'xinit_ale'},'Y',{'yinit_ale'}};
154 gd_bnd.ind = {cellstr(num2str([1:flgeomnbs(fem.geom)]','%d'))'};
155 gd_bnd.var = {'X',{'xinit_ale'},'Y',{'yinit_ale'}};
156 gd_sub.ind = {{'1'}};
157 gd_sub.var = {'X',{'xinit_ale'},'Y',{'yinit_ale'}};
158 el.geomdim{1} = {gd_pnt,gd_bnd,gd_sub};
159 fem.eleminit{1} = el;
160 clear el gd
161
162
163 % Use the value of the normal vector at the endpoints of the
164 % free boundary to define the tangent vector at the contact points.
165 % The tangent is (Tx,Ty) = (ny,-nx)
166 clear elem elemcpl
```

```
elem.elem = 'elcplextr';
elem.g = {'1'};
src = cell(1,1);
clear bnd
bnd.expr = { ...
    {'ny',{}},{'-nx',{}}, ...
    {{},'ny'},{{},'-nx'}};
bnd.map = { ...
    {'1',{}},{'1',{}}, ...
    {{},'1'},{{},'1'}};
bnd.ind = {{num2str(boundary.free(1))},{num2str(boundary.free(end))}};
src{1} = {{},bnd,{}};
elem.src = src;
geomdim = cell(1,1);
clear pnt
pnt.map = { ...
    {'2','3'},{'2','3'}, ...
    {{},'3'},{{},'3'}};
pnt.ind = {{num2str(point.piston)},{num2str(point.right)}};
geomdim{1} = {pnt,{},{}};
elem.geomdim = geomdim;
elem.var = {'Tx1','Ty1','Tx2','Ty2'};
map = cell(1,3);

clear submap
submap.type = 'local';
submap.expr = {'s'};
map{1} = submap;

clear submap
submap.type = 'local';
submap.expr = {'0'};
map{2} = submap;

clear submap
submap.type = 'local';
submap.expr = {'1'};
map{3} = submap;

elem.map = map;
elemcpl{1} = elem;
fem.elem = {elem};
clear elem elemcpl submap bnd pnt src map geomdim

```

```
211 %% Minimum mesh quality
212 clear el vol elem
213 el.elem = 'elcplscalar';
214 el.g = {'1'};
215 el.geomdim ={{}};
216 el.var = {'minqual_neg'};
217 el.global = {'1'};
218 el.maxvars = {'1'};
219 vol.expr = {'-qual_ale'};
220 vol.ipoints = {'4'};
221 vol.ind = '1';
222 el.src{1} = {{},{},vol};
223 fem.elem = [fem.elem {el}];
224 clear el vol
225
226 clear el;
227 el.elem = 'elconst';
228 el.var = {'minqual' '-minqual_neg'};
229 fem.elem = [fem.elem {el}];
230
231 %% Film thickness
232 clear el;
233 el.elem = 'elcplscalar';
234 el.g = {'1'};
235 el.var = {'thk'};
236 el.global = {'1'};
237 el.maxvars = {'1'};
238
239 clear src;
240 src.ind = {cellstr(num2str([boundary.free]','%d'))'};
241 src.expr = {{'-x'}};
242 src.iorders = {{'4'}};
243 el.src{1} = {{},src,{}};
244
245 clear dst;
246 dst.ind = {{'1'}};
247 dst.usage = {{'1'}};
248 el.geomdim{1} = {{},{},dst};
249 fem.elem = [fem.elem {el}];
250
251 clear el;
252 el.elem = 'elconst';
253 el.var = {'thickness' '-thk'};
254 fem.elem = [fem.elem {el}];
```

```
255
256 thickness=1;
257 iter = 0;
258
259 %% Solve problem. Remesh if mesh is too distorted
260 while thickness >= 0.01,
261     linsolver='pardiso';
262     iter = iter +1;
263
264     if iter > 1,
265         % Geometry
266         % Generate geom from mesh
267         fem = mesh2geom(fem, ...
268             'frame','ale', ...
269             'solnum',length(fem0.sol.tlist), ...
270             'srcdata','deformed', ...
271             'destfield',{'geom','mesh'}, ...
272             'srcfem',1, ...
273             'destfem',1);
274     end
275
276     % Initialize mesh
277     fem.mesh=meshinit(fem,'hnarrow',5,'hauto',3);
278
279     % Extend mesh
280     fem.xmesh=meshextend(fem);
281
282     if iter == 1,
283         init = asseminit(fem);
284         fem.sol.tlist = 0;
285     elseif iter > 1,
286         % Mapping current solution to extended mesh
287         init = asseminit(fem, ...
288             'init',fem0.sol, ...
289             'xmesh',fem0.xmesh, ...
290             'matherr','on', ...
291             'framesrc','ale', ...
292             'domwise','on');
293     end
294
295     if iter==3,break,end
296
297     % Solve problem
298     tic
```

```
299     fem.sol=femtime(fem, ...
300         'init',init, ...
301         'solcomp',{'x','y','u','v','p','lm1','lm2','lm3','lm4','lm5'}, ...
302         'outcomp',{'X','Y','x','y','u','v','p','lm1','lm2','lm3','lm4','lm5'
                }, ...
303         'tlist',[0:1:200]+fem.sol.tlist(end), ...
304         'tout','tlist', ...
305         'tsteps','free', ...
306         'linsolver',linsolver, ...
307         'plotglobal',{'thickness'}, ...
308         'stopcond','min(thickness-stopthickness,(minqual-stopminqual))');
309     toc
310
311
312     fem0=fem;
313     xfems{iter}=fem;
314
315     % Break if a solution cannot be found
316     if length(fem.sol.tlist)==1,
317         break
318     end
319
320 end
```

A.2.1. Helper functions

```
1  function [hh,xx] = static_meniscus(varargin)
2  % Helper function to generate the initial geometry.
3
4  if nargin==0,
5      disp('No input arguments?')
6      lc = 1.7e-3;
7  else
8      lc = varargin{1};
9      hstop = varargin{2};
10 end
11
12 xspan = linspace(sqrt(2)*lc,0,30);
13 init = [0,0];
14 options = odeset('Events',@events);
15 [x,H,xe,he,ie] = ode45(@calc_meniscus,xspan,init,options);
16 hh = H(:,1);
17 xx = x;
```

```
18
19      function dH = calc_meniscus(x,H)
20          hx = H(2);
21          dH = zeros(2,1);
22          dH(1) = hx;
23          dH(2) = x/(lc^2) * (1+hx^2)^(3/2);
24      end
25
26      function [value,isterminal,direction] = events(x,h)
27          % Locate the time when height passes through zero in a
28          % decreasing direction and stop integration.
29          value = h(1)-hstop; % Detect height = 0
30          isterminal = 1; % Stop the integration
31          direction = 0; % Negative direction only
32      end
33  end
```

```
1   function [g,boundary,point] = static_geometry(lc,w,varargin);
2   % Generate initial geometry for film drawing.
3   % Output geometrym and boundary and point numbers.
4
5   if nargin==2,
6       xscale = w;
7       yscale = w;
8   elseif nargin == 3;
9       xscale = varargin;
10      yscale = xscale;
11  elseif nargin == 4;
12      xscale = varargin{1};
13      yscale = varargin{2};
14  else
15      error('(static_geometry.m) The scale arguments are messed up.')
16  end
17  W = 40;
18  [h,x] = static_meniscus(lc,(W-1)*xscale);
19  H = (h+w)/xscale;
20  X = x/yscale;
21
22  p = [H';X'];
23  symmetry = curve2([0,0],[0,sqrt(2)*lc/yscale]);
24  piston = curve2([0,1],[sqrt(2)*lc/yscale,sqrt(2)*lc/yscale]);
25  free = geomspline(p);
26  right = curve2([W, W], [p(2,end),0]);
27  bottom = curve2([0, W],[0, 0]);
```

```
28
29 [g,ctx,ptx] = geomcoerce('solid',{symmetry,piston,free,right,bottom},'Out',{
       'ctx','ptx'});
30 %% boundary numbers
31 [i,j] = find(ctx{1}); boundary.symmetry = i';
32 [i,j] = find(ctx{2}); boundary.piston = i';
33 [i,j] = find(ctx{3}); boundary.free = i';
34 [i,j] = find(ctx{4}); boundary.right = i';
35 [i,j] = find(ctx{5}); boundary.bottom = i';
36
37 %% point numbers
38 points = 1:flgeomnv(g);
39 % end point for piston
40 [i,j] = find(ptx{2}); point.piston = i(2);
41 % top point for right boundary
42 [i,j] = find(ptx{4}); point.right = i(1);
43 point.other = points(points~=point.piston&points~=point.right);
44
45 %% plot geometry
46 % geomplot(g,'submode','off','edgelabels','on','pointlabels','on');
```

A.3. Implementation of convection–diffusion equation at a boundary

Comsol script for solving a convection-diffusion equation at a free boundary.

```
% create geometry
fem.geom = rect2(10,1);
fem.mesh = meshinit(fem,'hauto',3);

% constants and expressions
fem.const = {'Pe',100,'delta',0.35};
fem.expr = {'u','y','v','0'};

% setup equation system
fem.sdim = {'x','y'};
fem.bnd.dim = {'c'};
fem.shape = {'shlag(2,''c'')'};
fem.form = 'weak';
fem.bnd.ind = {[3],[1,2,4]};
fem.bnd.shape = {[1],[0]};
fem.bnd.dweak = {'test(c)*ct',0};
fem.bnd.weak = {'test(cTx)*(c*u-1/Pe*cTx)+ ...
                 test(cTy)*(c*v-1/Pe*cTy)',0};
fem.bnd.init = {{1},{0}};

% solve problem
fem.xmesh = meshextend(fem);
fem.sol = femtime(fem,'tlist',[0:0.1:10]);

% plot solution
postcrossplot(fem,1,[3], ...
    'lindata','c', ...
    'linxdata','x', ...
    'cont','on', ...
    'refine',1, ...
    'T',[0,0.1,1,10]);
```

A.4. Particle probability distribution in a unit cell

Comsol script for finding the reduced particle probability in a unit cell of a deterministic lateral displacement device.

```
M = 3;
N = 10;
br = 0;
a = 0.4;

flclear fem fem0 xfem

% Constants
xfem.const = {...
  'rho0','1e3', ...
  'eta0','1e-3', ...
  'kB','1.23e-23', ...
  'T','300', ...
  'a',a, ...
  'L','10e-6', ...
  'Re','rho0*u0*L/eta0', ...
  'D','kB*T/(6*pi*eta0*a*L)', ...
  'Pe','L*u0/D'};

% Global expressions
xfem.globalexpr = { ...
  'C','c/ctot', ...
  'tan_theta','J_y/J_x', ...
  'theta','atan2(J_y,J_x)*180/pi', ...
  'tan_theta_flow','U_y/U_x', ...
  'theta_flow','atan2(U_y,U_x)*180/pi'};

%% The flow problem
flclear fem

% Geometry
fem.geom = geomcoerce('solid', ...
    {rect2(1,1,'pos',[0;0],'base','center'), ...
     point2(-0.5,-0.5+M/N), ...
     point2(+0.5,+0.5-M/N), ...
     point2(0,0)});

% Mesh
fem.mesh=meshinit(fem,'hauto',2);

```

```
fem.form = 'general';
fem.frame = {'ref'};
fem.sdim = {'x','y'};
fem.shape = {'sharg_2_5(''psi'')'};
fem.gporder = {[8] [4]};
% fem.cporder = 2;

% Subdomain settings
fem.equ.ind = [1];
fem.equ.dim = {'u','v'};
fem.equ.expr = {...
  'u','psiy','ux','psiyx','uy','psiyy', ...
  'v','-psix','vx','-psixx','vy','-psixy'};
fem.equ.ga = {{{'2*ux';'uy+vx'};{'uy+vx';'2*vy'}}};
fem.equ.f = {{'0';'0'}};
%fem.equ.f = {{'(u*ux+v*uy)*0';'(u*vx+v*vy)*0'}};

% Boundary settings
fem.bnd.ind = {[1] [3] [4]};
fem.bnd.dim = {'u','v'};
fem.bnd.expr = {'u','psiy','v','-psix'};
fem.bnd.constr = {...
    {'u_out2-u' 'v_out2-v'}, ...
    {'u_out1-u' 'v_out1-v'}, ...
    {'u_bot-u' 'v_bot-v'}};

% Point settings
fem.pnt.ind = {[2,6] [1,5] [3,7] [4]};
fem.pnt.constr = {0,'psi','1-psi',{'psiy';'-psix'}};
fem.pnt.constrf = {0,'test(psi)','test(psi)',{'test(psiy)';'test(psix)'}};

fem = femdiff(fem);

% Coupling variables
clear elemcpl elem
elem.elem = 'elcplextr';
elem.g = {'1','2'};
src = cell(1,2);
clear bnd
bnd.expr = { ...
    {'u',{},{}}, ...
    {'v',{},{}}, ...
    {{},'u',{}}, ...
    {{},'v',{}}, ...
```

```
85      {{},{},'u'}, ...
86      {{},{},'v'}, ...
87      {},{}};
88  bnd.map = { ...
89      {'1','1','1'}, ...
90      {'1','1','1'}, ...
91      {'1','1','1'}, ...
92      {'1','1','1'}, ...
93      {'1','1','1'}, ...
94      {'1','1','1'}, ...
95      {},{}};
96  bnd.ind = {{'2'},{'5'},{'6'}};
97  clear equ
98  equ.expr = {{},{},{},{},{},{},{'u'},{'v'}};
99  equ.map = {{},{},{},{},{},{},{'2'},{'2'}};
100 equ.ind = {{'1'}};
101 src{1} = {{},bnd,equ};
102 src{2} = {};
103 elem.src = src;
104 geomdim = cell(1,2);
105
106 clear bnd
107 bnd.map = {...
108     {{},{},'3'}, ...
109     {{},{},'3'}, ...
110     {{},'4',{}}, ...
111     {{},'4',{}}, ...
112     {'5',{},{}}, ...
113     {'5',{},{}}, ...
114     {},{}};
115 bnd.ind = {{'1'},{'3'},{'4'}};
116 geomdim{1} = {{},bnd,{}};
117
118 clear equ
119 equ.map = {{},{},{},{},{},{},{'2',{}},{'2',{}}};
120 equ.ind = {{'1'},{'2'}};
121 geomdim{2} = {{},{},equ};
122 elem.geomdim = geomdim;
123 elem.var = {'u_bot','v_bot','u_out1','v_out1','u_out2','v_out2','u','v'};
124
125 map = cell(1,5);
126 clear submap
127 submap.type = 'unit';
128 map{1} = submap;
```

```
129
130 clear submap
131 submap.type = 'local';
132 submap.expr = {'x','y'};
133 map{2} = submap;
134
135 clear submap
136 submap.type = 'linear';
137 submap.sg = '1';
138 submap.sv = {'3','7'};
139 submap.dg = '1';
140 submap.dv = {'1','5'};
141 map{3} = submap;
142
143 clear submap
144 submap.type = 'linear';
145 submap.sg = '1';
146 submap.sv = {'2','3'};
147 submap.dg = '1';
148 submap.dv = {'5','6'};
149 map{4} = submap;
150
151 clear submap
152 submap.type = 'linear';
153 submap.sg = '1';
154 submap.sv = {'1','2'};
155 submap.dg = '1';
156 submap.dv = {'6','7'};
157 map{5} = submap;
158
159 elem.map = map;
160 elemcpl{1} = elem;
161
162 fem.elemcpl = elemcpl;
163
164 xfem.fem{1} = fem;
165
166
167 %% The particle distribution problem
168 flclear fem
169
170 % Geometry
171 fem.geom = geomcoerce('solid', ...
172     {rect2(1,1,'pos',[0;0],'base','center'), ...
```

```
173      point2(-0.5,-0.5+M/N), ...
174      point2(+0.5,+0.5-M/N), ...
175      circ2(a+br)});
176
177  % Mesh
178  fem.mesh = meshbndlayer(fem,'blbnd',[7:10],'blnlayers',{[7:10],10},'hauto'
         ,2);
179
180  fem.sdim = {'x','y'};
181  fem.frame = {'ref'};
182  fem.shape = {'shlag(2,''c'')'};
183
184  fem.form = 'general';
185
186  % Subdomain settings
187  fem.equ.ind = {[1] [2]};
188  fem.equ.dim = {'c'};
189  fem.equ.ga = {{{'c*u-1/Pe*cx';'c*v-1/Pe*cy'}};{{'0';'0'}}}; % ;{{'0';'0'}}
190  fem.equ.f = 0;
191  fem.equ.init = {'1/(1-a*a*pi)' 0};
192  fem.equ.shape = {[1] []};
193  fem.equ.sshape = 1;
194
195  % Boundary settings
196  fem.bnd.ind = {[1] [3] [4] [2,5,6] [7:10]};
197  fem.bnd.g = { ...
198      '-(nx*u+ny*v)*c+1/Pe*(nx*cx+ny*cy)' ...
199      '-(nx*u+ny*v)*c+1/Pe*(nx*cx+ny*cy)' ...
200      '-(nx*u+ny*v)*c+1/Pe*(nx*cx+ny*cy)' ...
201      '-(nx*u+ny*v)*c+1/Pe*(nx*cx+ny*cy)' ...
202      0};
203  fem.bnd.constr = {...
204      {'c_out2-c'}, ...
205      {'c_out1-c'}, ...
206      {'c_bot-c'}, ...
207      0 0};
208
209  fem = femdiff(fem);
210
211  % Coupling variables
212  clear elemcpl elem
213  elem.elem = 'elcplscalar';
214  elem.g = {'2'};
215  src = cell(1,1);
```

```
clear equ
equ.expr = {...
    {'c',{}}, ...
    {'(c*u-1/Pe*cx)/ctot',{}}, ...
    {'(c*v-1/Pe*cy)/ctot',{}}, ...
    {'u','u'}, ...
    {'v','v'}};
equ.ipoints = {{'4',{}},{'4',{}},{'4',{}},{'4','4'},{'4','4'}};
equ.frame = {{'ref',{}},{'ref',{}},{'ref',{}},{'ref','ref'},{'ref','ref'}};
equ.ind = {{'1'},{'2'}};
src{1} = {{},{},equ};
elem.src = src;
geomdim = cell(1,1);
geomdim{1} = {};
elem.geomdim = geomdim;
elem.var = {'ctot','J_x','J_y','U_x','U_y'};
elem.global = {'1','2','3','4','5'};
elem.maxvars = {};
elemcpl{1} = elem;

% Extrusion coupling variables
clear elem
elem.elem = 'elcplextr';
elem.g = {'2'};
src = cell(1,1);
clear bnd
bnd.expr = {{'c',{},{}},{{},'c',{}},{{},{},'c'}};
bnd.map = {{'1','1','1'},{'1','1','1'},{'1','1','1'}};
bnd.ind = {{'2'},{'5'},{'6'}};
src{1} = {{},bnd,{}};
elem.src = src;
geomdim = cell(1,1);

clear bnd
bnd.map = {{'2',{},{}},{{},'3',{}},{{},{},'4'}};
bnd.ind = {{'4'},{'3'},{'1'}};
geomdim{1} = {{},bnd,{}};
elem.geomdim = geomdim;
elem.var = {'c_bot','c_out1','c_out2'};
map = cell(1,4);

clear submap
submap.type = 'unit';
map{1} = submap;
```

```
260
261 clear submap
262 submap.type = 'linear';
263 submap.sg = '1';
264 submap.sv = {'3','10'};
265 submap.dg = '1';
266 submap.dv = {'1','8'};
267 map{2} = submap;
268
269 clear submap
270 submap.type = 'linear';
271 submap.sg = '1';
272 submap.sv = {'2','3'};
273 submap.dg = '1';
274 submap.dv = {'8','9'};
275 map{3} = submap;
276
277 clear submap
278 submap.type = 'linear';
279 submap.sg = '1';
280 submap.sv = {'1','2'};
281 submap.dg = '1';
282 submap.dv = {'9','10'};
283 map{4} = submap;
284
285 elem.map = map;
286 elemcpl{2} = elem;
287 fem.elemcpl = elemcpl;
288
289 xfem.fem{2} = fem;
290
291 %% Solve problem
292 xfem.solform = 'general';
293 xfem = multiphysics(xfem);
294 xfem.xmesh = meshextend(xfem,'geoms',[1,2]);
295
296 % Solve flow problem
297 xfem.sol=femstatic(xfem, ...
298                  'nullfun','flnullorth', ...
299                  'solcomp',{'psix','psiy','psi','psin','psixx','psixy','
                        psiyy'}, ...
300                  'outcomp',{'psix','psiy','c','psi','psin','psixx','psixy','
                        psiyy'});
301
```

```
302 % Save solution
303 fem0=xfem;
304
305 % Solve problem
306 xfem.sol=femstatic(xfem, ...
307                    'u',fem0.sol, ...
308                    'nullfun','flspnull', ...
309                    'solcomp',{'c'}, ...
310                    'outcomp',{'psix','psiy','c','psi','psin','psixx','psixy','
                           psiyy'}, ...
311                    'pname','u0', ...
312                    'plist',[[1 10 40 100 200].*1e-6]);
```

B. Papers

B.1. Paper published in Journal of Micromechanics and Microengineering

Title A theoretical analysis of the resolution due to diffusion and size dispersion of particles in deterministic lateral displacement devices.

Authors Martin Heller and Henrik Bruus.

Reference Published in J. Micromech. Microeng. **18** (2008).

J. Micromech. Microeng. **18** (2008) 075030 (6pp) doi:10.1088/0960-1317/18/7/075030

A theoretical analysis of the resolution due to diffusion and size dispersion of particles in deterministic lateral displacement devices

Martin Heller and Henrik Bruus

Department of Micro- and Nanotechnology, Technical University of Denmark, DTU Nanotech, Building 345 East, DK-2800 Kongens Lyngby, Denmark

E-mail: Martin.Heller@nanotech.dtu.dk and Henrik.Bruus@nanotech.dtu.dk

Received 28 January 2008, in final form 22 May 2008
Published 13 June 2008
Online at stacks.iop.org/JMM/18/075030

Abstract

We present a model including diffusion and particle-size dispersion for the separation of particles in deterministic lateral displacement devices also known as bumper arrays. We determine the upper critical diameter for diffusion-dominated motion and the lower critical diameter for pure convection-induced displacement. Application of our model to data suggests that the systematic deviation, observed for small particles in several experiments, from the critical diameter for separation given by simple laminar flow considerations may be explained by diffusion and size dispersion.

1. Introduction

In 2004, Huang *et al* [1] developed the elegant method of particle separation by deterministic lateral displacement in so-called microfluidic bumper arrays. The method, which relies on the laminar flow properties characteristic of microfluidcs, shows a great potential for fast and accurate separation of particles on the micrometer scale [1–4]. Among the key assets of the deterministic lateral displacement separation principle are that clogging can be avoided because particles much smaller than the feature size of the devices can be separated, that the devices are passive, i.e. the particles bump into solid obstacles or bumpers, and that the separation process is continuous.

More precisely, particle transport in microfluidic bumper arrays is primarily governed by convection due to the fluid flow and by displacement due to interaction with the bumpers in the array [1]. These processes are deterministic and the critical diameter for separation of relatively large particles in these devices is well understood in terms of the width of flow lanes bifurcating around the bumpers in the periodic arrays [3]. However, if bumper arrays and particles are scaled down, diffusion will influence the separation process and affect the critical particle size significantly. Previously reported data on separation of particles in bumper arrays all show a bias toward larger critical particle size than that given by the width of the flow lanes nearest to the bumpers of the array [1–3]. In this work we extend existing models by adding diffusion and taking particle-diameter dispersion into account, and thereby explain the observed discrepancy.

In bumper arrays particles are convected by the fluid flow through an array of bumpers placed in columns separated by the distance λ in the flow direction, see figure 1(*a*). For a given integer N, the array is made N-periodic in the flow direction by displacing the bumpers in a given column a distance λ/N perpendicular to the flow direction with respect to the bumper positions in the previous column. Due to this periodicity of the array and the laminarity of the flow, the stream can naturally be divided into N lanes, each carrying the same amount of fluid flux, and each having a specific path through the device, see [1].

For a given steady pressure drop, the fluid in the device moves with an average velocity u_0. Assuming a parabolic velocity profile $u(x)$ in the gap of width w_g between two neighboring bumpers, see figure 1(*b*),

$$u(x) = 6u_0 \frac{x}{w_g}\left(1 - \frac{x}{w_g}\right), \tag{1}$$

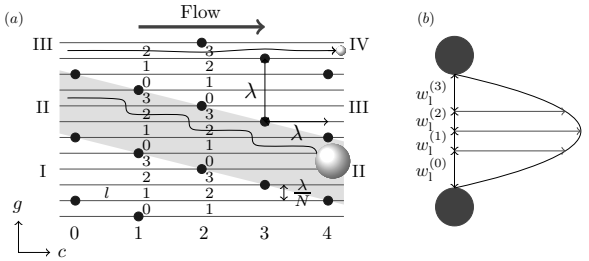

Figure 1. (*a*) An array of bumpers (black dots) with the definition of the lane number l (small arabic numbers), the column number c (large arabic numbers) and the gap number g (roman numbers). The shaded region illustrates how the shift in the position of gap II follows the geometry of the array. Large particles following the displacement path will therefore stay in the same gap number and lane number throughout the entire array as illustrated by the skew bumping trajectory of a large particle (large illuminated sphere). Small particles will not be displaced by the bumpers and will therefore visit all lane numbers as they follow the so-called zigzag path through an entire period of the array [1]. This is illustrated by the almost horizontal trajectory of a small particle in the upper flow lane (small illuminated sphere). (*b*) Close-up of a single gap between two bumpers (disks) in the array. Each of the four flow lanes carries the same flow rate. Due to the parabolic flow profile in the gap region, the width $w_1^{(l)}$ of the flow-lane l depends on its position in the gap.

the total flow rate Q_{tot} is given by

$$Q_{tot} = \int_0^{w_g} u(x)\,\mathrm{d}x = w_g u_0. \tag{2}$$

By numerical simulations at low Reynolds numbers relevant for the actual devices, $Re \approx 10^{-3} - 10^{-2}$, we find the assumption of a parabolic flow profile in the gap region well justified. This also agrees with the usual estimate for the entrance length $l_{entr} = 0.06Re\,w$, which is here of the order of 1 nm.

For an N-periodic array, the N flow lanes in a given gap carry the same flow rate Q_{tot}/N. The width $w_1^{(l)}$ of lane l is found by solving

$$\frac{Q_{tot}}{N} = \int_{x^{(l)}}^{x^{(l)}+w_1^{(l)}} u(x)\,\mathrm{d}x, \tag{3}$$

where $x^{(l)} = \sum_{j=0}^{l} w_1^{(j)}$ is the starting position of lane l. In the simple bifurcating flow-lane model [1, 3] the critical diameter d_c is given as $d_c/2 = w_1^{(1)}$. A small particle with $d < d_c$ will never leave its initial flow lane and will thus be convected in the general flow direction following a so-called zigzag path. The conventionally used name zigzag path refers to the case where the bumpers are large compared to their center-to-center distance. In this case the path, which appears almost straight in figure 1 given the smallness of the bumpers, becomes truly zigzag-shaped [1]. Large particles with $d > d_c$ will quickly bump against a bumper and from then on be forced by consecutive bumping to follow the skew direction of the array geometry, the so-called displacement path. When a particle gets bumped by a bumper in the array it will be displaced perpendicular to the flow direction until its center is located one particle radius $d/2$ from the surface of the bumper. This corresponds to n_l lanes of displacement,

$$n_l = \frac{N}{w_g u_0}\int_0^{d/2} u(x)\,\mathrm{d}x = N\frac{d^2}{4w_g^2}\left(3 - \frac{d}{w}\right). \tag{4}$$

In the bulk fluid, where the lanes are assumed to have equal width λ/N, see figure 1(*a*), the displaced distance ℓ_{disp} is therefore

$$\ell_{disp}(d) = n_l\frac{\lambda}{N} = \lambda\frac{d^2}{4w_g^2}\left(3 - \frac{d}{w_g}\right). \tag{5}$$

In this work we extend the simple bifurcating flow-lane model by including diffusion and particle-diameter dispersion.

2. Model including diffusion

During the average time $\tau = \lambda/u_0$ it takes a particle to move by convection from one column to the next, it also diffuses. We assume that the diffusion process perpendicular to the flow direction is normally distributed with mean value zero and variance

$$\sigma^2 = 2D\tau, \tag{6}$$

where the diffusivity D is given by the Stokes–Einstein expression

$$D = \frac{k_B T}{3\pi\eta d}. \tag{7}$$

Here k_B is Boltzmann's constant, T is the temperature and η is the viscosity of the fluid. Throughout the paper we use this expression to calculate D for any given particle size.

In figure 2 are sketched the two limits of (*a*) a small strongly diffusing particle, for which the interaction with the bumpers as well as the role of the flow lanes is negligible, and (*b*) a large particle, for which diffusion rarely brings the particle out of its given lane, and where each bumping event resets the position of the particle.

Note that we do not model Taylor–Aris dispersion explicitly. The reason is that this convection–diffusion phenomenon mainly affects the particle distribution along the flow direction [5]. However, we are not interested in the detailed arrival times of the particles in the outlet, only in their transverse distribution.

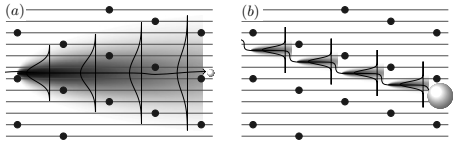

Figure 2. (*a*) The motion of very small particles is dominated by diffusion. Their distribution at the end of the array is therefore determined by their transverse diffusion during the time spent in the array. The intensity of the shaded region indicates the probability for finding the small particle at a given position in the array. A non-diffusive particle would follow the solid black trajectory straight through the array. (*b*) Large particles diffuse as well—but not very much—and every time they interact with a bumper their position in the gap is reset to the particle radius. Large particles therefore only have a slight probability of escaping the displacement path represented by the full black line. In both panels the Gaussian distribution of the diffusing particles is shown at four cross-sections.

2.1. Diffusion model

In order to escape bumping, a particle must diffuse more in the time interval τ than the difference $\ell_{\text{disp}} - \lambda/N$ between the bulk displacement and the shift in position of the next bumper. The probability p_{esc} for this to happen is given by the integral of the Gaussian tails (see figure 2) in the neighboring lanes, i.e., by the error function

$$p_{\text{esc}}(d) = \frac{1}{2} - \frac{1}{2}\,\text{erf}\left(\frac{\ell_{\text{disp}}(d) - \frac{1}{N}\lambda}{\sqrt{2}\sigma(d)}\right), \tag{8}$$

where we have introduced the d-dependence explicitly. When a particle is transported through a bumper array it must bump at every bumper within one period of the array in order to be displaced one gap at the outlet. Thus, if the particle escapes at least one time in N attempts, it will not be displaced. We define the critical particle size d_{c} to be the size for which half of the particles escape bumping as they pass one period of the array. Thus d_{c} can be found by solving

$$\sum_{k=1}^{N}\binom{N}{k} p_{\text{esc}}(d_{\text{c}})^k [1 - p_{\text{esc}}(d_{\text{c}})]^{N-k} = \frac{1}{2}. \tag{9}$$

In figure 3 we have plotted the result of our model calculation for the critical particle sizes as a function of the bumper period for parameter values corresponding to the bumper arrays used by Inglis *et al* [3] (full line), Huang *et al* [1] (dashed line) and Larsen [6] (dotted line). The corresponding measured data points from these papers are plotted as circular, square and triangular points, respectively.

It must be emphasized that although the authors of [3] in their text only describe bumper arrays with a relative column displacement $\varepsilon = 1/N$, they do plot, without comments, data points with other displacements, e.g., $\epsilon = 0.3$. These non-$1/N$ bumper arrays lead to more complicated displacement characteristics. This interesting topic, which we are currently studying, goes beyond the scope of the present work, where we focus on the influence of diffusion and particle-size distribution on the more simple and most widely used $1/N$-bumper arrays. In figure 3, we have therefore only plotted data points from [3] with $\epsilon = 1/N$.

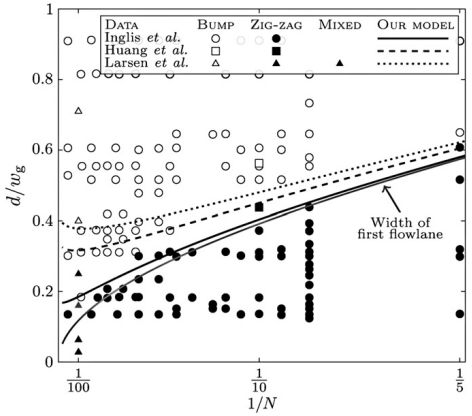

Figure 3. Our model applied to the experimental data of Inglis *et al* [3], Huang *et al* [1] and Larsen [6]. Particle diameter d over the gap width w_{g} is plotted as a function of the inverse period $1/N$. The full, dashed and dotted black lines show the theoretically predicted critical particle size for the bumper arrays used by Inglis *et al* [3] (only points with $\varepsilon = 1/N$), Huang *et al* [1] (only for $N = 10$) and Larsen [6] (only for $N = 100$), respectively. The experimental data points are representing particles following bumper paths (open symbols), zigzag paths (solid black symbols) and neither of these paths (solid gray symbols).

2.2. Comparison with experiments

The observation that the critical particle size in a $1/N$ bumper device is larger than the width of the first flow lane is also supported by the experimental data in figure 2 of [3]. Our model suggests that the deviation of the critical particle size from the width of the first flow lane can be explained by diffusion of the particles. In figure 3 it is seen how well the theoretical lines predict the transition between zigzag paths and displacement paths: the full line divides open and closed circles, the dashed line divides open and closed squares, and the dotted line divides open and closed triangles.

Using parameter values corresponding to the bumper device presented by Huang *et al* [1] our model predicts a critical particle diameter of 0.45 times the width of the gap for the particles traveling through the device with an average velocity of 400 μm s^{-1}. This is in good agreement with figure 2(*a*) in [1].

3. A discrete model including diffusion and dispersion

Particles typically used in experiments on particle separation are not mono-disperse. Their average diameters are distributed around a certain mean value with a relative standard deviation $\Delta d/d$, which typically is 20%, 10% and 5% for particles with $d = 25$ nm, $d = 100$ nm and $d = 500$ nm, respectively.

Faced with such a size dispersion it is very useful to have a simple method for predicting its effect. In the following

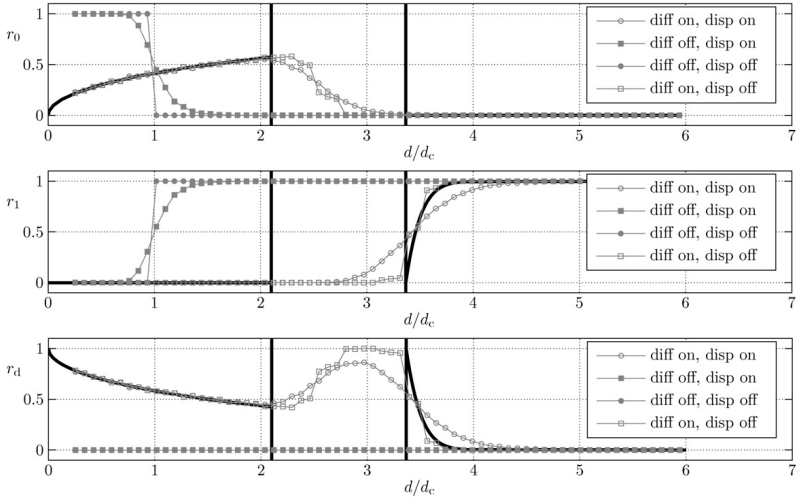

Figure 4. Relative numbers r_0, r_1 and r_{d} of particles following the zigzag path, the displacement path and neither of these two paths, respectively, plotted as a function of the normalized, average particle diameter d/d_{c}, where $d_{\text{c}} = 118$ nm. The parameters of the bumper array are taken from [6]: $N = 100$, $\lambda = 8$ μm, $w_{\text{g}} = 1$ μm, $L = 20N\lambda = 16$ mm and $u_0 = 250$ μm s^{-1}. The buffer liquid is water at room temperature. Neglecting diffusion (solid symbols), the particles follow the zigzag path if $d < d_{\text{c}}$ and the displacement path if $d > d_{\text{c}}$. Including diffusion (open symbols), with D given by equation (7), the small particles are not influenced by the bumpers. For $d > 2.1d_{\text{c}}$ the influence of the bumpers sets in, and for $d > 3.4d_{\text{c}}$ the particles follow the displacement path. The full black curves are the predictions using the results in sections 3.4.1 and 3.4.2, while the thick black vertical lines indicate the particle size when small particles stop behaving purely diffusive (left-most lines) and when large particles begin a purely deterministic displacement (right-most lines).

we therefore introduce a discrete model of the transport of particles with different diameters d in an N-periodic bumper array taking convection, diffusion and size dispersion into account. The model allows us to study the relative influence of all three phenomena on the separation efficiency in a fast and simple manner. We illustrate our model by using the specific parameters from the bumper device presented in [6], see figure 4. In particular our results suggest that the critical size for separation or displacement, studied above, must be supplemented by a smaller critical size below which pure diffusion governs the motion of the particles in the bumper array. This prediction has not yet been tested experimentally.

3.1. Definition of the discrete model

At any instant, a particle is assumed to be positioned in the center of a flow lane l of gap g in some column c of the array. For simplicity we further assume that the size distribution of any given set of particles is a normal distribution with a mean value given by the size quoted by the manufacturer and a relative standard deviation of 10%.

By convection any given particle moves from one column to the next. If it ends up in the last lane ($l = N - 1$) in one gap, it will be shifted to the first lane ($l = 0$) in the subsequent gap. Otherwise it will stay in the current gap and move up one lane. In our model pure convection is therefore described by the discrete map

$$(c, g, l) \mapsto \begin{cases} (c+1, g+1, 0), & \text{if} \quad l = N-1, \\ (c+1, g, l+1), & \text{otherwise.} \end{cases} \tag{10}$$

Because of the finite diameter d of the particle there is a minimum and a maximum lane number that it can occupy. The minimum lane number is the smallest integer l_{min} that satisfies

$$\sum_{l=0}^{l_{\text{min}}} w_1^{(l)} > \frac{d}{2}. \tag{11a}$$

Similarly, the maximum lane number l_{max} is the largest integer that satisfies

$$\sum_{l=l_{\text{max}}}^{N-1} w_1^{(l)} > \frac{d}{2}. \tag{11b}$$

Consequently, the simple convection mapping from equation (10) needs to be modified to account for the finite size of the particles

$$(c, g, l) \mapsto \begin{cases} (c+1, g+1, l_{\text{min}}), & \text{if} \quad l = N-1, \\ (c+1, g, l+1), & \text{if} \quad l < l_{\text{max}} - 1, \\ (c+1, g, l_{\text{max}}), & \text{otherwise.} \end{cases} \tag{12}$$

The above convection scheme accounts for the separation of particles in deterministic lateral displacement devices

according to size. The critical particle diameter predicted by this model is

$$d_c = 2w_1^{(0)} \tag{13}$$

in accordance with the geometric arguments of [3].

To characterize the separation quantitatively, we define the relative particle numbers r_0, r_1 and r_d as

r_0 = relative number of particles following the zigzag path, (14*a*)

r_1 = relative number of particles following the displacement path, (14*b*)

r_d = relative number of all other particles. (14*c*)

With these definitions the sum $r_0 + r_1 + r_d$ is always unity. If $r_0 = 1$ all particles follow the zigzag path and if $r_1 = 1$ all particles follow the displacement path. If $r_d \neq$ some of the particles end up at positions not explained by the deterministic analysis of the separation process. In figure 4 we have plotted the relative particle numbers r_0, r_1 and r_d as a function of the average particle diameter d.

3.2. Pure mono-disperse convection

For mono-disperse and non-diffusing particles, the model results, as expected, in two modes: the zigzag mode and the displacement mode, see the closed circles in figure 4. For $d < d_c$ we have $r_0 = 1$, and for $d \geqslant d_c$ we have $r_1 = 1$, while we always have $r_d = 0$. The relative particle numbers can therefore be written as

$$(r_0, r_d, r_1) = \begin{cases} (1,0,0) & \text{for} \quad d < d_c, \\ (0,0,1) & \text{for} \quad d \geqslant d_c. \end{cases} \tag{15}$$

3.3. Influence of size dispersion

If we assume that the particles are not mono-disperse, but are distributed around a mean size d with standard deviation Δd, the shift as a function of d from the zigzag mode to the displacement mode happens gradually instead of abruptly at a certain critical size d_c (figure 4, closed squares). The relative number of particles following the zigzag path r_0 can be found by integrating over all particle sizes smaller than the critical diameter given by the array geometry

$$r_0 = \int_{-\infty}^{d_c} \frac{1}{\sqrt{2\pi(\Delta d)^2}} \exp\left(\frac{-(s-d)^2}{2(\Delta d)^2}\right) \mathrm{d}s. \tag{16a}$$

Similarly, the relative number of particles following the displacement path r_1 can be found by integrating over all particle sizes larger than d_c

$$r_1 = \int_{d_c}^{\infty} \frac{1}{\sqrt{2\pi(\Delta d)^2}} \exp\left(\frac{-(s-d)^2}{2(\Delta d)^2}\right) \mathrm{d}s. \tag{16b}$$

The system is still a bi-modal system because $r_d = 0$ for all particle sizes.

3.4. Influence of diffusion

In 1D during the time step τ a particle diffuses the distance ℓ, the average of which is the size-dependent diffusion length $\sigma(d)$ given by

$$\sigma(d) = \langle \ell \rangle = \sqrt{2D\tau} = \sqrt{2\frac{k_B T}{3\pi\eta d}\frac{\lambda}{u_0}}. \tag{17}$$

In our model we discretize the transverse diffusion as the properly rounded number n_{jump} of flow lanes crossed by the particle during diffusion,

$$n_{\text{jump}} = \frac{N}{\lambda}\,\ell. \tag{18}$$

The addition of diffusion smears out the displacement of the particles and causes the critical diameter to be larger than in the diffusion-less case (figure 4, open symbols).

3.4.1. *Bumping criterion for small particles.*

Very small particles are completely dominated by diffusion, and the particle distribution at the end of the array is simply given by the transverse diffusion of the particles during the time L/u_0 it takes for the particle to be convected all the way L through the array, see figure 2(*a*). For small particles we therefore have

$$r_0 = \int_{-\frac{3}{2}\frac{\lambda}{N}}^{\frac{3}{2}\frac{\lambda}{N}} \frac{1}{\sqrt{2\pi\sigma^2}} \exp\left(\frac{-x^2}{2\sigma^2}\right) \mathrm{d}x, \tag{19}$$

where $\sigma^2 = 2DL/u_0$. In figure 4 we have plotted r_0 versus d/d_c and $r_d = 1 - r_0$ as the thick black curves in the interval $0 < d/d_c < 2.1$.

As the particle diameter d is increased, the bumpers begin to become important as the diffusion length $\sigma(d)$, equation (17), is decreased and becomes equal to the displacement length ℓ_{disp}, equation (5). Using the criterion $\sigma(d_1) = \ell_{\text{disp}}$, with the parameter values used in figure 4, we find that particles stop behaving as small diffusion-dominated particles and start interacting with the bumpers when $d_1 = 2.1 d_c$. This cross-over value is indicated by the left-most vertical lines in figure 4, and it fits well with the simulation data. Note that the specific value of the pre-factor is determined for $d_c = 118$ nm.

3.4.2. *Bumping criterion for large particles.*

Large particles will interact with the bumpers at every row in the array and their position is thus reset at every bump to be ℓ_{disp}, see figure 2(*b*). Diffusion can therefore be neglected for such particles, they all follow the displacement path, and $r_1 = 1$.

As the particle diameter is lowered, the probability p_{esc} that a particle escapes the displacement path can be estimated by the probability of diffusing from the displaced position to the last flow lane in the gap, i.e. the distance $\ell_{\text{disp}} - \frac{\lambda}{N}$. This probability p_{esc} is given by equation (8). In figure 4 we have plotted $r_d = p_{\text{esc}}$ and $r_1 = 1 - r_d$ as thick black curves in the interval $3.4 < d/d_c < 6$.

In order to follow the displacement path, a particle must bump at each row in the array. If we consider an N-periodic array with m full periods, the particles will have mN bumping opportunities as they pass through the entire array. If a particle

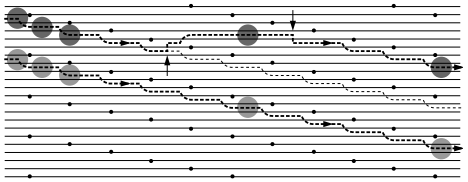

Figure 5. Schematics of a $N = 5$ bumper array (black dots) in which a large particle (light gray) moves along the displacement path (lower thick dashed line) without diffusion, and another particle of the same size (dark gray) moves partially along the displacement path (upper thick dashed line) under the influence of diffusion. The corresponding displacement path without diffusion is also shown (thin dashed line). Two diffusion-induced jumping events, each causing the particle to jump to a neigboring lane, are marked by the vertical arrows. The upward event induces a shift in the gap number by one, while the downward event does not induce a shift in the gap number. The diffusing particle thus exits the bumper array one gap above its diffusionless counter part.

evades bumping at a bumper, it will be convected by the flow through a full period of the array before bumping is possible again. Because of the escape, it will miss N bumping opportunities and end up one gap from the displacement path, see figure 5. Consequently, if a particle escapes one time, it will only have $(m-1)N$ bumping opportunities and has therefore escaped bumping with a probability of $1/[(m-1)N]$. The upper critical particle size d_2 for convection-induced displacement is defined using equation (8) as

$$p_{\text{esc}}(d_2) = \frac{1}{(m-1)N}. \tag{20}$$

For the device used in the experiments by Larsen [6] we find $d_2 = 3.4 d_c$. The predicted upper limit for diffusion dominated motion and the lower limit for convection-induced displacement compares well with the experimental observation by Larsen [6] that some particles end up in a transition region between the displacement path and the zigzag path (figure 3, gray triangles). Based on the data for $1/N = 1/100$ in figure 3 the experimentally observed transition region begins at $d_1 = 0.16 w_g = 1.4 d_c$ (the highest lying gray triangle) and ends at $d_2 = 0.40 w_g = 3.4 d_c$ (the lowest lying white triangle). Considering the simplicity of the discrete model this is in fair agreement with our model predictions, $d_1 = 2.1 d_c$ and $d_2 = 3.4 d_c$.

4. Conclusion

Experimental data on separation of particles in bumper arrays all show a systematic deviation from predictions made from the bifurcating flow-lane model [1, 3, 6]. Application of the model presented in this paper to the available data suggests that this systematic deviation may be explained by diffusion. In addition, we have proposed a simple discrete model for quickly simulating particle separation in bumper arrays. In contrast to the single critical particle size found in earlier analyses based solely on the deterministic separation processes, our work including diffusion identifies two particle sizes characteristic for the separation in bumper arrays: a small particle size d_1 below which diffusion dominates and a larger particle size d_2 above which the deterministic processes govern the sorting. Particles of intermediate sizes will neither follow the average flow direction nor the direction set by the array geometry. If bumper devices are scaled down both d_1 and d_2 are larger than the critical size predicted in the existing literature.

The presented model takes particle diffusion and size dispersion into account and has been validated against experimental data for a bumper device with period $N = 100$. In this example the transition from zigzag paths to displacement paths happens at particle sizes in the interval from 2.1 to 3.4 times the critical particle size predicted from geometrical arguments. This transition interval is in qualitative correspondence with the experimental observations from Larsen [6]. Our discrete model and the estimates presented in this paper suggest that particles smaller than twice the geometrical critical size of the $N = 100$ bumper device behave diffusively and are not affected by the bumpers because the small diffusive particles rarely come into contact with the bumpers due to random Brownian motion. We believe that our discrete model will be useful for design and evaluation of bumper arrays with any given specification.

Acknowledgments

We thank David W Inglis, Asger Vig Larsen, Anders Kristensen, Jason Beech and Jonas Tegenfeldt for inspiring discussions on experimental issues. Martin Heller was supported by the Danish Research Council for Technology and Production Sciences grant no. 26-04-0074.

References

[1] Huang L R, Cox E C, Austin R H and Sturm J C 2004 *Science* **304** 987–90

[2] Zheng S, Yung R, Tai Y-C and Kasdan H 2005 *Proc. 18th IEEE Int. Conf. on Micro Electro Mechanical Systems (Miami, USA)* pp 851–4

[3] Inglis D W, Davis J A, Austin R H and Sturm J C 2006 *Lab Chip* **6** 655–8

[4] Davis J A, Inglis D W, Morton K J, Lawrence D A, Huang L R, Chou S Y, Sturm J C and Austin R H 2006 *Proc. Natl Acad. Sci.* **103** 14779–84

[5] Bruus H 2008 *Theoretical Microfluidics* (Oxford: Oxford University Press)

[6] Larsen A V 2006 Deterministic bio separation devices *MSc Thesis* Technical University of Denmark www.nanotech.dtu.dk/NSE-optofluidics

B.2. Paper published in Physical Review E

Title Multi-directional sorting modes in deterministic lateral displacement devices.

Authors Brian R. Long, Martin Heller, Jason P. Beech, Heiner Linke, Henrik Bruus, and Jonas O. Tegenfeldt.

Reference Published in Physical Review E **78**, in press (2008).

Multi-directional sorting modes in deterministic lateral displacement devices

Brian R. Long[†*], Martin Heller[‡], Jason P. Beech[*], Heiner Linke[†], Henrik Bruus[‡] and Jonas O. Tegenfeldt[*]
[†]*Materials Science Institute and Department of Physics, University of Oregon, Eugene, Oregon 97403-1274 USA*
[‡]*Department of Micro- and Nanotechnology, Technical University of Denmark, DTU Nanotech Building 345 East, DK-2800 Kongens Lyngby, Denmark*
[*]*Department of Physics, Division of Solid State Physics & Nanometer Consortium, Lund University, S-22100 Lund, Sweden*
(Dated: September 12, 2008)

Deterministic lateral displacement (DLD) devices separate micrometer-scale particles in solution based on their size using a laminar microfluidic flow in an array of obstacles. We investigate array geometries with rational row-shift fractions in DLD devices by use of a simple model including both advection and diffusion. Our model predicts novel multi-directional sorting modes that could be experimentally tested in high-throughput DLD devices containing obstacles that are much smaller than the separation between obstacles.

PACS numbers: 05.40.Jc, 47.57.eb, 47.57.ef, 66.10.C-, 64.70.pv, 82.70.Dd

I. INTRODUCTION

Deterministic lateral displacement (DLD) is a mechanism of particle separation that uses the laminar properties of microfluidic flows in a periodic array of posts to sort particles based on size. This technique has been shown to differentiate between micrometer-sized particles with a resolution in diameter on the order of 20 nm. The basic sorting mechanism has been described for the devices used experimentally: particles smaller than a critical radius r_c follow streamlines through the array while larger particles are systematically 'bumped' laterally during each interaction with a post [1–3].

Previous analysis of DLD sorting has focused on predicting r_c as a function of array parameters, typically the width of the gap between posts and the shift of posts between rows. Once basic hydrodynamics is included, theoretical calculations of r_c agree with experimental results within about 5 % [2, 4, 5]. Inclusion of diffusion in DLD sorting has been described using rough estimations [1–3], and in more detailed studies that incorporate both microfluidic advection and diffusion to calculate r_c under a range of experimental conditions [5].

Previous analysis of the geometry of the DLD array has been limited to the following conventional case. In a given row the center-to-center distance between the posts is denoted λ, see Fig. 1. The subsequent row of posts is placed at a distance $\alpha\lambda$ downstream from the first row. Normally, α is chosen to be unity, however this is not an essential requirement. The posts in this second row are displaced a distance $(1/N)\,\lambda$ along the row, where N traditionally has been an integer. The ratio $1/N$ is also denoted the row-shift fraction ϵ. In row number $N+1$ the posts have the same positions as in the first row, and consequently the array is cyclic with period N. Due to this periodicity of the array and the laminarity of the flow, the stream can naturally be divided into N flow lanes, each carrying the same amount of fluid flux, and each having a specific path through the device [1].

For devices with the simple row-shift fraction $\epsilon = 1/N$ and disregarding particle diffusion, only one critical separation size r_c is introduced. Spherical particles with a radius smaller than r_c will move forward along the main flow direction through the device, defining the angle $\theta = 0$. However, particles with a radius larger than r_c are forced by collisions with the posts to move in a skew direction at an angle θ given by $\tan\theta = 1/(\alpha N)$. Taking diffusion into account the transition from straight to skew motion takes place over a finite range of particle sizes [1–3, 5].

In this paper we generalize the array geometry by studying the effects of row-shift fractions different from that of the conventional, simple $(1/N)$-array. We show in Sec. II that by displacing consecutive rows by the rational fraction $\epsilon\lambda = (M/N)\lambda$, where M is an integer that is not a divisor of N, two new separation modes appear, each associated with a distinctive range of particle sizes and separation directions θ. Furthermore, to test experimental feasibility of the novel separation modes, we introduce in Sec. III a model of the DLD system reduced to its essential elements: particle trajectories interrupted by size-dependent interactions with a periodic array of posts. Utilizing these simplifications, we investigate in Sec. III A the advection and diffusion of particles in the M/N-array geometries, and discuss in Sec. IV possible experimental consequences of our novel DLD system.

In our model of the DLD system described in Sec. III we reduce the posts to point-like obstacles in a uniform flow. This particular case is currently of interest to researchers looking to apply DLD separation to high-throughput microfluidic devices. Such a reduced post size decreases hydraulic resistance and thus increases the liquid throughput for a given pressure difference applied along the device. One promising method to create such devices is to use arrays of semiconductor nanowires [6] in a microfluidic channel.

II. BASIC THEORETICAL ANALYSIS

The introduction of a non-simple row-shift fraction $\epsilon = M/N$ in the DLD system is first discussed in Sec. II A for the specific case of $M/N = 3/8$, since all the novel separation modes are present in that device geometry. Fig. 1 shows the principle of the fractionally displaced DLD array leading to multi-directional separation of particles of different sizes.

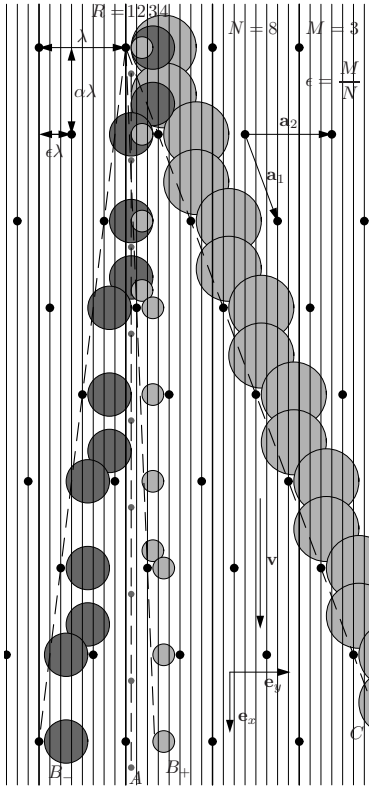

FIG. 1: An array of posts (marked by black dots) with period $N = 8$ and a shift of $M = 3$ flow lanes per row, i.e., a row-shift fraction $\epsilon = 3/8 = 0.375$. The flow $\mathbf{v}$ is directed along the x-axis from top to bottom. The dashed lines indicate the four possible separation directions. First, the two well-known modes: the straight mode A with $\theta_A = 0°$ for particles of radius r with $r < (1/N)\lambda$ (small dark gray circles starting in flow lane $R = 1$), and the maximal displacement mode C with $\theta_C = 20°$ for $(3/N)\lambda < r$ (large light gray circles starting in flow lane $R = 4$). Additionally, the two novel separation modes: one B_+ towards the right with angle $\theta_{B_+} = 2.4°$ for $(1/N)\lambda < r < (2/N)\lambda$ (small light gray circles starting in flow lane $R = 2$), and another B_- towards the left with angle $\theta_{B_-} = -7.1°$ for $(2/N)\lambda < r < (3/N)\lambda$ (large dark gray circles starting in flow lane $R = 3$). The solid vertical lines indicate the flow lanes of width λ/N, while $\mathbf{a}_1$ and $\mathbf{a}_2$ are the lattice vectors, and α is an aspect ratio.

As was the case for the simple row shift fraction $1/N$, the rational row-shift fraction M/N also naturally leads to N flow lanes, each carrying the same amount of fluid flux. In this section, all particles are assumed to follow these flow lanes unless bumped by an interaction with a post. However, in contrast to the traditional DLD geometries, now the posts are displaced M flow lanes instead of just a single flow lane when passing from one row of posts to the next.

In Sec. II B we analyze this more general case of M/N-arrays, where the integer row-shift M and the integer array-period N have no common divisors.

A. The specific row-shift fraction 3/8

First we consider the explicit choice of parameters given in Fig. 1, namely, a period $N = 8$, and a row-shift of $M = 3$ lanes in the y-direction $\mathbf{e}_y$, i.e., a row-shift fraction of $\epsilon = 3/8$. The flow $\mathbf{v}$ is in the x-direction $\mathbf{e}_x$. For simplicity, we employ the most simple model where all flow lanes are assumed to have the same width λ/N, and where the particles are not subject to Brownian motion. The analysis can straightforwardly be extended to take the different widths of the flow lanes [2] as well as diffusion [5] into account.

The analysis is most easily carried out by considering spherical particles of increasing radius r. As the rows in Fig. 1 are shifted to the right, it is natural to choose the starting point of a given particle to be directly to the right of a post, placing the particle's center in flow lane $R = 1, 2, 3$, or 4 according to size.

For the smallest particles with $r < \lambda/N$, labeled A in Fig. 1, we obtain a path corresponding to the familiar so-called zigzag path defined in Ref. [1]. Due to the point-like nature of our obstacles, the path is a straight line, indicated by the dashed vertical line in Fig. 1. The path angle is $\theta_A = \arctan 0 = 0°$.

For the next set of particles with $\lambda/N < r < 2\lambda/N$, ($B_+$ in Fig. 1), we note that they are not affected significantly by passing the second rows of posts. The displacement of $(M/N)\lambda$ is larger than the size of the particle. By simple inspection we find that the particles interact with a post in the fourth row leading to a bump of one lane width to the right. This bumping brings the particles back to a position just right of a post, and we have identified a new separation mode, B_+. The direction of mode B_+ can be characterized by the integers

p = the number of rows after which the bumping pattern repeats itself, and (1a)

q = the number of flow lanes that the particles are bumped to the right while traveling through p rows. (1b)

Here, with $p = 3$ and $q = 1$ and the array parameters indicated in Fig. 1, the path angle of mode B_+ is found to be $\theta_{B_+} = \arctan\left[1/(\alpha \times 3 \times 8)\right] = 2.4°$. Here and in the following we choose the aspect ratio $\alpha = 1$.

For the third set of particles with $2\lambda/N < r < 3\lambda/N$, marked as B_- in Fig. 1, we note that they collide with a post in the second row and are bumped two lanes to the left. After two

*Current address: Biomedicial Engineering Division, Oregon Health and Science University, 3303 S.W. Bond Ave. Portland, OR, 97239

TABLE I: List of separation radii r and angles θ as a function of the integer array parameters N, M, p and q for $\alpha = 1$.

N	M	mode	particle radius in units of lane width	q/p	separation angle $\theta = \arctan\left[\frac{p}{qN}\right]$
5	2	A	$0 < r < 1$	0/1	0.0°
		B_-	$1 < r < 2$	−1/2	−5.7°
		C	$2 < r < 2.5$	2/1	21.8°
7	2	A	$0 < r < 1$	0/1	0.0°
		B_-	$1 < r < 2$	−1/3	−2.7°
		C	$2 < r < 3.5$	2/1	15.9°
7	3	A	$0 < r < 1$	0/1	0.0°
		B_-	$1 < r < 3$	−1/2	−4.1°
		C	$3 < r < 3.5$	3/1	23.2°
8	3	A	$0 < r < 1$	0/1	0.0°
		B_+	$1 < r < 2$	1/3	2.4°
		B_-	$2 < r < 3$	−2/2	−7.1°
		C	$3 < r < 4.0$	3/1	20.6°
9	2	A	$0 < r < 1$	0/1	0.0°
		B_-	$1 < r < 2$	−1/4	−1.6°
		C	$2 < r < 4.5$	2/1	12.5°
9	4	A	$0 < r < 1$	0/1	0.0°
		B_-	$1 < r < 4$	−1/2	−3.2°
		C	$4 < r < 4.5$	4/1	24.0°
10	3	A	$0 < r < 1$	0/1	0.0°
		B_-	$1 < r < 3$	−1/3	−1.9°
		C	$3 < r < 5.0$	3/1	16.7°
11	2	A	$0 < r < 1$	0/1	0.0°
		B_-	$1 < r < 2$	−1/5	−1.0°
		C	$2 < r < 5.5$	2/1	10.3°
11	3	A	$0 < r < 1$	0/1	0.0°
		B_+	$1 < r < 2$	1/4	1.3°
		B_-	$2 < r < 3$	−2/3	−3.5°
		C	$3 < r < 5.5$	3/1	15.3°
11	4	A	$0 < r < 1$	0/1	0.0°
		B_+	$1 < r < 3$	1/3	1.7°
		B_-	$3 < r < 4$	−3/2	−7.8°
		C	$4 < r < 5.5$	4/1	20.0°
11	5	A	$0 < r < 1$	0/1	0.0°
		B_-	$1 < r < 5$	−1/2	−2.6°
		C	$5 < r < 5.5$	5/1	24.4°
12	5	A	$0 < r < 1$	0/1	0.0°
		B_+	$1 < r < 2$	1/5	1.0°
		B_-	$2 < r < 5$	−2/2	−4.8°
		C	$5 < r < 6.0$	5/1	22.6°

rows, the particles are again bumped two lanes to the left, and we have identified another new separation mode, B_-. Given this period $p = 2$ bumping of $q = -2$ flow lanes (where minus indicates displacement to the left), the path angle of mode B_- is found to be $\theta_{B_-} = \arctan\left[-2/(\alpha \times 2 \times 8)\right] = -7.1°$.

Finally, the fourth set of particles (with $3\lambda/N < r$) is considered, shown as the large light gray circle in Fig. 1. Since $3\lambda/N$ equals the row-shift $\epsilon\lambda$, these large particles collide with a post in each row ($p = 1$) where they are bumped $q = M = 3$ lanes to the right. This is the conventional maximal displacement mode C [1]. As a result the path angle for mode C here is found to be $\theta_C = \arctan\left[3/(\alpha \times 8)\right] = 20.6°$.

B. General row-shift fractions M/N

In the general case of a DLD device with period N and a row-shift of M flow lanes, it is useful to introduce the floor function $\lfloor x \rfloor$ of x, which gives the largest integer smaller than or equal to x, eg., $\lfloor 8/3 \rfloor = 2$ and $\lfloor 10/3 \rfloor = 3$, and the ceiling function $\lceil x \rceil$ of x which gives the smallest integer larger than or equal to x (see also the definitions given at Ref. [7]).

Using the notation in Fig. 1, the flow lane R occupied by the center of the particles can be expressed in terms of the particle radius r as $R = \lceil rN/\lambda \rceil$, so that $R = 1, 2, 3, \ldots, \lceil N/2 \rceil$ for $0 < r < \lambda/2$.

Two cases are straightforward to analyze. For small radii with $R = 1$, the particles will follow the streamlines without any systematic net lateral displacement, i.e., a mode A in the direction $\mathbf{t}_A$ given by

$$\mathbf{t}_A = \alpha\, \mathbf{e}_x, \tag{2}$$

and forming the path angle θ_A with the x-axis,

$$\theta_A = 0, \quad R = 1. \tag{3}$$

For large radii with $M < R < \lceil \frac{N}{2} \rceil$, the particles collide with the posts and are bumped M flow lanes to the right in each row, but they do not get stuck between the posts; this is mode C. The path is directed along the direction $\mathbf{t}_C$ given by

$$\mathbf{t}_C = \alpha\, \mathbf{e}_x + \frac{M}{N}\, \mathbf{e}_y, \tag{4}$$

and forming the path angle θ_C with the x-axis,

$$\theta_C = \arctan\left[\frac{M}{\alpha N}\right], \quad M < R < \left\lceil \frac{N}{2} \right\rceil. \tag{5}$$

In a given M/N array, modes with larger sorting angles are excluded because of the post spacing in the y-direction: particles with radius $r > \lambda/2$ are unable to fit between the posts.

If the particles are small enough to pass the second row without getting bumped to the right, but too large for mode A, $1 < R \leq M$, their trajectories fall into one or two B modes.

As a particle is convected through the array, a post will approach the particle from the left in steps of M flow-lanes per row the particle advances, hence the use of modulus M arithmetic in the following analysis.

If $(N \bmod M) < R \leq M$ the particle will hit the post with its center to the left of this obstacle and will therefore enter mode B_- where it is displaced to the left with a period $p_- = \lfloor \frac{N}{M} \rfloor$. This is most readily seen by starting the analysis with a particle position just left of a post. A particle with $(N \bmod M) < R \leq \left[(N - R + 1) \bmod M\right]$ will bump left after $p_- = \lfloor \frac{N}{M} \rfloor$ rows and will again be in a position just left of a post. The small particle in mode B_- of Fig. 2 is an example of this behavior. Slightly larger particles with $\left[(N - R + 1) \bmod M\right] < R \leq M$ will bump right after $p = \lfloor \frac{N-R+1}{M} \rfloor$ rows. Since we are only considering particles with $R \leq M$, this displacement will always be less than M flow lanes, and the particle is therefore bound to bump left on

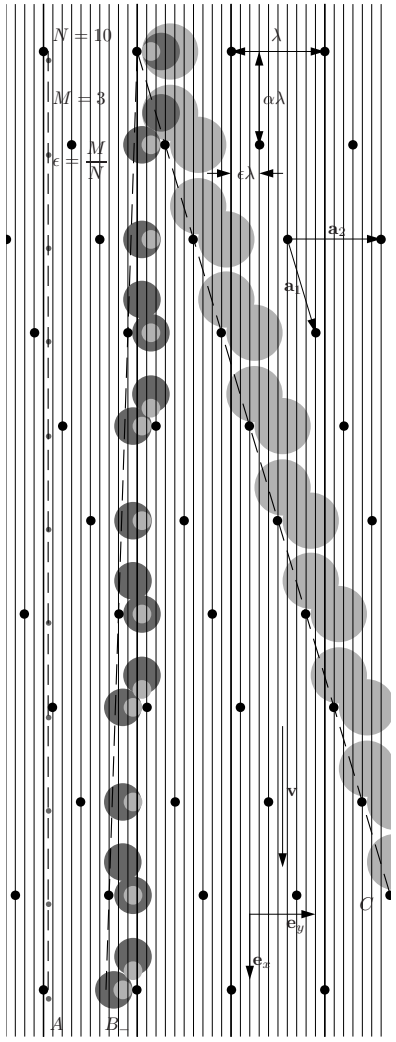

FIG. 2: An array with period $N = 10$ and a shift of $M = 3$ flow lanes per row, giving a row-shift fraction $\epsilon = 3/10 = 0.3$. The flow $\mathbf{v}$ is directed along the x-axis from top to bottom. Here there are three sorting modes, delimited by two critical radii. Mode A for particles of radius r with $r < r_{c1} = (1/10)\lambda$ (shown on the far left), and mode C, the maximal displacement mode for $(3/10)\lambda = r_{c2} < r < (1/2)\lambda$ (large light gray circles). A novel mode B_- displaces particles with $r_{c1} < r < r_{c2}$ towards the left (large dark gray and intermediate, light gray circles).

the post in the following row, i.e., after a total of $p_- = \lfloor \frac{N}{M} \rfloor$ rows. The large B_- mode particle in Fig. 2 is an example of this behavior.

The trajectories in mode B_- have period $p_- = \lfloor \frac{N}{M} \rfloor$. The number q_- of lanes bumped after passing these p_- rows is $q_- = Mp_- - N < 0$. The path is directed along the direction $\mathbf{t}_{B_-}$ given by

$$\mathbf{t}_{B_-} = \alpha p_-\, \mathbf{e}_x + \frac{q_-}{N} \mathbf{e}_y, \tag{6a}$$

$$p_- = \left\lfloor \frac{N}{M} \right\rfloor, \tag{6b}$$

$$q_- = Mp_- - N < 0, \tag{6c}$$

forming the path angle θ_{B_-} with the x-axis,

$$\theta_{B_-} = \arctan\left[\frac{q}{\alpha p_- N}\right] < 0. \tag{7}$$

If $1 < R \leq (N \bmod M)$ the particle will enter mode B_+ where it is displaced to the right with a period $p_+ = \lfloor \frac{N+R}{M} \rfloor$. To realize this it is natural to start the analysis with the particle just right of a post. Again, a post will approach the particle from the left in steps of M lanes as the particle moves through the array. A particle with $1 < R \leq \lceil \frac{M}{2} \rceil$ will follow the flow for $p_+ = \lfloor \frac{N+R}{M} \rfloor$ rows and then bump right. If $\lceil \frac{M}{2} \rceil < R \leq (N \bmod M)$ the particle will bump left already in the second row of posts. The particle is now in a position just left of a post. However, since it is not large enough to follow the B_- path, it will bump right when it meets the post after $p_+ = \lfloor \frac{N+R}{M} \rfloor$ rows.

The trajectories in mode B_+ have period $p_+ = \lfloor \frac{N+R}{M} \rfloor$. After p_+ rows the particles will get bumped q_+ flow lanes to the right given by $q_+ = Mp_+ - N > 0$. The path is directed along the direction $\mathbf{t}_{B_+}$ given by

$$\mathbf{t}_{B_+} = \alpha p_+\, \mathbf{e}_x + \frac{q_+}{N} \mathbf{e}_y, \tag{8a}$$

$$p_+ = \left\lfloor \frac{N+R}{M} \right\rfloor, \tag{8b}$$

$$q_+ = Mp_+ - N > 0, \tag{8c}$$

forming the path angle θ_{B_+} with the x-axis,

$$\theta_{B_+} = \arctan\left[\frac{q_+}{\alpha p_+ N}\right] > 0. \tag{9}$$

In terms of the flow lane number R, the criteria for the four different displacement modes can be summarized as follows

mode A,	if $R = 1$	(10a)
mode B_+,	if $1 < R \leq (N \bmod M)$	(10b)
mode B_-,	if $(N \bmod M) < R \leq M$	(10c)
mode C,	if $M < R \leq \lceil \frac{N}{2} \rceil$.	(10d)

Note that mode B_+ vanishes if $(N \bmod M) = 1$.

III. MODEL AND IMPLEMENTATION

The following model is established to numerically test the sorting behavior of a particular M/N DLD array and take into account the effect of particle diffusion on sorting behavior, as discussed below. We treat the device as a periodic array of zero-radius posts with the geometry shown in Fig. 2. This $N = 10$, $M = 3$ geometry, with a row-shift fraction given by $\epsilon = 3/10$, exhibits the three modes shown in Table I, including a novel sorting mode, B_-.

We assume the array to be infinitely deep so that the flow field is two-dimensional and independent of the z-direction. Consistent with the infinitesimal size of the posts, the liquid flow through the device is assumed to be uniform with velocity $\mathbf{v} = v\,\mathbf{e}_x$ along the x-axis. Thus, our model does not describe Taylor-Aris dispersion, which in real systems with finite-sized posts would be induced along the x-direction by a combination of transverse diffusion and transverse velocity gradients [8]. The particles only interact with the posts through a hard-wall repulsion and any effect of the particles on fluid flow is neglected. The particle-post interaction excludes the center of a particle with radius r from a circular region of the same radius around the point-sized post. In addition to being moved by the fluid and interacting with the posts, each particle has a diffusion coefficient D given by the Einstein relation

$$D(r) = \frac{k_B T}{6\pi\eta r}, \tag{11}$$

where $k_B T$ is the thermal energy and η is the viscosity of the solution. For the calculations below we have chosen the following experimentally relevant parameters: For water at room temperature $k_B T \approx 4 \times 10^{-21}$ J and $\eta \approx 10^{-3}$ Pa s, and for the geometry the post separation is $\lambda = 10$ µm and particle radii in the range 0.5 µm $< r < 4$ µm. A final basic assumption of our model is that all time dependence in our model is implicitly given by the advective flow speed v. For particles starting at the entrance of the device at $x = 0$ the time t is given through its x-coordinate as $t = x/v$. The model therefore allows all the relevant dynamics of an ensemble of many particles to be described by a continuous concentration distribution $c(x, y)$ with some given initial distribution $c(0, y)$ at the entrance of the DLD device. Given $c(0, y)$ the time-evolution of the distribution consists of calculating $c(\Delta x, y)$ after convection to $x = \Delta x$. By following the evolution of $c(x, y)$ as the distribution interacts with posts and responds to thermal forces, our model can identify the basic modes of transport in an array of posts and the effect of diffusion on this transport.

The initial distribution $c(0, y)$ is given by a box distribution of width λ (although a narrow distribution is used in Fig. 3 for visual clarity), and the distribution $c(\Delta x, y)$ is calculated from the previous distribution $c(0, y)$ taking into account its interactions with the posts as well as the diffusion equation. The entire distribution $c(x, y)$ is evaluated by iterating the following procedure:

1. Upon encountering a row of posts, the distribution for particles of radius r is set to zero in regions with a distance smaller than r to any post, and the corresponding number of particles is then added to the distribution in the adjacent pixels to maintain the total number of particles (see Fig. 3).

2. The distribution $c(x, y)$ is subsequently evolved in accordance with the diffusion equation, with the diffusion coefficient given by Eq. (11),

$$v\frac{\partial c}{\partial x} = D\frac{\partial^2 c}{\partial y^2}, \tag{12}$$

employing the implicit time $t = x/v$ set by convection along the x-direction, and using the Fourier cosine transformation in the transverse y-direction as described below.

The computation uses a finite array of width $w = 10\lambda$, i.e. containing 10 posts, and the row separation is again taken to be equal to the post separation, i.e. $\alpha = 1$. The array with width w is discretized in y into $n_{\max} = 10^4$ pixels of size $\Delta w \times \Delta x$ with $\Delta x = \Delta w = w/n_{\max}$.

The discrete Fourier cosine transformation $C(x, k_n)$ of the distribution $c(x, y)$ then takes the form

$$C(x, k_n) = \frac{2 - \delta_{0,n}}{w} \int_0^w c(x, \tilde{y})\, \cos(k_n \tilde{y})\, \mathrm{d}\tilde{y}, \tag{13}$$

where k_n is given by

$$k_n = \frac{2\pi}{w}\, n, \quad n = 0, 1, 2, \ldots, n_{\max} = \frac{w}{\Delta w}. \tag{14}$$

By direct inspection we find the well-known result from the y-dependent diffusion equation in Fourier space that, during the time step $\Delta t = \Delta x/v$, $C(x, k_n)$ evolves into $C(x + \Delta x, k_n)$ as

$$C(x + \Delta x, k_n) = C(x, k_n)\, \exp\left[-Dk_n^2 \frac{\Delta x}{v}\right]. \tag{15}$$

By the inverse Fourier cosine transform we can therefore write the distribution at row $x + \Delta x$ in terms of that at row x as

$$c(x + \Delta x, y) = \sum_{n=0}^{n_{\max}} C(x, k_n)\, \exp\left[-Dk_n^2 \frac{\Delta x}{v}\right] \cos(k_n y). \tag{16}$$

which by construction automatically respects the boundary condition that no particles can diffuse beyond the edges of the array. The evolution of the distribution due to diffusion is computed at each row of pixels after the effects of posts on the distribution have been taken into account.

To elucidate the sorting mechanism in the absence of thermal forces, calculations were also done with diffusion coefficient $D = 0$, in which case $c(x, y)$ evolves only according to the interaction of the particles with the posts. Results of these calculations are shown as $D = 0$ in Fig. 4.

While $c(x, y)$ is the calculated distribution at a given time and position in the array, the set of all $c(x, y)$ also represents the steady-state distribution of a stream of particles entering an array of obstacles and moving constantly through the array, as seen in Fig. 3.

The calculations were done using Matlab on a personal computer and a 64-bit dual processor workstation.

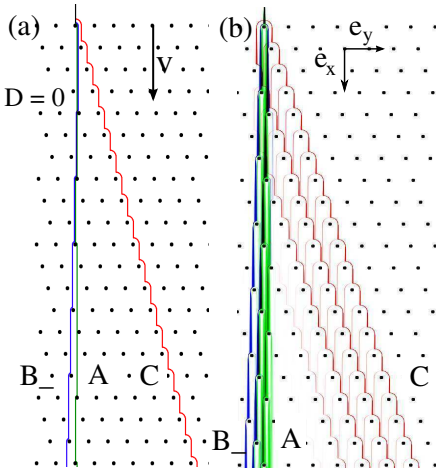

FIG. 3: (Color online) Composite image of numerically calculated spatial distributions for a device with $N = 10$ and $M = 3$. (a) Results for $D = 0$ for particles with radii $r < r_{c1}$ (mode A), $r_{c1} < r \le r_{c2}$ (mode B) and $r > r_{c2}$ (mode C). (b) Particles, with the same radii as in (a), moving through the array with a flow speed of $v = 100$ µm/s, including the effect of diffusion. Broadening of all distributions due to diffusion can be seen and particles in mode C are sorted less efficiently. Initial spatial distributions here are the same for all particle radii, and a narrow initial distribution is used for visual clarity.

A. Results

1. *Three transport modes in the 3/10-array*

The existence of the novel sorting mode B_-, as well as the two modes A and C previously described in DLD literature are confirmed by applying our numerical model to a range of particle sizes advected through the 3/10-array. As the particle distributions move through the array, their trajectories form three modes A, B and C, according to two critical radii, r_{c1} and r_{c2}, see Fig. 3(a). Our calculations reproduce the two known modes: the 'zigzag mode' A, in which there is no average displacement from the direction of flow, and the 'bumped mode' C, in which particles are bumped laterally in every row. These two modes are most clearly seen in Fig. 3(a), where the distributions are calculated without diffusion. In mode A, where $r \le r_{c1} = (1/N)\lambda$, particles may interact with the posts, but no net lateral displacement is accomplished. Mode C is characterized by a displacement equal to the shift $(M/N)\lambda$ for every row the particles pass through. In the novel mode B_-, particles of size $r_{c1} < r \le r_{c2}$ interact with posts more frequently than in mode A but less frequently than in Mode C, as described in Secs. II B. The 3/10 array used here clearly exhibits the lone B_- mode shown in Table I for these array parameters. It is important to note that mode B_- vanishes in the conventional case $M = 1$, and all particles smaller than the critical radius r_{c2} move along the direction of flow.

The directions $\mathbf{t}_A$ and $\mathbf{t}_C$ of the conventional modes A and C are given directly by Eqs. (2) and (4) for $\alpha = 1$:

$$\mathbf{t}_A = \mathbf{e}_x, \tag{17a}$$

$$\mathbf{t}_C = \mathbf{e}_x + \frac{3}{10}\,\mathbf{e}_y, \tag{17b}$$

while the direction $\mathbf{t}_{B_-}$ of mode B_- is found through the path period $p_- = \left\lfloor \frac{N+R}{M} \right\rfloor = \left\lfloor \frac{10+1}{3} \right\rfloor = 3$ and the lane shift $q_- = p_- M - N = 3 \times 3 - 10 = -1$, and thus

$$\mathbf{t}_{B_-} = 3\,\mathbf{e}_x - \frac{1}{10}\,\mathbf{e}_y. \tag{17c}$$

The corresponding displacement angles become

$$\theta_A = \ \ 0.0°, \quad 0\,\frac{\lambda}{10} < r < 1\,\frac{\lambda}{10}, \tag{18a}$$

$$\theta_{B_-} = -1.9°, \quad 1\,\frac{\lambda}{10} < r < 3\,\frac{\lambda}{10}, \tag{18b}$$

$$\theta_C = \ 16.7°, \quad 3\,\frac{\lambda}{10} < r < 5\,\frac{\lambda}{10}. \tag{18c}$$

The array parameters used here can be translated into those used in DLD literature [1–3], simply by setting $M = 1$.

2. *Effect of diffusion on sorting*

The effect of diffusion on the sorting of particles is shown in Fig. 4. The angles shown are measured between $\mathbf{v}$ and the lateral displacement of the center of mass of the distribution for each particle size after 10 rows of posts for high and low flow speeds. We can estimate speeds at which diffusion becomes negligible by comparing the time it takes a particle to be advected along the x-direction from one row to the next, λ/v, to the time it takes a particle to diffuse transversely in the y-direction to reach a position where it would be bumped, $2D/(r - r_{c2})^2$. For high flow speeds,

$$v \gg \frac{2D\lambda}{(r - r_{c2})^2}, \tag{19}$$

diffusion can be neglected, and the transitions between the sorting modes are sharp, as seen in the $D = 0$ case. Note that this velocity diverges as the particle size approaches the critical radius r_{c2}; in this limit the displacement needed for a particle to change sorting directions goes to zero. Within the spatial resolution of this work (1 pixel = 10 nm), the particles

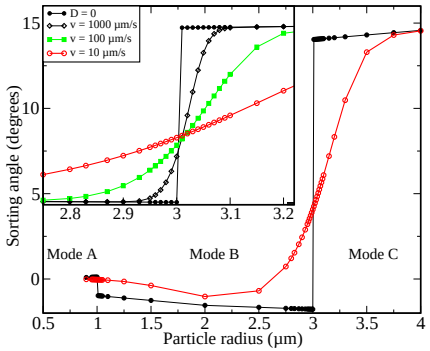

FIG. 4: (Color online) Sorting angles θ calculated for a device with $N = 10$ and $M = 3$ as described in Sec. III with r_{c1} = 1 μm and r_{c2} = 3 μm. The initial position corresponds to the center of mass of the initial distribution between two posts and the final position corresponds to the center of mass after 10 rows. θ is plotted here versus particle radius r with (open circles) and without (filled circles) diffusion with flow velocity $v = 10$ μm/s. The negative sorting angles for $r_{c1} < r < r_{c2}$ indicate the presence of mode B_- for this array. Inset shows the sorting angle θ around $r = r_{c2} = 3$ μm for a range of flow velocities (same y-axis range). Diffusion blurs the sharp transition between the sorting modes, as discussed in Sec. IV B.

closest in size to the critical radius will still be sensitive to diffusion at flow velocities below 10 mm/s. As flow speeds decrease, particles have more time to diffuse transversely as they move through the array, and the effects of thermal motion on sorting are seen more clearly. Transverse diffusion of particles along the y-direction tends to shift the center of mass of the distribution $c(x, y)$ towards the midpoint between posts. This means that particles with $r < r_{c_2} = \frac{3\lambda}{10}$ are more likely to be shifted to higher sorting angles. However, in the regions between rows, diffusion allows particles to move transversely away from the path that would normally be 'bumped' by a post, decreasing their sorting angle. These two effects of diffusion are responsible for the smoothing of the angle versus radius curves for slower flow speeds in Fig. 4. The calculated values for θ_{B-} are in good agreement with the value predicted in Eq. (18a), but for particles with $r > r_{c_2} = \frac{3\lambda}{10}$, the finite width of the initial distribution and the relatively short array size (10 rows) reduce the calculated values for θ_C from the predicted value by about 15 %. The small variation in sorting angle with radius for modes B_- and C for $D = 0$ in Fig. 4 is mainly the result of the two end points used to define the angle being not exactly equivalent: the position of the second, but not the first end point varies continuously with bead size, and so the presented angle varies with bead size. Secondly, since the number of rows is not divisible by the periodicity of mode B_-, an additional small error is introduced. These deviations should vanish for simulations with larger numbers of rows.

IV. DISCUSSION

A. The novel sorting mode and its relation to kinetically locked-in transport

DLD devices have thus far been made with a fixed flow direction and almost exclusively with $M = 1$. However, in theoretical work studying transport through periodic potential landscapes, the direction of the applied force is varied for a fixed array geometry and the transport direction is calculated [9–12]. To calculate the correspondence between varying the array parameters M and N used here and changing the flow direction in a fixed array as in [9–12] is cumbersome, but for a range of flow directions near $\mathbf{t}_{B-} = 3\mathbf{e}_x - \frac{1}{10}\mathbf{e}_y$, the angles to the flow direction θ_{B-} and θ_C vary as the flow directions change, but the relative angle between them, $\theta_C - \theta_{B-}$, remains a constant defined by the array. The angle between modes B_- and C is insensitive to small changes in flow direction for $\mathbf{v}$ near (in this case) $3\mathbf{e}_x - \frac{1}{10}\mathbf{e}_y$.

This insensitivity to flow direction is an example of a plateau in a so-called 'devil's staircase': transport through a 2-D periodic potential is independent of the flow direction near small integer lattice vectors [9]. In this case the lattice vectors are $\mathbf{a}_1 = \mathbf{t}_C = \mathbf{e}_x + (3/10)\,\mathbf{e}_y$ and $\mathbf{a}_2 = \mathbf{e}_y$, and the two close-lying flow directions are $\mathbf{t}_{B-} = 3\mathbf{e}_x - \frac{1}{10}\mathbf{e}_y = 3\,\mathbf{a}_1 - \mathbf{a}_2$ and $\mathbf{a}_1 = \mathbf{t}_C$.

The interplay between lattice directions and applied forces has been documented extensively in the literature of kinetically and statistically locked-in transport. Of interest in the present context is that many numerical simulations of trajectories through various two-dimensional periodic potentials have been done to study these and other phenomena, including sorting of particles [9–12].

The interaction between posts and particles that we have chosen simplifies DLD to a 1D distribution that evolves in time. This allows the effects of diffusion to be easily incorporated into our modeling of the dynamics of the distribution of particles. Also, the particular interaction between point-sized posts and finite-sized particles depends only on particle size, an analysis that seems to be absent from the literature.

B. Diffusion, detectability and experimental possibilities

A clear difference between the results in Fig. 4, based on zero-sized posts, and those reported in the literature, based on finite-sized posts, is that the critical radius (defined as the inflection point of the angle *vs.* radius graph near $r = r_c$), decreases for lower flow velocities in Ref. [1], whereas our simulations show a critical radius that is essentially constant. When particles have more time to diffuse laterally in reported experimental data, ones that previously followed the 'zigzag' path follow something closer to Mode C but not the other way around. We have identified the difference in size of the posts as the primary basis for the difference in symmetry. In the gap between the posts, only beads smaller than r_c can change modes (from A to C) whereas beads larger than r_c cannot change modes because of steric hindrance. Diffusion between posts is thus asymmetric. On the other hand, between rows all beads can change modes equally well so that the effect of diffusion is symmetric. This result is most clearly seen in two cases: (*i*) with sufficiently large posts and small spacing between rows, diffusion between posts dominates leading to asymmetry, and (*ii*) with our needle-like posts, instead diffusion between the rows dominates, leading to symmetry between small and large particles. In devices with large round posts such as those in Ref. [1], the flow streams are narrower in the gap between the posts than in the region between the rows making the asymmetric diffusion even more pronounced. The symmetry about r_{c2} shows that sorting in this model is robust against changes in flow velocity.

As discussed in Sec. IV A, there is no difference between modes A and B_- when the flow is directed along the lattice direction $3\mathbf{a}_1 - \mathbf{a}_2$, which is equivalent to a conventional array with $M = 1$ and $N = 3$, instead of along $\mathbf{e}_x$. Also, while mode B_- for the 3/10 array shown in Fig. 2 is directed away from mode C, the mode B_+ discussed in Sec. II A is deflected away from $\mathbf{v}$ towards mode C. The absence of modes B_- and B_+ in previous analyses of DLD experiments stems from the use of tilted square arrays with flows chosen such that $M = 1$ or more general arrays that are still limited to simple row-shifts $1/N$. In these cases, Modes A and B are the same: they both go along the direction of flow. Interestingly, in their paper Ref. [2], Inglis *et al.* mention that they are studying simple row-shift fractions $\epsilon = 1/N$, with N being an integer, but they do not comment on the data points in their Fig. 2 that clearly have $\epsilon \neq 1/N$.

Experimental detection of mode B requires that the distributions of modes A and B must be spatially separated. The numerically calculated distributions shown in Fig. 5 exhibit four qualitative regimes that could be observed in an experiment to detect the presence of particle transport in mode B.

(a). At very high flow speeds, corresponding to $D = 0$ in the numerical data, the three modes are completely separated because each distribution is very narrow. In this regime, arbitrary spatial separation can be achieved simply by running the particles through a longer array.

(b). At high intermediate flow speeds, the distributions have widened due to diffusion, but modes A and B are clearly distinguishable, despite some overlap.

(c). At low intermediate flow speeds, modes A and B overlap enough to prevent resolution of two separate distributions. This regime is relevant to DLD device design because it would be experimentally observed as an anomalous, asymmetric broadening of the distribution associated with the 'zigzag' path.

(d). At low flow speeds, distributions from modes A and B are completely overlapping and it may even be difficult to differentiate them from mode C.

Experimental realization of the regime investigated in this model would require arrays made with very small posts to minimize hydrodynamic effects on particle trajectories. This also corresponds to a reduction in hydrodynamic drag, which is beneficial for researchers seeking to increase fluid throughput of devices.

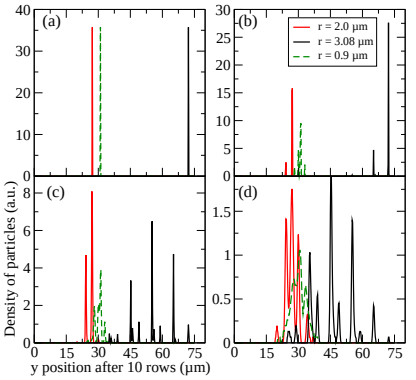

FIG. 5: (Color online) Distributions of three particle sizes: $r = 0.90$ (dashed line), 2.00 (red/gray), and 3.08 μm (black) after transport through ten rows of the $N = 10$, $M = 3$ array. The total number of particles is the same in each case and each initial distribution (not shown) is a square distribution with a narrow width centered on $y = 30$ μm. (a) No diffusion. (b) With diffusion and $v = 1000$ μm/s. (c) With diffusion and $v = 100$ μm/s. (d) With diffusion and $v = 10$ μm/s. Panel (b) shows a case where mode B_- could be detected experimentally. For the lower speed in panel (c), modes A and B_- cannot be resolved, but the combined distribution is broader than mode A alone. For the even lower speed in panel (d) the distributions of particles in modes A and B_- are each wider than the separation between them and the two modes are completely unresolvable.

As can be seen in Fig. 3, the angle θ_B is small compared to θ_C. In order to differentiate between particles traveling in modes A and B, size dispersion of beads must be considered in addition to broadening due to diffusion. Commercially available polystyrene beads used in DLD experiments typically have size distributions with widths of less than ±10 %. This then requires choosing particles whose size distributions are separated by more than 10 %, such as those shown in Fig. 5, or the use of a DLD array to create a sufficiently narrow size distribution. If hydrodynamic effects or limitations on flow velocity in a particular experiment prevent the novel sorting mode from being completely resolved, it may still appear as an asymmetric broadening of the distribution of seemingly undeflected particles, as in Fig. 5.

In general, the separation angles for a given M/N-array can be made larger to the extent that the aspect ratio α can be made smaller without risking clogging of the largest particles. By consulting Table I, it can be seen that the novel separation angle of the 3/10-array is one of the smaller B angles, and also, the 3/8-, 3/11-, 4/11- and 5/12-arrays offer both the B_+ and the B_- modes.

V. CONCLUSIONS

We have identified novel sorting modes in a model of transport through a DLD device characterized by row-shift fractions M/N. Our simple model also reproduces key features of DLD arrays, including sorting based on size and the blurring of cutoffs between modes due to diffusion. Even if not completely resolved, the novel sorting mode has the potential to increase spatial broadening of 'zigzag' particle distributions. In order to avoid this broadening, adjustable DLD arrays could use variable spacing while maintaining a fixed $M = 1$ geometry, such as in Ref. [4], or tune flow angles to exactly reproduce the $M = 1$ condition across a fixed obstacle array using techniques such as in Ref. [13]. Our simulations indicate that using needle-like posts decreases the shift in critical size due to diffusion that has been observed in devices where the post separation is on the same scale as the post diameter. Furthermore, the use of more general array geometries and simplified fluid dynamics links this work to the field of kinetically locked transport phenomena.

VI. ACKNOWLEDGEMENTS

This research is supported by the National Science Foundation under CAREER Grant No. 0239764 and IGERT International Travel Award, the Danish Research Council for Technology and Production Sciences Grant No. 26-04-0074, and the Swedish Research Council, under Grants No. 2002-5972 and 2007-584.

[1] L. R. Huang, E. C. Cox, R. H. Austin, and J. C. Sturm, Science **304**, 987 (2004).

[2] D. W. Inglis, J. A. Davis, R. H. Austin, and J. C. Sturm, Lab on a Chip **6**, 655 (2006).

[3] J. A. Davis, D. W. Inglis, K. J. Morton, D. A. Lawrence, L. R. Huang, S. Y. Chou, J. C. Sturm, and R. H. Austin, Proceedings of the National Academy of Sciences of the USA **103**, 14779 (2006).

[4] J. P. Beech and J. O. Tegenfeldt, Lab on a Chip **8**, 657 (2008).

[5] M. Heller and H. Bruus, J. Micromech. Microeng. **18**, 075030 (2008).

[6] T. Mårtensson, M. Borgström, W. Seifert, B. J. Ohlsson, and L. Samuelson, Nanotechnology **14**, 1255 (2003).

[7] Strict definitions: $\lfloor x \rfloor = \max\{n \in \mathbb{Z} | n \leq x\}$ and $\lceil x \rceil = \min\{n \in \mathbb{Z} | n \geq x\}$.

[8] H. Bruus, *Theoretical Microfluidics*, Oxford University Press (Oxford, 2008).

[9] C. Reichhardt and F. Nori, Physical Review Letters **82**, 414 (1999).

[10] A. Lacasta, M. Khoury, J. Sancho, and K. Lindenberg, Modern Physics Letters B **20**, 1427 (2006).

[11] K. Ladavac, K. Kasza, and D. G. Grier, Physical Review E **70**, 010901 (2004).

[12] Y. Roichman, V. Wong, and D. G. Grier, Physical Review E **75**, 011407 (2007).

[13] L. R. Huang, J. O. Tegenfeldt, J. C. Sturm, R. H. Austin, and E. C. Cox, Technical Digest International Electron Devices Meeting (Washington DC), 363-366 (2001).

B.3. Paper submitted to Stroke

Title Geometry Regulates Hemodynamics in Saccular Aneurysms.

Authors Marjan Rafat, Martin Heller, Howard A. Stone, and Debra T. Auguste.

Reference Submitted to Stroke – Journal of The American Heart Association, August 2008.

Stroke

JOURNAL OF THE AMERICAN HEART ASSOCIATION

Geometry Regulates Hemodynamics in Saccular Aneurysms
Marjan Rafat, Martin Heller, Howard A. Stone, and Debra T. Auguste
STROKE/2008/533943 VERSION 1

Author Disclosures

Marjan Rafat: No disclosures

Martin Heller: No disclosures

Howard A. Stone: No disclosures

Debra T. Auguste: No disclosures

Downloaded from http://submit-stroke.ahajournals.org on August 11, 2008

Geometry Regulates Hemodynamics in Saccular Aneurysms

Marjan Rafat, SM;* Martin Heller, MSc[†]; Howard A. Stone, PhD;* Debra T. Auguste, PhD*[§]

* School of Engineering and Applied Sciences, Harvard University, Cambridge, MA 02138

[†] Department of Micro- and Nanotechnology, Technical University of Denmark, DTU Nanotech, DK-2800 Kongens Lyngby, Denmark

[§] Corresponding Author. 29 Oxford Street, Cambridge, MA 02138. Fax: 617 495 9837. Phone: 617 384 7980. Email: auguste@seas.harvard.edu

Acknowledgments

Martin Heller was supported by the Danish Research Council for Technology and Production Sciences grant no. 26-04-0074. The authors would like to thank Derek Vigil for his preliminary analysis of aneurysm fluid flow and shear stress.

Disclosures

None.

Geometry Regulates Hemodynamics in Saccular Aneurysms

Word Count: 4,730

Cover title: Geometry Regulates Saccular Aneurysm Hemodynamics

Keywords: Hemodynamics; Intracranial Aneurysm; Saccular Aneurysm

Abstract

***Background and Purpose*—**The mechanisms behind aneurysm pathophysiology remain unknown, which makes treatment options ambiguous. Understanding aneurysm hemodynamics may aid in the prediction of aneurysm growth and rupture and allow development of new treatment strategies.

***Methods*—**We analyzed flow patterns in aneurysm geometries for two-dimensional, steady-state flow over a range of Reynolds numbers (0 to 500). The geometric characteristics of the aneurysms are defined as the aneurysm height to width (H_A/W_A) and neck width to parent vessel width (W_N/W_P) ratios, which have been identified as significant in recent clinical studies. Aneurysms were centered at the midpoint of a bifurcation, offset from the bifurcation midpoint, and on a lateral vessel. Wall shear stress profiles were also evaluated.

***Results*—**Our model depicts symmetric and asymmetric flow patterns, with the appearance of eddies and penetrating jets that are characteristic of inefficient and efficient mass transport, respectively. The distinguishing features of the flows are mapped as a function of Reynolds number and geometry. For aneurysms centered at the midpoint of a bifurcation, we observe the flow development as a function of increasing W_N/W_P and H_A/W_A from eddies to penetrating bifurcating jets with eddies to asymmetric flows. We also found that areas of low shear stress increase with increasing H_A/W_A. Increasing H_A/W_A causes dominating areas of eddies in offset and lateral aneurysms.

***Conclusions*—**We have developed systematic “flow maps” for clinically relevant aneurysm geometries and Reynolds numbers. Our nondimensional analysis relates aneurysm geometry to the incidence of growth and rupture.

Introduction

Weak areas in the walls of the vasculature can expand to form blood-filled sacs, or aneurysms.[1, 2] Aneurysms pose a major health risk; approximately 30,000 cerebral aneurysms rupture annually in the US, commonly causing subarachnoid hemorrhage.[2, 3] Prediction of aneurysm growth and rupture may be achieved by understanding the fluid and solid mechanics of blood flow and vessel structure. In this paper, we use numerical methods to study the flow patterns in clinically relevant aneurysm geometries to relate hemodynamics to incidence of rupture.

Numerical simulations of fluid flow, computational fluid dynamic models based on clinical data, and geometric analyses are among the many approaches taken to study the pathophysiology of this disease. Previous hemodynamic studies have attempted to elucidate distinguishing flow features of aneurysms using numerical simulations. In one analysis, Perktold et al. used the finite-element method to determine the velocity fields in wide and narrow necked aneurysms under pulsatile flow at two Reynolds numbers.[4] They speculated that eddy formation in the center of the aneurysm head contributes to thrombus formation or cell aggregation, which may lead to growth and rupture of an aneurysm. The finite-element method was also used in a two-dimensional (2D) model of lateral aneurysms under steady flow.[5] It was found that the magnitude of shear stress on the aneurysm wall depends on the geometry, which suggests that the shape of the aneurysm could influence aneurysm growth. These and other studies agree that aneurysm hemodynamics is a function of the geometry; the outcome of these hemodynamic changes is unclear.

Analysis of aneurysm hemodynamics has been assessed in a clinical context. Cebral et al. evaluated the risk of rupture as a function of hemodynamics in patient-specific aneurysm

geometries.[6] In particular, they developed a computational fluid dynamic (CFD) model based on the three-dimensional (3D) angiographs of real patients. They also determined that complex flows and narrow inflow jets were characteristic of ruptured aneurysms.

Several hypotheses have been made that link geometric factors to aneurysm rupture.[5-8] For example, Utter and Rossmann found a correlation between an elliptical shape factor and wall shear stress that could indicate an increased susceptibility to rupture.[7] Hoh et al. suggest that 2D shape factors are statistically significant in determining aneurysm rupture.[8] Their study evaluated aneurysm geometry in patients with both unruptured and ruptured aneurysms and concluded that specific geometrical shape factors contribute to rupture. We extend this work by describing the physical phenomena (i.e. stress, pressure, flow conditions, approximate flow fields) that arise due to the different geometries of the aneurysms.

It is clear from this brief survey that many unanswered questions remain for elucidating the link between hemodynamic features, aneurysm geometry, and rupture. Though it is generally accepted that hemodynamics is important in understanding the fate of aneurysms, most studies focus on a limited number of geometries and flow rates, which does not allow extension of the conclusions to a wide range of aneurysms. We probe the relationship of aneurysm geometry to flow patterns using nondimensional terms, which allows for broad application of our data to patient specific aneurysms.[8] Specifically, we determine what changes in flow patterns occur as geometry is altered and how sensitive flow characteristics are to changes in geometry. Additionally, because wall shear stress has previously been implicated in aneurysm growth and rupture, we evaluate how the shear stress at the aneurysm walls relates to differences in geometry.[9]

In this study, a "flow mapping" scheme is presented to evaluate common features of saccular aneurysms over a wide range of geometries and flow conditions. We categorize aneurysm geometries previously shown to be statistically relevant by their height to width (height of the aneurysm/width of the aneurysm or H_A/W_A) and neck to parent (width of the aneurysm neck/width of the parent vessel or W_N/W_P) ratios (Figure 1A). We evaluate the flow patterns for aneurysm geometries centered on a bifurcating vessel, offset from a bifurcating vessel, and in a lateral vessel. We assume an incompressible 2D, steady-state flow of a Newtonian fluid over a range of physiologically relevant Reynolds numbers (Re), which represents the ratio of inertial to viscous forces; previous work has shown that the flow profiles do not change qualitatively when contrasting pulsatile with steady conditions.[10] In addition, wall shear stress profiles are examined upon changing geometries. Though many 3D, pulsatile flow models have been published for distinct geometries, mapping flow patterns as a function of geometry and Re as we do here may be useful for characterizing common hemodynamic features that correlate with aneurysm formation, growth, and rupture. Of particular interest are flows that result in low shear stress at the vessel wall and conditions that give rise to mass transfer limitations due to eddies in the neighborhood of the aneurysm. This analysis could lead to insights into new treatment and drug delivery strategies based on manipulation of hemodynamics.

Methods

Aneurysm Geometry

Schematics of the geometries of the aneurysms used in our computational modeling are shown in Figures 1A, C, and D. Widths for the parent (entrance channel) and daughter vessels

(branching or bifurcating channels) were chosen as 4 mm and 3 mm, respectively, which approximate physiological parameters.[10] We have also set the lengths of the parent and daughter vessels at 30 and 13 mm, respectively. We have defined two ratios: the height to width (H_A/W_A) ratio and the width of the neck to width of the parent vessel (W_N/W_P) ratio. W_N/W_P physically describes impingement upon the aneurysm; when the neck and parent vessel widths are equivalent in size, then $W_N/W_P=1$. In our simulations, H_A/W_A varies between 0.5 and 1.75 and W_N/W_P varies between 0.2 and 1.5. The shape factor H_A/W_A has been previously implicated in aneurysm rupture.[8] Figures 1C and 1D show representative images for offset and lateral aneurysms, respectively. In addition to the geometry, the flow is characterized by the dimensionless Reynolds number (Re) (Equation 1).

$$\mathrm{Re} = \frac{\rho W_p \bar{u}}{\eta} \qquad (1),$$

where ρ is the density, W_P is the width of the parent vessel, $\bar{u}$ is the mean velocity, and η is the fluid viscosity. Literature values of Reynolds numbers in cerebral arteries vary, and we focused on a physiological range of $100<\mathrm{Re}<400$.[11] Variability in the patient condition may include differences in hematocrit, which impacts viscosity, and blood pressure, which impacts velocity.

Computational Model

We numerically solved the Navier-Stokes (Equation 2) and continuity (Equation 3) equations assuming incompressible flow of a Newtonian fluid using the COMSOL 3.3 Multiphysics finite-element software:

$$\rho\left(\frac{\partial \boldsymbol{u}}{\partial t} + (\boldsymbol{u}\cdot\nabla)\boldsymbol{u}\right) = -\nabla p + \eta\nabla^2\boldsymbol{u} \qquad (2)$$

$$\nabla \cdot \boldsymbol{u} = 0 \qquad (3),$$

where p is the pressure, u is the velocity vector, and η is the fluid viscosity. We assumed two-dimensional, steady ($\frac{\partial \boldsymbol{u}}{\partial t}$ =0) flow in a rigid-wall model of a vessel.[4, 7, 10] It should be noted that Steiger et al. found that flow patterns do not change qualitatively when comparing steady to pulsatile flow at Re=300.[10] Blood density and viscosity were assumed to be 1060 kg/m^3 and 3 cP, respectively.[12, 13] We performed a large number of numerical simulations and illustrated the results by plotting the streamlines for these steady flows. Additionally, wall shear stress profiles were calculated along the aneurysm boundary arc length. The geometries were resolved with a fine mesh (Figure 1B), with special attention paid to the region of the aneurysm and the corners, and we confirmed that the streamlines and wall shear stress profiles converge with a coarser mesh.

Results

Centered Aneurysms

We show six different characteristic flow patterns (Figure 2) that are found commonly upon altering the aneurysm H_A/W_A, W_N/W_P (Figure 1A), and Re. These patterns are distinguished qualitatively by having symmetrical (Figure 2A) and asymmetrical (Figure 2B) streamline patterns. The symmetric patterns show the formation of eddies (Figure 2Ai), penetrating bifurcating jets (Figure 2Aii), and penetrating bifurcating jets with eddies (Figure 2Aiii). The observed asymmetric streamline patterns consisted of penetrating jets with eddies (Figure 2Bi), penetrating bifurcating jets (Figure 2Bii), and penetrating bifurcating jets and eddies (Figure 2Biii).

By visually inspecting various streamline patterns, we created flow maps by plotting W_N/W_P versus Re for multiple H_A/W_A values and qualitatively demarcated the transitions between streamline patterns (Figure 3). Mapping of the distinct flow patterns defines common characteristics that appear as a function of Re and geometry. Representative images of the aneurysm geometry are placed at the bottom of each graph for visualization of W_N/W_P. The physiologically relevant Re range is located between the dashed lines.

We have determined that there are distinct flow patterns as W_N/W_P and Re are varied. For H_A/W_A=0.5 (Figure 3A), we observe a combination of penetrating bifurcating jets and eddies when $0.2<W_N/W_P<0.5$ and below Re=150. Beyond this regime, only penetrating bifurcating jets are seen. Figure 3B (H_A/W_A=1) depicts eddies at low Re (<100) and low W_N/W_P (<0.5). Penetrating bifurcating jets with eddies are found at intermediate values of Re (100<Re<300) for all W_N/W_P ratios. Asymmetric flows dominate at large Re. The transitions between the flow regimes show a decreasing dependence on the W_N/W_P ratio. Mappings of H_A/W_A=1.25 or 1.5 (data not shown) have similar profiles to the results for H_A/W_A=1.

When H_A/W_A=1.75 (Figure 3C), the appearance of eddies at low W_N/W_P is approximately independent of Re. Also, bifurcating jets with eddies exist beyond $W_N/W_P>0.5$ but only below physiologically relevant Reynolds numbers (100<Re<400). Asymmetric flows are observed for physiological Re for $0.4<W_N/W_P<1.5$. The transition between eddies and asymmetric flow has a steep, decreasing dependence on W_N/W_P. The transition between bifurcating flow with eddies and asymmetric flow occurs between 50<Re<100.

Wall Shear Stress Analysis

There are multiple hypotheses about the role of shear stress in aneurysm growth and rupture.[9, 14] Hence, we evaluated physiologically relevant wall shear stresses along the aneurysm boundary for varying geometries and Re. Wall shear stress profiles and the corresponding streamlines are shown in Figure 4A-C for Re=400, W_N/W_P =1, and three different H_A/W_A ratios. The results utilize the arc length which is non-dimensionalized by the parent vessel diameter. The results show that as H_A/W_A increases, the fraction of the aneurysm's arc length that experiences very low shear stress (<0.01 N/m^2) increases. It is convenient to present these results by reporting the arc length ratio, by which we denote the fraction of the arc length that experienced this low shear stress. Although the magnitude of the shear stress typically increases with Re (results not shown), we also found that as the Re increases, the arc length ratio with low shear stress decreases at the same H_A/W_A (Figure 4D).

Offset Aneurysms

We also studied flow patterns that arise in aneurysms offset from the inflow (Figure 1C). By visual inspection, the characteristic flows in this geometry are all asymmetric and consist of eddies, penetrating jets, or penetrating jets with eddies (Figure 5A).

We have mapped flow patterns for offset aneurysms with respect to various H_A/W_A and W_N/W_P (Figure 5). For H_A/W_A=0.5 (Figure 5B), two types of flows are observed: penetrating jets with eddies at low W_N/W_P and penetrating jets when W_N/W_P is > 0.5. When H_A/W_A=1 (Figure 5C), the flow is mostly penetrating jets with eddies except for a region of penetrating jets below physiological Re ($0<Re<60$) and $W_N/W_P>1$. The mapping of H_A/W_A=1.25 and 1.5 (data not shown) are similar to the graphs for H_A/W_A=1.75 (Figure 5D). The map displays mostly

penetrating jets with eddies, except for a region of eddies at low Re ($0<Re<50$) and W_N/W_P ($0.2<W_N/W_P<1$).

Lateral Aneurysms

We mapped flow patterns in lateral aneurysms (Figure 1D). Over the entire range of H_A/W_A, asymmetric flows dominate. The characteristic asymmetric flows consisted of penetrating jets with eddies (Figure 6Ai), eddies (Figure 6Aii), or layered eddies (Figure 6Aiii). For H_A/W_A=0.5 (Figure 6B), asymmetric flows dominate the map except for a small area of penetrating jets with eddies at low Re (<10) and low W_N/W_P ($0.2<W_N/W_P<0.5$). Similarly, H_A/W_A=1 (Figure 6C) predominantly has asymmetric flows with an area of eddies ($W_N/W_P<0.2$ and $0<Re<150$) and an area of penetrating jets with eddies ($Re<150$ and $0.22<W_N/W_P<0.5$). Similar flow patterns have been found in the literature. For example, the computational study of Burleson et al. shows an asymmetric eddy profile for an aneurysm with H_A/W_A=0.925, Re=300, and W_N/W_P=2.[5]

Increasing the H_A/W_A ratio to 1.25 (Figure 6D) reveals layered eddies at $W_N/W_P>1$ and $Re>100$ but also has small regions of eddies and penetrating jets with eddies at low Re ($Re<50$) and low W_N/W_P ($W_N/W_P<0.6$). The maps with H_A/W_A=1.25 (Figure 6D) and 1.5 (data not shown) are similar, with the area of layered eddies becoming more prevalent ($W_N/W_P>0.5$ and $Re>10$).

As H_A/W_A is increased to 1.75 (Figure 6E), the area on the map of single eddies increases and is independent of Re for $W_N/W_P<0.5$. An area of penetrating jets with eddies exists for low Re ($Re<150$) and intermediate W_N/W_P values ($0.5<W_N/W_P<1$). Asymmetric flows are dominated by layered eddies over a large range of Re ($0<Re<500$) at $W_N/W_P>0.4$. The transition between

eddies and asymmetric flow is steeply decreasing, whereas the transition between penetrating jets with eddies and asymmetric flow is gradually decreasing. We find a small dependence on W_N/W_P at $H_A/W_A<1$ for this geometry. Above $H_A/W_A=1$, we observe a steep transition between asymmetric flows, eddies, and layered eddies.

Discussion

The process of aneurysm growth and rupture is most likely a combination of physical and biological phenomena. Our systematic mapping of the basic flow patterns correlates aneurysm geometry and clinically relevant Reynolds numbers (Re) with distinctive flow patterns. Flow and transport processes are well known to regulate the mechanisms of health and disease, so these basic flow characterizations facilitate our understanding of how the hemodynamic landscape may affect mass transport and complex biological processes.[15] In addition, we have shown how geometry and shear stress are coupled.

Our mapping scheme demonstrates that flow characteristics in centered aneurysms are more sensitive to changes in geometry than in offset or lateral aneurysms. We observe that for a given Re, the flow profiles in centered aneurysms evolve from regions of eddies to penetrating bifurcating jets with eddies to asymmetric flows as the neck to parent vessel width (W_N/W_P) ratio increases, which corresponds to an increase in the area of impingement.

Mass transfer limitations most likely occur in the presence of eddies, which we have shown occur readily at low W_N/W_P ratios. Such transitions between regions of different flow patterns may be important in diagnoses, assessment of treatment of options, and predictions of rupture. As aneurysms change geometry or Re, the flow patterns are altered, which may define a potential treatment strategy where flow patterns could be manipulated to reduce the incidence of

aneurysm rupture or as a strategy for remodeling. Moreover, mappings of the flows in offset and lateral aneurysms have a weaker dependence on the aneurysm geometry. Offset aneurysms, which are off-center from the midpoint of a bifurcating vessel, are dominated by penetrating jets or penetrating jets with eddies. Lateral aneurysms, where the flow is parallel instead of perpendicular to the aneurysm, are dominated by asymmetric flows or layered eddies.

In addition, previous studies suggest a correlation between an increase in H_A/W_A and the incidence of aneurysm rupture.[8] As H_A/W_A increases in centered aneurysms (Figure 3), penetrating bifurcating jets become less evident and asymmetric flows and eddies are more prevalent. Asymmetric aneurysms (Figure 5) show a decrease in penetrating jets and an increase in eddies as H_A/W_A increases. In lateral aneurysms (Figure 6), we observe a similar trend with an increase in eddies, specifically layered eddies. Based on these mappings, we speculate that eddies (layered for lateral vessels), which may limit mass transfer, could contribute to aneurysm growth and rupture. Penetrating and bifurcating jets, seen only at low H_A/W_A (0.5 for centered and <1 for offset aneurysms), should allow a rapid influx of nutrients while eddies cause stagnation within the aneurysm head. Stagnation has been linked to thrombus formation, which may relate to the secretion of matrix metalloproteinases that damage the vessel wall during repair mechanisms.[10, 16, 17] This hypothesis coincides with the patient specific study of Cebral et al.[6] In their work, they found that large impingement regions correlated with unruptured aneurysms, and aneurysm rupture was more prevalent with smaller impingement regions.

Flow characteristics are also important in aneurysm growth and remodeling. Meng et al. surgically created a bifurcation in the carotid vasculature of canines to assess aneurysm formation.[9, 18] They reported aneurysm growth and remodeling events, such as hyperplasia and the disruption of the internal elastic lamina and medial layer at the apex of the bifurcation, as a

result of wall shear stress and shear stress gradients. The study of Chatziprodromou et al. used CFD and physiological data to understand aneurysm growth.[19] They examined the shear stress-mediated loss of vascular tone through smooth muscle cell apoptosis, rupture, degradation, and reconstruction of the medial collagen and elastin fibers. These studies demonstrate that altering fluid flow within blood vessels creates appreciable biological changes. Our study documents the important changes in flow experienced upon geometric alterations.

In addition, we found that shear stress profiles are affected by changes in geometry: as H_A/W_A increases at a given W_N/W_P and Re, the area along the aneurysm wall with low shear stress increases. In a computational study that modeled patient aneurysms, Shojima et al. found that the areas of highest shear stress were near the neck of the aneurysm while the shear stress significantly decreased in the aneurysm head area, which resembles our findings.[14] We speculate that the appearance of eddies contributes to a) the increase in low shear along the aneurysm boundary and b) the stagnation that has been linked to aneurysm rupture.[4, 10] This result correlates with the Hoh et al. study, which found that increases in H_A/W_A are associated with increased rupture.[8] We see more incidences of eddies and areas of low shear as H_A/W_A increases, which could contribute to aneurysm wall remodeling and rupture. Taken together, mass transfer and shear stress appear to play a critical role in predicting aneurysm growth and rupture.

Combining our hemodynamic studies with biological response data may facilitate our understanding of aneurysm formation and rupture. For example, Malek et al. have studied the biological response of endothelial cells (ECs) due to fluid flow and shear.[20-24] Monolayers of ECs were subjected to steady laminar, turbulent, and pulsatile shear stresses with a cone-plate viscometer. Thrombomodulin was downregulated by shear while fibrinolytic tissue plasminogen activator was increased, demonstrating the dynamic response of ECs under flow conditions.

Shear also regulated EC expression of endothelin-1, basic fibroblast growth factor, and platelet-derived growth factor B mRNA.[20, 21] These studies showed no significant change in trends of gene expression when comparing steady or pulsatile flow character; rather, gene expression was dependent on shear stress magnitude and exposure time. Understanding how hemodynamic characteristics influence cellular biology may allow the discovery of new treatment strategies that exploit protein regulation for aneurysm management.

Current treatments for aneurysms are either invasive or ineffective for certain aneurysm geometries. Wide-necked aneurysms cannot be treated using the endovascular embolization technique.[25] New treatment strategies may circumvent microvascular clipping based on alteration of flow characteristics that lead to rupture or by controlling the shear-induced cellular response. Further analysis of how flow-induced shear stress impacts the biological response may elucidate how clinically relevant geometries and fluid flow patterns relate to our current knowledge of aneurysm pathophysiology.

Summary

We have examined the hemodynamic and shear stress profiles of clinically relevant aneurysm geometries for a range of physiological Reynolds number (Re). Our systematic approach correlates Re with ratios of aneurysm height to width (H_A/W_A) and neck width to parent vessel width (W_N/W_P). Our findings indicate an increase in eddies for bifurcating vessels and layered eddies for lateral vessels for increasing H_A/W_A and W_N/W_P, which may result in mass transfer limitations. For aneurysms on bifurcating vessels, small changes in the geometry or Re may result in distinct changes in the hemodynamic and shear stress profiles, which may (1) correlate with an increased incidence of rupture or (2) be used to manipulate the biological

response to impede rupture or growth. Our nondimensional analysis may be broadly applied to a wide range of aneurysms and patient specific cases.

References

1. Lasheras JC. The biomechanics of arterial aneurysms. *Annu Rev Fluid Mech*. 2007;39:293-319.
2. Peters DG, Kassam AB, Feingold E, Heidrich-O'Hare E, Yonas H, Ferrell RE, Brufsky A. Molecular anatomy of an intracranial aneurysm: Coordinated expression of genes involved in wound healing and tissue remodeling. *Stroke*. 2001;32:1036-1042.
3. Zhang B, Fugleholm K, Day LB, Ye S, Weller RO, Day IN. Molecular pathogenesis of subarachnoid haemorrhage. *Int J Biochem Cell Biol*. 2003;35:1341-1360.
4. Perktold K, Kenner T, Hilbert D, Spork B, Florian H. Numerical blood flow analysis: Arterial bifurcation with a saccular aneurysm. *Basic Res Cardiol*. 1988;83:24-31.
5. Burleson AC, Strother CM, Turitto VT. Computer modeling of intracranial saccular and lateral aneurysms for the study of their hemodynamics. *Neurosurgery*. 1995;37:774-782; discussion 782-774.
6. Cebral JR, Castro MA, Burgess JE, Pergolizzi RS, Sheridan MJ, Putman CM. Characterization of cerebral aneurysms for assessing risk of rupture by using patient-specific computational hemodynamics models. *AJNR Am J Neuroradiol*. 2005;26:2550-2559.
7. Utter B, Rossmann JS. Numerical simulation of saccular aneurysm hemodynamics: Influence of morphology on rupture risk. *J Biomech*. 2007;40:2716-2722.
8. Hoh BL, Sistrom CL, Firment CS, Fautheree GL, Velat GJ, Whiting JH, Reavey-Cantwell JF, Lewis SB. Bottleneck factor and height-width ratio: Association with ruptured aneurysms in patients with multiple cerebral aneurysms. *Neurosurgery*. 2007;61:716-722; discussion 722-713.

9. Meng H, Wang Z, Hoi Y, Gao L, Metaxa E, Swartz DD, Kolega J. Complex hemodynamics at the apex of an arterial bifurcation induces vascular remodeling resembling cerebral aneurysm initiation. *Stroke*. 2007;38:1924-1931.

10. Steiger HJ, Poll A, Liepsch D, Reulen HJ. Basic flow structure in saccular aneurysms: A flow visualization study. *Heart Vessels*. 1987;3:55-65.

11. Gobin YP, Counord JL, Flaud P, Duffaux J. In vitro study of haemodynamics in a giant saccular aneurysm model: Influence of flow dynamics in the parent vessel and effects of coil embolisation. *Neuroradiology*. 1994;36:530-536.

12. DeGroff CG, Thornburg BL, Pentecost JO, Thornburg KL, Gharib M, Sahn DJ, Baptista A. Flow in the early embryonic human heart: A numerical study. *Pediatr Cardiol*. 2003;24:375-380.

13. Taber LA. An optimization principle for vascular radius including the effects of smooth muscle tone. *Biophys J*. 1998;74:109-114.

14. Shojima M, Oshima M, Takagi K, Torii R, Hayakawa M, Katada K, Morita A, Kirino T. Magnitude and role of wall shear stress on cerebral aneurysm: Computational fluid dynamic study of 20 middle cerebral artery aneurysms. *Stroke*. 2004;35:2500-2505.

15. Mohrman DE, Heller LJ. *Cardiovascular Physiology*. McGraw-Hill Companies, Inc.; 2006.

16. Frosen J, Piippo A, Paetau A, Kangasniemi M, Niemela M, Hernesniemi J, Jaaskelainen J. Remodeling of saccular cerebral artery aneurysm wall is associated with rupture: Histological analysis of 24 unruptured and 42 ruptured cases. *Stroke*. 2004;35:2287-2293.

17. Ribourtout E, Raymond J. Gene therapy and endovascular treatment of intracranial aneurysms. *Stroke*. 2004;35:786-793.

18. Meng H, Swartz DD, Wang Z, Hoi Y, Kolega J, Metaxa EM, Szymanski MP, Yamamoto J, Sauvageau E, Levy EI. A model system for mapping vascular responses to complex hemodynamics at arterial bifurcations in vivo. *Neurosurgery*. 2006;59:1094-1100; discussion 1100-1091.

19. Chatziprodromou I, Tricoli A, Poulikakos D, Ventikos Y. Haemodynamics and wall remodelling of a growing cerebral aneurysm: A computational model. *J Biomech*. 2007;40:412-426.

20. Malek A, Izumo S. Physiological fluid shear stress causes downregulation of endothelin-1 mrna in bovine aortic endothelium. *Am J Physiol*. 1992;263:C389-396.

21. Malek AM, Gibbons GH, Dzau VJ, Izumo S. Fluid shear stress differentially modulates expression of genes encoding basic fibroblast growth factor and platelet-derived growth factor b chain in vascular endothelium. *J Clin Invest*. 1993;92:2013-2021.

22. Malek AM, Izumo S. Control of endothelial cell gene expression by flow. *J Biomech*. 1995;28:1515-1528.

23. Malek AM, Izumo S, Alper SL. Modulation by pathophysiological stimuli of the shear stress-induced up-regulation of endothelial nitric oxide synthase expression in endothelial cells. *Neurosurgery*. 1999;45:334-344; discussion 344-335.

24. Malek AM, Jackman R, Rosenberg RD, Izumo S. Endothelial expression of thrombomodulin is reversibly regulated by fluid shear stress. *Circ Res*. 1994;74:852-860.

25. Lanzino G, Kanaan Y, Perrini P, Dayoub H, Fraser K. Emerging concepts in the treatment of intracranial aneurysms: Stents, coated coils, and liquid embolic agents. *Neurosurgery*. 2005;57:449-459; discussion 449-459.

Figure Legends

Figure 1: A) Centered aneurysm model and definition of parameters. The height (H_A) and width (W_A) of the aneurysm are indicated by solid vertical and horizontal lines, respectively. The width of the neck (W_N) and parent vessel (W_P) are respectively shown by a dashed horizontal line and arrows. **B)** Typical mesh used to resolve the aneurysm geometries. **C)** Representative offset aneurysm. **D)** Representative lateral aneurysm.

Figure 2: A) Symmetric flow streamlines. i) Eddies (Re=0.5, H_A/W_A=1, W_N/W_P=0.25) ii) Penetrating bifurcating jets (Re=500, H_A/W_A=0.5, W_N/W_P=0.5) iii) Penetrating bifurcating jets with eddies (Re=200, H_A/W_A=1.5, W_N/W_P=0.4) **B)** Asymmetric flow streamlines. i) Penetrating jets with eddies (Re=500, H_A/W_A=1, W_N/W_P=1.5) ii) Penetrating bifurcating jets (Re=500, H_A/W_A=1.5, W_N/W_P=1) iii) Penetrating bifurcating jets with eddies (Re=150, H_A/W_A=1.75, W_N/W_P=1.5).

Figure 3: Qualitative mapping of flow patterns in terms of various aneurysm height to width (H_A/W_A) ratios, Reynolds numbers (Re), and neck to parent width (W_N/W_P) ratios: **A)** H_A/W_A=0.5 **B)** H_A/W_A=1 C) H_A/W_A=1.75. Dashed lines indicate physiological Re.

Figure 4: Streamlines and shear stress profiles for varying H_A/W_A at Re=400 and W_N/W_P=1. **A)** H_A/W_A = 0.5 **B)** H_A/W_A=1 **C)** H_A/W_A=1.75 **D)** Aneurysm arc length ratio with low shear stress along aneurysm wall for varying H_A/W_A and Re at W_N/W_P=1.

Figure 5: A) Examples of flow patterns in offset aneurysms. i) Eddies (Re=10, H_A/W_A=1.5, W_N/W_P=0.2) ii) Penetrating jets with eddies (Re=10, H_A/W_A=1.5, W_N/W_P=1) iii) Penetrating jets (Re=200, H_A/W_A=0.5, W_N/W_P=0.5).

Flow mapping in terms of various aneurysm height to width (H_A/W_A) ratios, Reynolds numbers (Re), and neck to parent width (W_N/W_P) ratios: **B)** H_A/W_A=0.5 **C)** H_A/W_A=1 **D)** H_A/W_A=1.75. Dashed lines indicate physiological Re.

Figure 6: A) Characteristic asymmetric flows in lateral aneurysms: i) Penetrating jets with eddies (Re=5, H_A/W_A=1, W_N/W_P=1.5) ii) Eddies (Re=300, H_A/W_A=1, W_N/W_P=1.5) iii) Layered eddies (Re=500, H_A/W_A=1.5, W_N/W_P=0.5).

Flow mapping in terms of various aneurysm height to width (H_A/W_A) ratios, Reynolds numbers (Re), and neck to parent width (W_N/W_P) ratios: **B)** H_A/W_A=0.5 **C)** H_A/W_A=1 **D)** H_A/W_A=1.25 **E)** H_A/W_A=1.75. Dashed lines indicate physiological Re.

Figure 1.

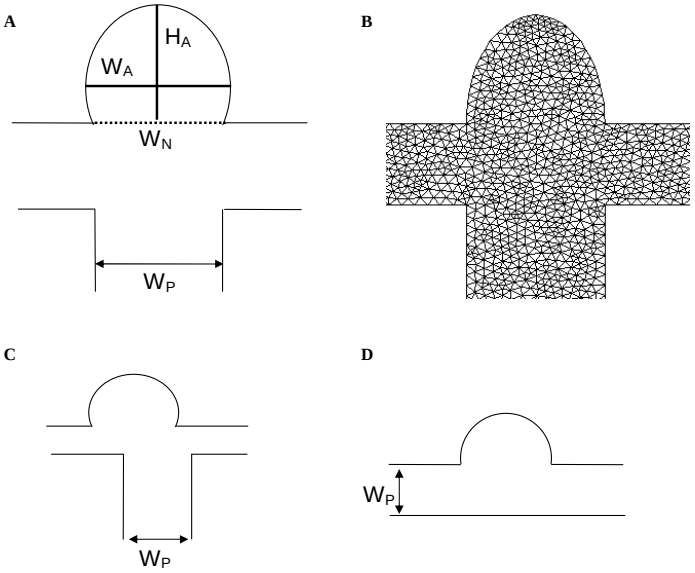

Figure 2.

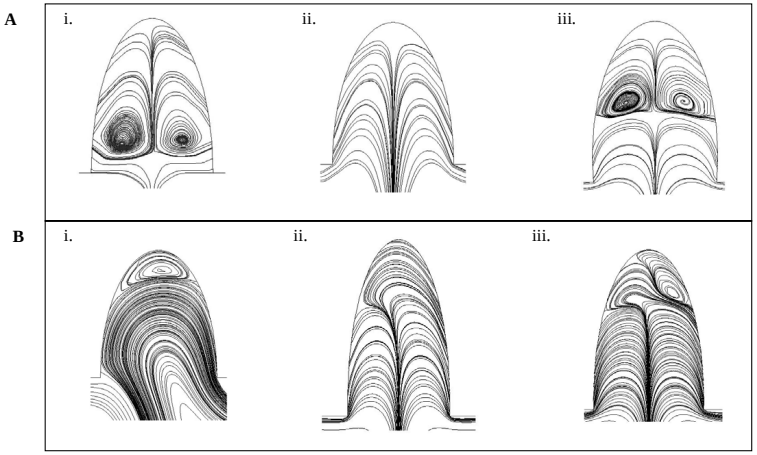

Figure 3.

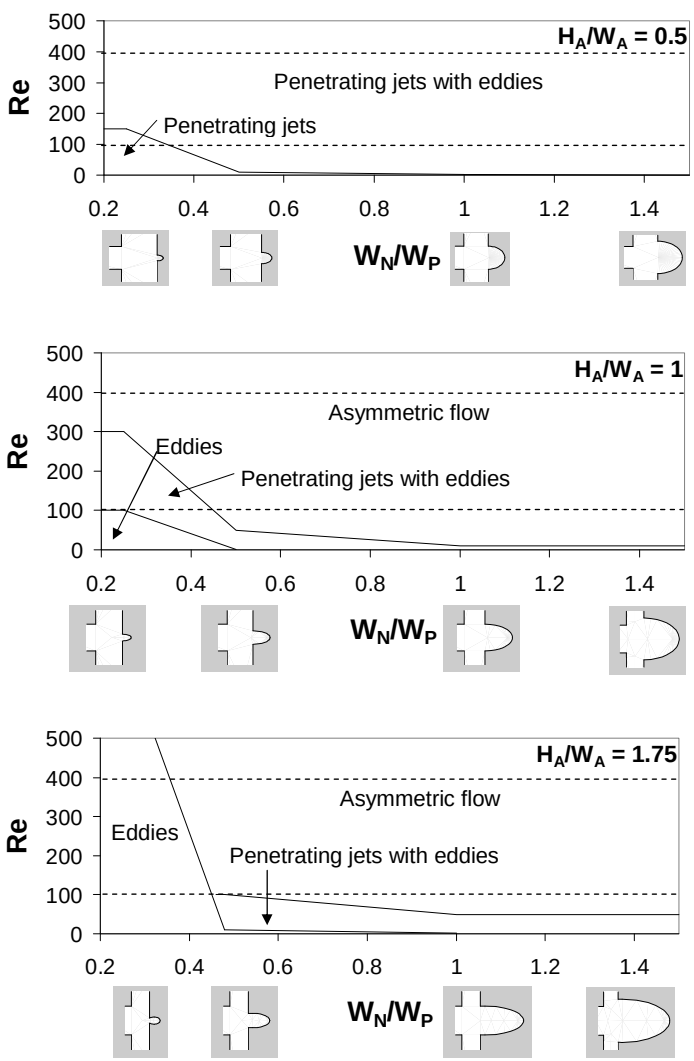

Figure 4.

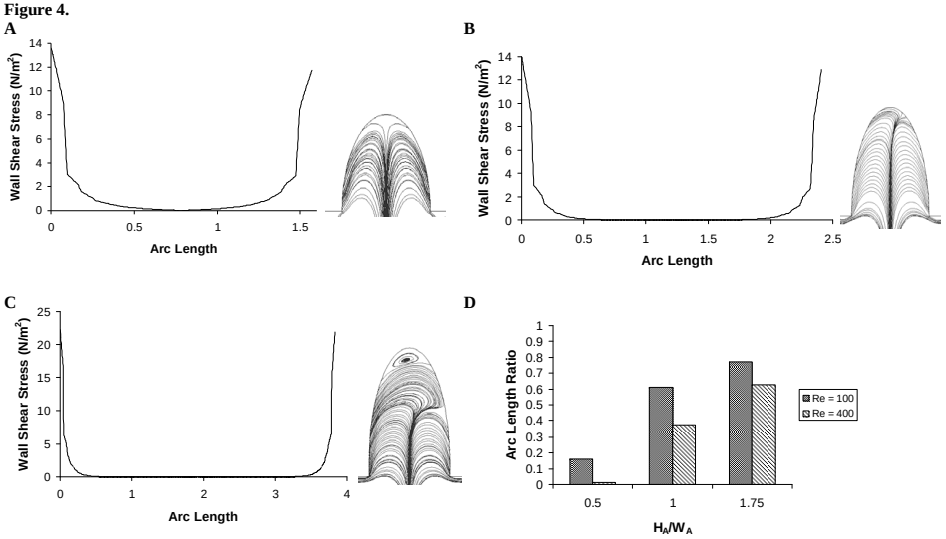

Figure 5.

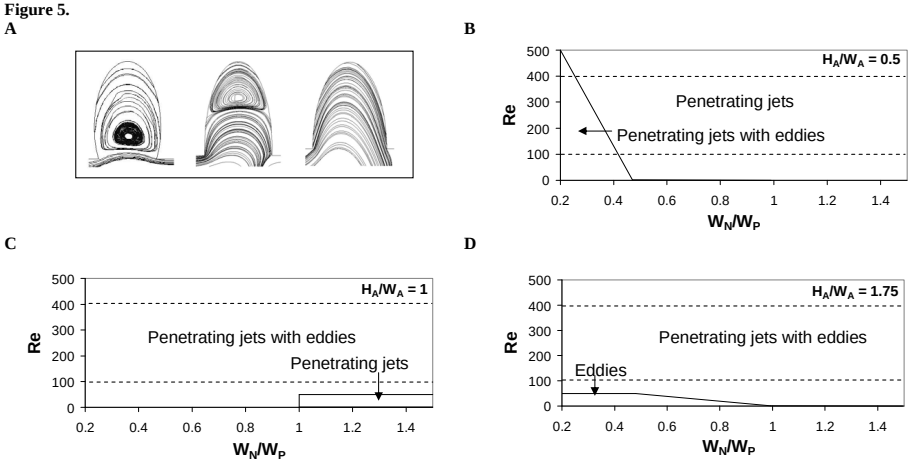

Figure 6.